Università degli Studi di Padova

Dipartimento di Fisica e Astronomia "Galileo Galilei"

Master degree in Astrophysics and Cosmology

Final Dissertation

Modeling the 21cm global signal from first stars and black holes

Thesis supervisor:
Prof. Michela Mapelli

Candidate:
Emanuele Maria Ventura

Thesis co-supervisor:
Prof. Raffaella Schneider

Academic Year 2020-2021

Contents

1 Introduction

Looking at the history of our Universe, in the past few decades we have obtained a lot of information about conditions of the early Universe, through an extensive study of Cosmic Microwave Background (CMB) observations (Planck [110],[111]). Also the formation and properties of local structures are well understood thanks to the large number of surveys done with many telescopes observing at different wavelengths. However, there is still a crucial gap in the history of the Universe: how did the first luminous objects form? What was their impact on structure formation? The epoch between the last scattering surface of the CMB and formation of first stars (approximately between $z \sim 1000$ and $z \sim 30$) is commonly referred to as "Dark Ages". Another important event in the history of our Universe, which is still largely unconstrained, is the cosmic reionization of the intergalactic medium (IGM); this approximately ended at $z \sim 6$. Dark ages and the era of "first lights" (also known as "cosmic dawn") have not been observed yet, this is why they are considered the next frontier of observational cosmology. With the advent of new generation of telescopes such as the "James Webb Space Telescope" (JWST) and the "Extremely Large Telescope" (ELT), as well as the new generation of gravitational wave detectors (Einstein telescope, LISA) there is some chance to put new constraints on these epochs. One of the most promising tools to investigate Universe between $z \sim 50$ (growth of earliest structures) and $z \sim 6$ (complete reionization) is the redshifted 21-centimeter line of HI. Since this is a spectral line, the measure of the Doppler shift traces the 3D history of the IGM which contains the majority of baryonic matter. In order to make robust theoretical predictions of the 21-centimeter signal we need to have a clear picture of the processes that drive the evolution of the Universe during Dark Ages and the era of first lights. The following subsections are devoted to explain: how structures formed and evolved during these epochs (1.1), which mechanisms allowed the formation of luminous objects (1.2), how these sources were able to completely reionize the Universe (1.3) and through which processes first stars influenced the evolution of the IGM (1.4).

1.1 Structure evolution

Before describing the formation and evolution of first structures,we provide here a brief summary of parameters and relations typical of modern cosmology.
The standard model of cosmology (ΛCDM), considers an isotropic, homogeneous and expanding universe, in which the major energy contribution is given by dark energy (responsible for the accelerated expansion), and the majority of matter can be found in the form of Cold Dark Matter. To describe such a spacetime the metric used is the Robertson-Walker one usually written using spherical coordinates (R, Θ, Φ):

$$ds^2 = dt^2 - a^2(t)\left[\frac{dR^2}{1-kR^2} + R^2(d\Theta^2 + \sin^2\Theta d\Phi^2)\right] \tag{1}$$

a(t) is the scale factor, it defines the Hubble constant $H(t) = \frac{\dot{a(t)}}{a(t)}$ that describes the rate of expansion in time; k is a constant that indicates the curvature of the Universe

(positive/negative/null if closed/open/flat universe). Solutions of Einstein field equations for this metric give the Friedmann equation:

$$H^2(t) = \frac{8\pi G}{3}\rho - \frac{k}{a^2} \tag{2}$$

that together with the equation of energy conservation:

$$d(\rho R^3) = -pd(R^3) \tag{3}$$

relates the expansion of the Universe to its energy-matter content. Taking k=0 in Eq. (2) the critical density is defined:

$$\rho_c(t) = \frac{3H^2(t)}{8\pi G} \tag{4}$$

The contribution of each source (matter, radiation, vacuum etc.) with respect to the critical density is: $\Omega_i = \frac{\rho_i}{\rho_c}$, using these density parameters for each energy source in the Universe (matter, radiation, dark energy and curvature), Eq. (2) becomes:

$$H(t) = H_0\left[\frac{\Omega_m}{a^3} + \Omega_\Lambda + \frac{\Omega_r}{a^4} + \frac{\Omega_k}{a^2}\right]^{1/2} \tag{5}$$

Rather than the cosmic time dependence, it is mostly used the redshift dependence that can be easily obtained remembering that $a(t) \propto \frac{1}{1+z}$. Throughout this work it will be used the expression for H(z) valid at high redshifts (only Ω_m and Ω_Λ):

$$H(z) = H_0[\Omega_m(1+z)^3 + \Omega_\Lambda]^{1/2} \tag{6}$$

According to the Hot Big Bang model the Universe was initially hotter and radiation dominated. As expansion proceeds, due to adiabatic cooling, matter started to dominate at $z \sim 10^4$. When this transition occurred, the Universe was still hot enough to keep the gas ionized, but at $z \sim 1200$, temperature dropped below 3300K and hydrogen recombined. Hydrogen recombination allowed photons to decouple from matter and travel freely until our telescopes: this is when the most ancient source we observe (the CMB) is generated.
At our epochs the local universe shows a rich hierarchical pattern of galaxy clustering. However, CMB observation, prove that the Early Universe (or at least at the epoch of recombination) was almost smooth with only small density fluctuations (the measured fractional amplitude is of 10^{-5}). With the evolution of the Universe, due to gravitational instability the initial over-dense regions accrete additional matter at the beginning linearly, until non-linear concentrations of mass are formed allowing galaxies and clusters formation [109].

1.1.1 Linear Growth

As seen above, at recombination we may consider a flat universe matter dominated background with uniform matter density $\bar{\rho}$ and, on top of this, some small perturbations

with fractional amplitude $|\delta| << 1$ where $\delta = \frac{\varrho}{\bar{\rho}} - 1$. This justifies the perturbative approach adopted in the following. If the mean free path of a particle is small, matter can be treated as an ideal fluid and its behaviour is governed by these three equations which are known respectively as continuity equation, Euler equation and Poisson equation [119].

$$\left.\frac{\partial \rho}{\partial t}\right|_{\bar{r}} + \bar{\nabla}_{\bar{r}}(\rho \bar{v}) = 0 \tag{7}$$

$$\left.\frac{\partial \bar{v}}{\partial t}\right|_{\bar{r}} + (\bar{v} \cdot \bar{\nabla}_r)\bar{v} + \frac{1}{\rho}\bar{\nabla}_{\bar{r}} p + \bar{\nabla}_{\bar{r}}\Phi = 0 \tag{8}$$

$$\nabla^2_{\bar{r}}\Phi = 4\pi G\rho \tag{9}$$

Where ρ is matter density, Φ gravitational potential and p is pressure. In this vector notation the fixed coordinate $\bar{r}$ corresponds to a comoving position $\bar{x}$ through $\bar{r}$(t)=a(t)$\bar{x}$(t). From this relation it follows that: $\bar{v}$=$\dot{\bar{r}}$=H$\bar{r}$+$\bar{u}$,
$\left.\frac{\partial f}{\partial t}\right|_{\bar{r}} = \left.\frac{\partial f}{\partial t}\right|_{\bar{x}} - H(\bar{r} \cdot \nabla_{\bar{r}})f$ and $\nabla_{\bar{r}} = \frac{1}{a}\nabla_{\bar{x}}$

with $\bar{u}$=a$\dot{\bar{x}}$ peculiar velocity which represents departures of matter motion from pure Hubble expansion. ϕ is the peculiar Newtonian gravitational potential which is the fluctuations in potential with respect to the homogeneous background. Historically, one of the first analytical methods to study the evolution of density perturbations was based on applying perturbation theory (PT) to the hydrodynamical description just seen. First-order Eulerian PT is often referred as "linearized fluid approach" and has the big advantage to be a simple but robust approach until we consider large scales where density fluctuations are much smaller than the mean density ($\rho << \rho_0$)[8]. With this "linearized fluid approach" the three dynamical equations for a self-gravitating fluid Eqs. (7), (8) and (9) can be rewritten in terms of perturbed quantities $(\delta, \bar{u}, \phi)$ dropping all the terms of 2^{nd} order and higher:

$$\left.\frac{\partial \delta}{\partial t}\right|_{\bar{x}} + \frac{1}{a}\bar{\nabla}_{\bar{x}} \cdot [(1+\delta)\bar{u})] = 0 \tag{10}$$

$$\left.\frac{\partial \bar{u}}{\partial t}\right|_{\bar{x}} + H\bar{u} + \frac{1}{a}(\bar{u} \cdot \bar{\nabla}_{\bar{x}})\bar{u} = -\frac{1}{a\rho}\bar{\nabla}_{\bar{x}} p - \frac{1}{a\bar{\rho}}\bar{\nabla}_x \phi \tag{11}$$

$$\nabla^2_x \phi = 4\pi G a^2 \delta\bar{\rho} \tag{12}$$

To solve this system is convenient to go in Fourier space and differentiate Eq. (10); doing so, after some mathematical steps we obtain:

$$\ddot{\delta}_k + 2H\dot{\delta}_k + [\frac{c_s^2 k^2}{a^2} - 4\pi G\bar{\rho}]\delta_k = 0 \tag{13}$$

Where c_s^2 is square adiabatic speed of sound and k is wave number. In Eq. (13) the term that contains the speed of sound is negligible for $k << k_J$, $k_J \equiv \frac{a\sqrt{4\pi G\rho_0}}{c_s}$. In this regime (note that this condition is always fulfilled if we consider a collisionless system since p=0

$\implies c_s = 0 \implies \mathrm{k}_J \to \infty$ Eq. (13) becomes easy to solve and will depend on the choice of cosmological parameters. Considering a flat, matter-dominated Universe Eq. (13) admits two linearly independent solutions that are labelled as "growing mode" ($\delta_{(+)} \propto t^{2/3}$, $v_{(+)} \propto t^{1/3}, \phi_{(+)} = cost$) and "decaying mode" ($\delta_{(-)} \propto t^{-1}, v_{(-)} \propto t^{-4/3}, \phi_{(-)} \propto t^{-5/3}$). The one of our interest is the growing mode because it dominates the density evolution. So at early times, as long as $\delta << 1$ a density perturbation maintains its shape in comoving coordinates ($\bar{x}$) and grows in amplitude in proportion to a growth factor D(t). The expression of this factor depends on the adopted cosmology, choosing a standard in which there is only matter and cosmological constant so that $\Omega_m + \Omega_\Lambda = 1$ then [5]:

$$D(t) \propto \frac{(\Omega_\Lambda a^3 + \Omega_m)^{1/2}}{a^{3/2}} \int_0^a \frac{a'^{3/2} da'}{(\Omega_\Lambda a'^3 + \Omega_m)^{3/2}} \tag{14}$$

$$D(z) = \frac{5\Omega_m(z)}{2}[\Omega_m(z)^{4/7} - \Omega_\Lambda(z) + (1 + \Omega_m(z)/2)(1 + \Omega_\Lambda(z)/70)]^{-1} \tag{15}$$

With

$$\Omega_m(z) = \frac{\Omega_m(1+z)^3}{\Omega_m(1+z)^3 + \Omega_\Lambda} \tag{16}$$

$$\Omega_\Lambda(z) = \frac{\Omega_\Lambda}{\Omega_m(1+z)^3 + \Omega_\Lambda} \tag{17}$$

Once we have the time (or redshift) evolution for different Fourier modes, it is straightforward to compute the evolution of the density field as this is a sum of a complete set of periodic Fourier modes each of them evolving independently (as long as we are in a linear regime).
In order to look for the formation of first structure, not only we need to know the time evolution of perturbations but also their spatial dependence is crucial. The amplitude of initial perturbations varies with scale (large-scale regions have smaller amplitude than smaller scales). In the modern picture of cosmology, initial perturbations are generated by inflation and are distributed according to a Gaussian random field [83]. For this reason their description is quite simple in Fourier space where different $\bar{k}$-modes are statistically independent.

$$\delta_{\bar{k}} = \int d^3x \delta(x) e^{i\bar{k}\cdot\bar{x}} \tag{18}$$

As commonly indicated, $\bar{k}$ is the comoving wavevector whose amplitude is given in terms of the wavelength by $k = 2\pi/\lambda$. Our observations cannot follow the evolution of an individual density mode, this is why we are mostly interested in their statistical properties. These are determined by the variance of the amplitude of different k-modes which are described in terms of the power spectrum $P(\bar{k})$ adopting the usual definition in terms of the correlation function:

$$< \delta_{\bar{k}} \delta^*_{\bar{k}} >= (2\pi)^3 P(\bar{k}) \delta^{(3)}(\bar{k} - \bar{k}') \tag{19}$$

According to standard models, inflation produces a simple power-law spectrum $P(k) \propto k^{n_s}$ with $n_s \simeq 1$ (nearly scale-invariant power spectrum) [83] [88]. As perturbations grow in time, the power spectrum becomes more complex. In particular this is characterized by *(i)* a turnover at the horizon scale (cH^{-1}) at matter-radiation equality resulting from the fact that density perturbations experience almost no growth during the radiation-dominated era and *(ii)* a small-scale asymptotic shape of $P(k) \propto k^{n_s-4}$. After matter-radiation equality P(k) is parameterized by a transfer function that accounts for changes in the shape of the dark matter power spectrum [88] [38]. It is defined as:

$$P(k,z) = T^2(k)\frac{D^2(z)}{D^2(z_{eq})}P_{pri}(k) \tag{20}$$

where $P_{pri}(k)$ is the primordial power spectrum and z_{eq} is the redshift of matter-radiation equality. Various forms of T(k), accounting for different effects of baryons and CDM, have been discussed by Eisenstein & Hu (1998, 1999) [38] [39]. The only quantity which is not determined by current models of inflation is the overall amplitude of the power spectrum, and thus this must be set by observations (observed CMB temperature fluctuations or local measures of large-scale structure). The most popular normalization adopted is through the observed mass fluctuation amplitude at the present day on $8h^{-1}$Mpc (the scale of galaxy clusters) [5]. The meaning of this choice will be clear in a moment.
To determine the formation of objects of given mass (or size) it is useful to consider the distribution of the smoothed density field defined as $\int d^3r\delta(\bar{x})W(\bar{r})$ where $W(\bar{r})$ is a window function normalized so that $\int d^3rW(\bar{r}) = 1$. Considering masses inside spheres of radius R it is used a "spherical top-hat" window in which W=1 inside the sphere and is null outside; with this choice the smoothed density field measures fluctuations in the mass inside a sphere of radius R, it is denoted by δ_R or δ_M where the enclosed mass M is related to the comoving radius R by $M = 4\pi\bar{\rho}_m R^3/3$ with $\bar{\rho}_m$ is the current mean matter density. The variance $< \delta_M^2 >$ is then:

$$\sigma^2(M) = \sigma^2(R) = \int_0^\infty \frac{dk}{2\pi^2}k^2P(k)\left[\frac{3j_1(kR)}{kR}\right]^2 \tag{21}$$

where $j_1 = (\sin x - x\cos x)/x^2$. As written above, to describe the normalization of the overall amplitude of the power spectrum the value of $\sigma_8 = \sigma(R = 8h^{-1}Mpc)$ is inferred from observations.

1.1.2 Formation of nonlinear objects

As already stressed, the above treatment is no longer valid when $\delta \sim 1$, at this point the full non-linear gravitational problem must be considered. In our standard cosmology dark matter is "cold" so that pressure forces are null, making the nonlinear evolution entirely dependent on gravitational forces. Considering an isolated, spherically symmetric density perturbation, the trajectory of a test particles at radius r relative to the center of symmetry can be followed beyond linear regime. These extrapolations beyond linear theory (like Zel'dovich approximation [138] [171]) are valid until the particle crosses

paths with one from a different radius (this event is called "shell crossing"); this happens rather late for most initial conditions. Another useful simplification can be done if a region much smaller than the horizon is considered: in this case we can put ourselves in a Newtonian framework. Having in mind these assumptions, it is now possible to study the problem of the halo formation. At some early epoch, a top-hat of uniform overdensity $\delta_i = \delta(t = t_i)$ inside a sphere of radius R is considered. The collapse of this spherical top-hat perturbation is described by the simple Newtonian equation with a correction for the cosmological constant:

$$\frac{d^2r}{dt^2} = H_0^2\Omega_\Lambda r - \frac{GM}{r^2} \tag{22}$$

note that r is the radius in a fixed coordinate frame, $M = (4\pi/3)r_i^3\bar{\rho}_i(1+\delta_i)$ is the total mass enclosed within radius r. To solve Eq. (22), a dimensionless radius $x = a_i(r/r_i)$ is defined and a flat universe is considered. What is found is that δ grows initially as $\delta_L = D(t)/D(t_i)$ in accordance with linear theory, at later times δ grows above δ_L. So if the mass shell is bound (Newtonian energy is negative), it will expand reaching a maximum radius after which it will collapse. When the top-hat collapses to a point the predicted overdensity is $\delta_L = 1.686$, while at turnaround (the time at which the halo reached its maximum radius) $\delta_L = 1.063$ [5]. So, in order to collapse at redshift z, a top-hat must have a linearized overdensity extrapolated to the present day of:

$$\delta_{crit}(z) = \frac{1.686}{D(z)} \tag{23}$$

where D(z) is the linear growth factor defined in Eq. (15) setting $D(z = 0) = 1$. This derivation has been done considering the simplest possible case (spherical, top-hat overdensity), because the dynamical collapse of a dark matter halo can be solved analytically only if a particular symmetry is present. Nevertheless, as it will be shown briefly, these results turned out to be extremely useful to understand the properties and distribution of cold dark matter halos.

So far, we have stated that a spherical region collapses to a point, but a small violation of the exact symmetry (we do not expect perfect symmetry in the real world) is sufficient to prevent the top-hat to entirely collapse. The halo instead reaches a state of virial equilibrium through violent dynamical relaxation. To find the final overdensity when the halo is virialized it is necessary to use the virial theorem $U = -2K$ (valid for the final state of the collapsed halo). Assuming that virialization occurs at twice the turnaround time (corresponding to the moment at which the spherical perturbation would otherwise collapse completely) and a flat, matter dominated universe ($a \propto t^{2/3}$), the final density of the virialized halo relative to the critical density is:

$$\Delta_c(\Omega_m = 1) = \frac{\rho_{vir}(z_{vir})}{\bar{\rho}_{crit}(z_{vir})} = 18\pi^2 \simeq 178 \tag{24}$$

Considering instead a flat universe in which $\Omega_m + \Omega_\Lambda = 1$ the above equation is modified by the following fitting formula found by Bryan & Norman (1998) [19]:

$$\Delta_c = 18\pi^2 + 82d - 39d^2 \tag{25}$$

with $d = \Omega_m(z) - 1$ ($\Omega_m(z)$ is defined in Eq. (17)). Armed with Eq. (25) it is now possible to find the physical quantities of the virialized dark matter halos. In particular a halo of mass M collapsing at redshift $z >> 1$ has a virial radius (r_{vir}), a circular velocity (V_c) and a virial temperature (T_{vir}) of [88]:

$$r_{vir} = 0.784\left[\frac{\Omega_m}{\Omega_m(z)}\frac{\Delta_c}{18\pi^2}\right]^{-1/3}\left(\frac{M}{10^8 M_\odot}\right)^{1/3}\left(\frac{1+z}{10}\right)^{-1} h^{-2/3} kpc \quad (26)$$

$$V_c = \left(\frac{GM}{r_{vir}}\right)^{1/2} = 23.4\left[\frac{\Omega_m}{\Omega_m(z)}\frac{\Delta_c}{18\pi^2}\right]^{1/6}\left(\frac{M}{10^8 M\odot}\right)^{1/3}\left(\frac{1+z}{10}\right)^{1/2} h^{1/3} kms^{-1} \quad (27)$$

$$T_{vir} = \frac{\mu m_p V_c^2}{2k_B} = 1.98x10^4\frac{\mu}{0.6}\left[\frac{\Omega_m}{\Omega_m(z)}\frac{\Delta_c}{18\pi^2}\right]^{1/3}\left(\frac{M}{10^8 M\odot}\right)^{2/3}\left(\frac{1+z}{10}\right)h^{2/3} K \quad (28)$$

In these expressions the Hubble constant H_0 is written in terms of the Hubble parameter h as $H_0 = 100h$ kms$^{-1}Mpc^{-1}$. μ is the mean molecular weight which depends on the ionization fraction of the gas (typical values are 0.59 for a fully ionized gas, 0.61 for a gas with ionized hydrogen but only singly ionized helium and 1.22 for a fully neutral gas), m_p is the proton mass. Going deeply in the physics governing the formation of halos, we must consider that structure formation in cold dark matter models proceeds hierarchically: low-mass halos are the first ones to form and after having accreted and merged together form high-mass halos (this is referred as "bottom-up evolution" [53]). Results of numerical simulations give a spherically averaged density profile of a dark matter halo, this profile is known as NFW (Navarro-Frank-White) and has the approximate form of [104]:

$$\rho(r) = \frac{3H_0^2}{8\pi G}(1+z)^3\frac{\Omega_m}{\Omega_m(z)}\frac{\delta_c}{c_N x(1+c_N x)^2} \quad (29)$$

with $x = r/r_{vir}$ and the characteristic density δ_c is linked to the concentration parameter c_N through

$$\delta_c = \frac{\Delta_c}{3}\frac{c_N^3}{ln(1+c_N) - c_N/(1+c_N)} \quad (30)$$

Typical values of c_N are ~ 4 for newly collapsed halos and larger values at later times (it depends strongly on the formation redshift, weakly on the halo mass M [88]).
Having characterized the properties of individual halos, in order to have a picture of global structure formation in our universe, what is left to estimate is the number density of halos as a function of mass for different redshifts. To achieve this goal, a simple but effective model has been developed by Press and Schechter [113]. To determine the abundance of halos at redshift z we use the definition of δ_M introduced in Eq. (21). δ_M is distributed as a Gaussian variable with zero mean and standard deviation $\sigma(M)$, so the probability that δ_M is larger than a fixed δ is:

$$\int_\delta^\infty \frac{1}{\sqrt{2\pi}\sigma(M)}\exp\left[-\frac{\delta_M^2}{2\sigma^2(M)}\right] = \frac{1}{2}erfc\left(\frac{\delta}{\sqrt{2}\sigma(M)}\right) \quad (31)$$

In the Press-Schechter formalism, this probability is identified with the fraction of dark matter particles that are part of a collapsed halo of mass greater than M at redshift z,

so with this procedure the abundance of halos at redshift z is determined counting the number of density peaks per unit volume (such density peaks correspond to virialized objects and under the assumption of a Gaussian random field of density perturbations). In order to make this ansatz reasonable we need to use δ_{crit} (defined in Eq. (23)) as a value of δ and we also have to consider that even regions with $\delta_M < 0$ can be part of collapsed objects (this ends up in multiplying by 2 the factor in Eq. (31)). Thus we obtain the final formula for the mass fraction in halos above M at redshift z, also known as *collapse fraction*.

$$f_{coll}(> M|z) = erfc\left(\frac{\delta_{crit}(z)}{\sqrt{2}\sigma(M)}\right) \tag{32}$$

Differentiating Eq. (32) yields the mass distribution. Being n(M)dM the comoving number density of halos of mass between M and M+dM it is possible to write:

$$\frac{dn}{dM} = \sqrt{\frac{2}{\pi}}\frac{\rho_m}{M}\frac{-d(\ln\sigma)}{dM}\nu_c e^{-\nu_c^2/2} \tag{33}$$

with $\nu_c = \delta_{crit}(z)/\sigma(M)$ the number of standard deviations which the critical collapse overdensity represents on mass scale M (the higher is ν_c the less likely a halo of mass M will form). Hence, the halo abundance depends basically on cosmological parameters (through $\sigma(M), \delta_{crit}(z)$ and ρ_m); just as an example here are shown some plots. To make these plots, it has been chosen the following set of cosmological parameters: $\Omega_m = 0.3$, $\Omega_\Lambda = 0.7, \Omega_b = 0.045, \sigma_8 = 0.9$, h=0.7, n=1. This choice is in accordance with the one of the review made by Barkana & Loeb (2001) [5] in order to be sure that these results are consistent with the ones in their work. Throughout this work, the Press-Schechter formalism will be adopted, anyway it is worth to mention that this is not the only possible formalism. Another popular choice is to take the Sheth-Tormen mass function that, instead of a spherical collapse, considers a more accurate physical description of the collapse: the ellipsoidal collapse [137].

1.1.3 Baryonic objects

Understanding how dark matter structures build up and evolve is the starting point to understand how the first luminous objects are formed; cold dark matter halos are the building blocks within which the formation of luminous objects (such as stars, galaxies, quasars etc.) occurs. These are made by baryons, and differently from dark matter, baryonic particles cannot be considered as a pressureless fluid. For this reason, in order to study the behaviour of a sphere of gas with a higher density with respect to the environment we have to consider not only gravity (as for the dark matter case) but also the pressure gradient of the gas. Remaining in the context of Newtonian gravity, the standard stability criterion against perturbation is set by the *Jeans mass*:

$$M_J = \frac{4\pi}{3}\rho\left(\frac{\lambda_J}{2}\right)^3 \tag{34}$$

with $\lambda_J = \frac{\pi c_s^2}{G\rho}$ the Jeans length for a static, infinite uniform gas of density ρ and sound speed c_s. λ_J represents the critical wavelength that separates oscillatory from growing

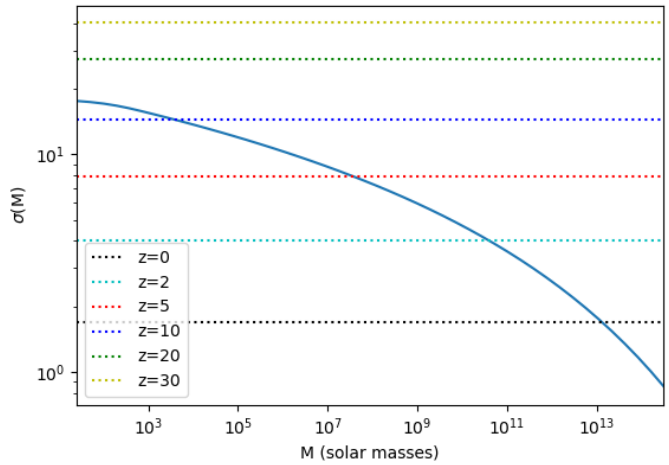

Figure 1: The light blue solid line shows $\sigma(M)$ vs M (in solar mass units). The horizontal dotted lines show δ_{crit} for different values of z. As it can be seen, going at later times (lower z), δ_{crit} becomes lower due to the increasing value of the growth factor D(z). Thus, at earlier times it is favoured the formation only of low-mass halos (they have the lower values of ν_c). Moving to the present, the formation of massive halos can also occur since δ_{crit} decreases making ν_c lower also for higher masses.

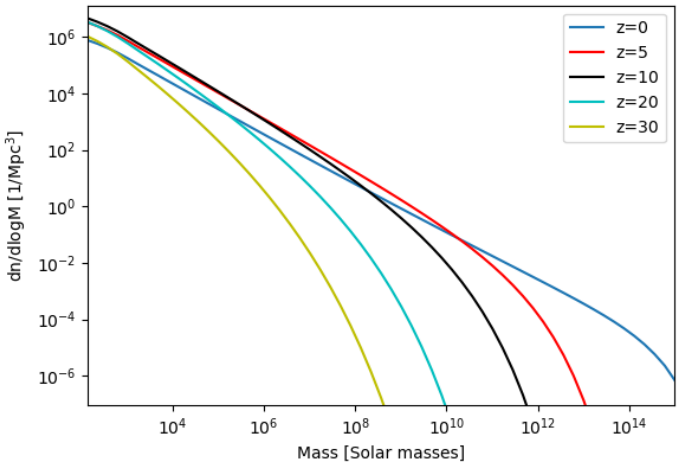

Figure 2: Halo mass function at several redshifts taking $\nu_c = 1$ (so we are considering halo formation with 1-σ standard deviation). At z=30, the yellow curve shows that only low-mass halos form, moving to lower redshifts the formation of more massive halos is expected.

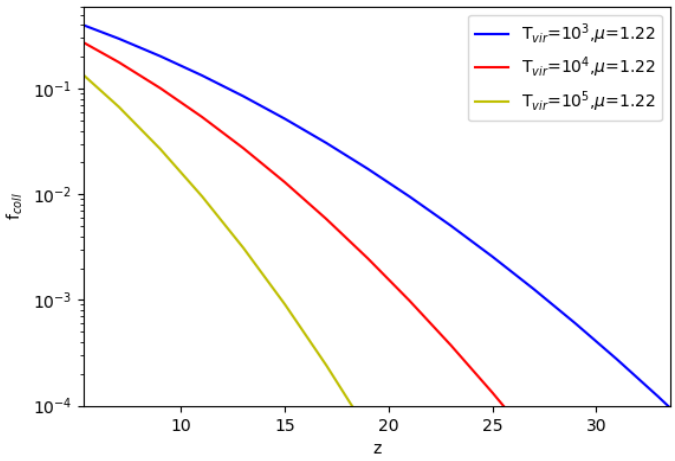

Figure 3: Collapse fraction as a function of redshift for different values of mass. Mass values are expressed specifying the virial temperature and μ. Therefore M is expressed as a function of T_{vir} and μ by inverting Eq. (28). A higher value of T_{vir} corresponds to a more massive halo. Thus, as expected the collapse fraction is systematically lower for higher T_{vir}.

density perturbations [77]. A perturbation with $M > M_J$ is unstable against gravitational collapse as pressure forces are not able to counterbalance this density perturbation. The derivation of the Jeans mass is not formally correct and it does not consider an expanding background [5] [88], however it is possible to carry out this derivation in a cosmological context (in this case the expansion of the background slows down the exponential growth of perturbation). Without going in the details of the derivation, assuming a mixture of dark matter and baryons with density parameters Ω_b and Ω_{dm} such that $\Omega_b + \Omega_{dm} = \Omega_m$ and taking spatial fluctuations in the gas and dark matter densities as a single spherical Fourier mode it is possibile to find [88]:

$$k_J = (2\pi/\lambda_J) = [2k_b T_{\gamma,0}/3\mu m_p]^{-1/2}\sqrt{\Omega_m}H_0 \tag{35}$$

that yields:

$$M_J = 1.35 \cdot 10^5 \left(\frac{\Omega_m h^2}{0.15}\right)^{-1/2} M_\odot \tag{36}$$

Notice that Eq. (36) is redshift independent (actually this is valid for perturbations in the early universe). Just for completeness it is worth to mention another critical mass related to baryonic perturbations: the *Filtering mass*. Jeans mass is indeed related only to the evolution of perturbations at a given time, but if the Jeans mass itself varies with time, the overall suppression of the growth of perturbations must depend on a time-averaged Jeans mass. This time-averaged Jeans mass found by Gnedin & Hui (1998) [58] is called Filtering mass (M_F), a more detailed discussion can be found in section 1.4.1.

In conclusion, considering both dark matter and baryons, linear and non-linear gravitational growth we end up with the following scenario: due to the growth of density perturbations, cold dark matter collapses and virializes forming halos. Baryonic particles fall inside these dark matter halos (dark matter potential wells) until a minimum mass (Jeans or Filtering mass) is reached. From this moment on, pressure forces of baryons are not able to maintain the hydrostatic equilibrium and so the gas starts to collapse leading to the formation of the very first luminous structures in the Universe [88].

1.2 Cooling mechanisms

In the previous section, the discussion was entirely devoted to the gravitational evolution of the matter content of the Universe, that led to the formation of dark matter halos inside which the gas is able to collapse. In order to have star formation, not only we need the gas to collapse but it is also necessary that gas cools down so that gas can fragment into stars [88]. Thus, there are two thresholds masses that enables star formation: one related to the collapse already discussed and the other related to cooling that will be the main subject of this section. Here after, stars are considered to form out of primordial gas inside low-mass dark matter halos without any influence from other structures such as stars or black holes, the population of stars forming such under conditions is referred in [88] as Pop.III.1 stars.
The main products of Big Bang Nucleosynthesis are Hydrogen ($\sim 76\%$), Helium ($\sim 24\%$) and few traces of Lithium. Heavier elements are produced by nuclear reactions inside star cores so it is reasonable to expect that the first molecule to form in the early universe is molecular hydrogen H_2. A complete set of reactions that lead to the formation of H_2 is reviewed by Abel & Haiman (2000) [1] the dominant of which are:

$$H + e^- \rightarrow H^- + h\nu \tag{37}$$

$$H^- + H \rightarrow H_2 + e^- \tag{38}$$

Electrons act as a catalyst so in regions rich of e^- H_2 is produced faster and more abundantly. Molecular hydrogen can be rotationally or vibrationally excited through a collision with another particle; when the subsequent de-excitation is radiative, the cloud loses energy and it cools down (if instead there are collisional de-excitations no cooling occurs). During the initial phase of the collapse, at relatively low densities, radiative de-excitation dominates. We can express the condition to have star formation requiring that (molecular) cooling must occur faster than the timescale over which the halo accumulates more thermal energy. A commonly used approximation for the cooling time is [151]:

$$t_{cool} = 5 \cdot 10^4 f_{H_2} \left(\frac{1+z}{20}\right)^3 \left(\frac{\delta}{200}\right) \left(1 + \frac{10 T_3^{7/2}}{60 + T_3^4}\right)^{-1} \exp\left(\frac{512K}{T}\right) yr \tag{39}$$

where $T_3 = T/(10^3 K)$ and f_{H_2} is the molecular fraction. This timescale must be compared with the dynamical timescale ($t_{dyn} \simeq 1/\sqrt{G\rho}$) that describes how rapidly hydrostatic equilibrium is restored. Applying this criterion it turns out that molecular cooling

is effective inside halos with virial temperatures $T_{vir} \geq 10^3$K [5]. This result justifies the future choice of considering as star forming halos, those that have a mass greater than $m_{min} = m_3$ with m_3 equal to the mass corresponding to a $T_{vir} = 10^3$K using Eq. (28). Molecular hydrogen, however, is a very fragile molecule that can be easily photo-dissociated by UV photons in the *Lyman-Werner band* (between 11.26-13.6 eV). Photodissociation is a two-step process known as *Solomon process*; details about this process can be found in Stecher & Williams (1967) [145]. This mechanism has a key importance in the evolution of structure formation because soft-UV photons are likely produced by first stars. Soon after the first star formation, H_2 abundance is expected to decrease drastically so that molecular cooling cannot be anymore an efficient cooling channel. Luckily there is another efficient cooling mechanism: atomic cooling. This is effective only inside halos with $m \geq m_{min} = m_4$ with m_4 equal to the mass corresponding to a $T_{vir} = 10^4$K [65] [25]. Together with molecular cooling, throughout this work it will be widely adopted this mass threshold for star forming halos.

1.3 Reionization

Once the first sources appeared in the Universe, they had a strong impact on the IGM and on subsequent star formation. Their effects are commonly referred to as "feedback" processes and an example of these is the H_2 photo-dissociation discussed above. In the next section, all these processes will be shortly reviewed. Here, instead the main focus is on an event that strongly influenced the history of our Universe: cosmic reionization. This event is mainly studied through Lyα forest observations and in particular quasar absorption spectra suggest that the IGM was completely ionized at z $\sim$ 6 [53]. To study the evolution of reionization, it is commonly used the average ionized fraction $\bar{x}_i(z)$: soon after recombination $\bar{x}_i \sim 0$ while when reionization is completed $\bar{x}_i \sim 1$. To ionize hydrogen, photons with E $\geq$ 13.6eV (or $\lambda \leq$ 912 A) are needed; such UV photons are emitted by the first stars (in principle both stars and accretion disks onto black holes could produce ionizing photons, but here we will assume that only stars drive reionization because observations indicate that quasars were rare at $z > 6$ [53].) The impact of accreting BHs on the reionization history will be considered starting from Section 3. Stellar ionizing photons are supposed to be only slightly more energetic than 13.6 eV so, once they reach a region full of neutral hydrogen they will be absorbed efficiently once. In this scenario, the Universe will be constituted by a two-phase IGM [88]: "bubbles" of ionized gas around stars will be immersed in neutral hydrogen region. as reionization proceeds, these bubbles will occupy larger regions. For this reason in some studies, $\bar{x}_i$ is called "filling factor" (i.e. the fraction of the volume of the Universe inside HII regions) and in this case is denoted as Q_{HII} [5]. In this picture it is possible to compute how each bubble grows in time. Assuming for the moment that there are no recombinations so each hydrogen atom needs to be ionized only once. The ionized proper volume V_p will be:

$$V_p = \frac{Q_i}{\bar{n}_H} \tag{40}$$

where $\bar{n}_H$ is the mean number density of hydrogen and Q_i is the total number of ionizing photons (produced by the source). To obtain a rough estimate of Q_i, consider a halo of mass M and a baryon fraction of Ω_b/Ω_m. Let us call star formation efficiency $f_\star$ the efficiency at which baryons are incorporated into stars, escape fraction f_{esc} the amount of ionizing radiation escaping from the host galaxy and N_{ion} the number of ionizing photons per baryon inside stars. These quantities are collected together and determine the ionizing efficiency ζ [88]:

$$\zeta = f_\star f_{esc} N_{ion} \tag{41}$$

Typical values of ζ vary strongly with the stellar population considered, at the end of this section each of these parameters just introduced will be deeply discussed. The total number of ionizing photons produced by the source is:

$$Q_i = \left(\zeta \frac{\Omega_b}{\Omega_m} \frac{M}{m_p}\right)^{1/3} \tag{42}$$

So far, in the problem of the evolution of an expanding HII bubble, both recombination and expansion of the Universe have been neglected. If we consider only recombinations, the problem is identical to the one of the Strömgren sphere (HII regions produced by early-type stars embedded in the interstellar medium [146]). In such a case the ionized proper volume is:

$$V_p = \frac{\dot{Q}_i}{\alpha_B \bar{n}_H^2} \tag{43}$$

where the recombination rate is given by $\alpha_B \bar{n}_H^2$ with α_B is the case-B recombination coefficient (it ignores recombinations to the ground state which generate a new ionizing photon and so do not change the net ionized fraction [88]) and $\alpha_B = 2.6 \times 10^{-13} cm^3 s^{-1}$ for H at $T = 10^4$K. The exact evolution of an expanding HII region that includes also cosmological expansion is given by the following equation [134]:

$$\bar{n}_H \left(\frac{dV_p}{dt} - 3HV_p\right) = \dot{Q}_i - \alpha_B < n_H^2 > V_p \tag{44}$$

In this equation, the mean density varies with the scale factor: $\bar{n}_H \propto a^{-3}(t)$. It is important to highlight the fact that recombinations scale with the square of the density and the angular brackets denote a volume average. As a consequence, if the IGM is not uniform (as it is) with ionized gas in high-density clumps, the recombination time will be shorter than the case of uniform IGM. This dependence is dealt with introducing the clumping factor C:

$$C = < n_H^2 > / \bar{n}_H^2 \tag{45}$$

Together with ζ, also this factor will be extensively discussed soon. Assuming that the ionized volume is much larger than the scale of clumping and so clumps can be averaged out, Eq. (44) can be solved by specifying C. Moving from the proper volume to a comoving one we obtain:

$$\frac{dV}{dt} = \frac{1}{\bar{n}_H^0} \dot{Q}_i - \alpha_B \frac{C}{a^3} \bar{n}_H^0 V \tag{46}$$

with the present number density of Hydrogen $\bar{n}_H^0 \sim 0.76\bar{n}_b^0$. Eq. (46) can be solved exactly; taking a source that turns on at t= t_i:

$$V(t) = \int_{t_i}^{t} \frac{1}{\bar{n}_H^0} \frac{dQ_i}{dt'} e^{F(t',t)} dt' \tag{47}$$

$$F(t',t) = -\alpha_B \bar{n}_H^0 \int_{t'}^{t} \frac{C(t'')}{a^3(t'')} dt'' \tag{48}$$

Eq. (48) can be simplified assuming a constant C, a flat universe and high redshift [88]:

$$F(t',t) = -\frac{2}{3} \frac{\alpha_B \bar{n}_H^0}{\sqrt{\Omega_m} H_0} C[f(t') - f(t)] \tag{49}$$

$$f(t) = \sqrt{\frac{1}{a^3} + \frac{1-\Omega_m}{\Omega_m}} \tag{50}$$

With these equations the evolution of a single ionized bubble is entirely computed. The next step is to compute the average ionized (or neutral) fraction across the entire Universe: the filling factor Q_{HII}. To find this, the procedure is quite similar to the one used to derive the evolution of the volume of ionized bubbles. Accounting for ionizations we just need to consider the number of photons produced per baryon by the first sources. Thus, remembering that the first sources form in collapsed dark matter halos and the definition of ζ to account for ionizing efficiency it is possible to write:

$$Q_{HII} = \zeta f_{coll} \tag{51}$$

This expression does not account for recombinations and assumes that ionizing photons are produced instantaneously. Remember also that the value of f_{coll} depends on the mass function and on the threshold halo mass that allows star formation (as previously discussed, common choices are $m_{min} = m_4$ or $m_{min} = m_3$). The treatment of recombinations is exactly the same already done with the same definition for the clumping factor C, thus the redshift evolution of the filling factor is given by:

$$\frac{dQ_{HII}}{dz} = \zeta \frac{df_{coll}}{dz} + \alpha_B C \bar{n}_H^0 \frac{(1+z)^2}{H(z)} Q_{HII} \tag{52}$$

This equation is analogous to Eq. (46) sharing the same solution given by Eq. (47), with the only difference that Eq. (46) is expressed in terms of cosmic time t while Eq. (52) is expressed in terms of redshift z (in order to do this change of coordinate just remember that $a(t) = \frac{1}{1+z}$ and $\frac{d}{dz} = \frac{1}{H(z)(1+z)} \frac{d}{dt}$ with H(z) given by Eq. (6))
Now that the evolution of the average ionized fraction in the Universe is computed, it is worth to discuss a bit more the typical values of two key parameters that regulates the ionization history: ζ and C.

1.3.1 Ionizing efficiency

The ionizing efficiency ζ appears in Eq. (52) in the positive ionization term: the higher is ζ the more Q_{HII} increases. ζ is given by Eq. (41) thus depends on: star formation

efficiency $f_\star$, escape fraction f_{esc} and the number of ionizing photons N_{ion}. All these quantities are strongly related to the stellar population and for population II stars we are able to make robust estimate on these parameters; for population III stars (which have not been detected yet) parameter estimation is way more uncertain. Reasonable values for $f_\star$ for pop.II star can be estimated from observations in the local Universe; these tells us that $f_\star \sim 10\%$ [88] [5]. The only possible estimation for $f_\star$ in Pop.III stars can be done assuming that each halo can form only a single very massive star ($M_\star \geq 100 M_\odot$), thus $f_\star \sim (\Omega_m/\Omega_b) M_\star/M_{halo} < 10^{-3}$ [88]. This is only a very general estimation, larger values ($\sim 10^{-2}$) are often taken in literature (this corresponds to assuming that there is an inefficient metal dispersion together with a rapid starburst [53]). In general $f_\star$ for Pop.III is taken to be smaller than for pop.II.
For what concerns UV escape fraction, measurements in nearby galaxies and at moderate redshifts suggest that $f_{esc} \leq 0.06$ [10], but some studies predict that in high-z galaxies this value could be larger [91] [93]. Actually the UV escape fraction, shows a strong variance among galaxies and different systems; for example, quasars are expected to have larger f_{esc} since they concentrate all of their photons in one spatial location [53]. For these reasons, it is commonly chosen $0.05 \leq f_{esc} \leq 0.1$ [57] [74].
N_{ion} can be estimated starting from the initial mass function (IMF) and metallicity (Z). Usually Pop.III stars have an IMF shifted toward higher values of mass with respect to pop.II IMF [124]. Convenient approximations are $N_{ion} \sim 4000$ for Pop.II stars with Z=$0.05 Z_\odot$ [124] [80] and $N_{ion} \sim 40000$ for Pop.III stars [16]. As usual, the estimation for Pop.III has a large uncertainty (at least of a factor 2) due to the lack of observations of metal-free stars.
Putting together all these parameters, the ionizing efficiency can accept a quite big range of values (20-300) and only future observations can put more constraints. Finally, these factors that have been assumed constant, actually vary throughout reionization due to the fact that stars have a strong impact on the ISM/IGM and so on the subsequent star formation (e.g. molecular photodissociation mentioned in 1.2); all these effects are commonly referred to as "feedback mechanisms" and they will be discussed in Section 1.4.

1.3.2 Clumping factor

Even more problematic than ζ, is the estimation of the clumping factor C(z). Numerical simulations could be very useful but at the current state of the art we have not enough resolution on the smallest scales [53]. Particularly, the Jeans mass for the cold IGM is $< 10^5 M_\odot$; such a low mass allows the formation of dense gas clouds which are not able to cool (thus to form stars) due to their low mass. These structures are invisible to simulations of reionization which usually span ∼100 Mpc boxes in order to sample the large HII regions. Another not trivial problem, is that we need to trace the topology of both ionized and neutral gas since C(z) is evaluated over only the ionized gas [88]. If low-density gas is ionized first (it seems reasonable to think this) C<1 throughout most of reionization because dense gas will be locked up in neutral, self-shielded systems. But at the same time we know that, on large scales, ionizing sources form inside overdense

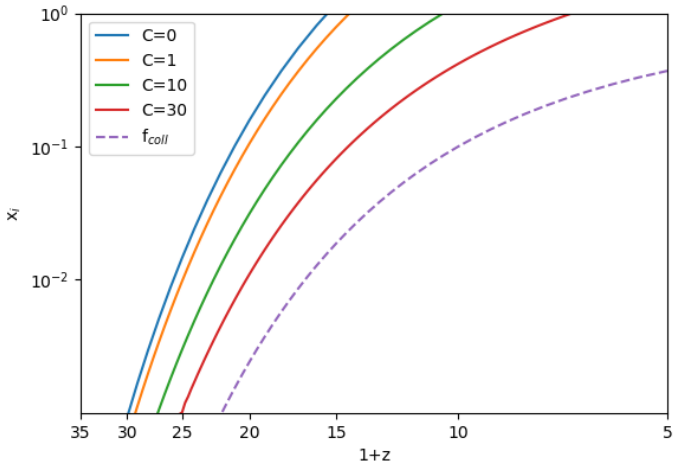

Figure 4: Ionized fraction vs z+1. Blue line considers C=0 (thus no recombinations). Orange C=1, green C=10, red C=30. The dashed line shows the collapse fraction f_{coll} evaluated for $m_{min} = m_4$.

regions where also recombinations are higher. The relative importance of these two effects must be evaluated and many works have attempted to do this (i.e. in Miralda-Escudé et al. (2000) it is considered that voids are ionized first [101]). Finally, it must be considered that reionization itself changes the evolution of gas clumps, having an impact on C(z) [5]. When the gas becomes ionized, thermal pressure increases and clumps evaporate. This process is quite complicated to quantify and in principle should require simulations of coupled-gas dynamics and radiative transfer. Due to the complexity of solving these three problems, throughout this work C will be mostly taken as a constant. If not, the following fit from simulations that is able to solve the first problem mentioned above (but not the second and third one) will be used [88] [98]:

$$C(z) = 27.466 \exp(-0.114z + 0.001328z^2) \tag{53}$$

Having discussed all the factors present in Eq. (52) we are now in the position to discuss some results. Figure 4 shows the evolution of the ionized fraction (x_i which is the same of Q_{HII}) as a function of redshift (z+1) for different clumping factors (from left to the right we have C=0,1,10,30). Ionizations are accounted taking an efficiency $\zeta = 20$ ($f_{esc} = 0.1$, $f_\star = 0.1$, $N_{ion} = 4000$) and f_{coll} is evaluated taking $m_{min} = m_4$. Such parameters are typical of Pop.II stars with a Scalo IMF [124]. Cosmological parameters are identical to the ones adopted in the previous plots. When the clumping factor is higher (thus there are more recombinations), the ionized fraction is lower and complete reionization ($x_i = 1$) is reached at a lower redshift.

1.3.3 Thomson scattering optical depth

To conclude this discussion about reionization it is interesting to mention a useful observable that can put some constraints on the redshift at which reionization is completed: the Thomson scattering optical depth (τ_e). Reionization affects the CMB because Thomson scattering of CMB photons with electrons washes out temperature fluctuations and generate large-scale polarization anisotropies [53]. The higher is the redshift at which reionization is completed, the larger is τ_e. From WMAP [142] and Planck collaboration [110] [111], large-scale correlation between temperature and polarization maps is measured and from this values of Thomson scattering optical depth can be inferred; the latest measure (Planck 2018) [111], gives $\tau_e = 0.0561 \pm 0.0071$. For a given reionization history (computed as described above), τ_e can be simply estimated as follows [132]:

$$\tau_e(z) = \int_0^z dz' \left| c\frac{dt}{dz'} \right| \sigma_T n_e(z') \tag{54}$$

where $\sigma_T = 6.65 \times 10^{-25} cm^2$ is the Thomson cross section and $n_e(z)$ the number density of free electrons at a given redshift and it can be evaluated as $n_e = Q_{HII}(z) n_B^0 (1+z)^3$ [132]. So, once a certain reionization history is computed, its Thomson scattering optical depth can be evaluated and compared with the values measured from CMB observations, providing thus a useful test to check the consistency of the computed reionization history. In figure 5 it is shown a reionization history and τ_e predicted compared with different measures from WMAP and Planck. To compute this evolution of Q_{HII} the collapse fraction has been evaluated adopting $m_{min} = m_4$, an efficiency $\zeta = 20$ (typical of Pop.II stars) and the clumping factor C taken from Eq. (53) discussed in Section 1.3.2. In this scenario, $Q_{HII} = 1$ at z$\sim$6, providing a $\tau_e = 0.0629$ which lies just below the upper limit of measurements from Planck 2018.

1.4 Feedback processes

Once first stars are formed, they will influence the IGM evolution through various "feedback" effects, some of which (e.g. photodissociation) have been already mentioned. The word "feedback" usually stands for a back reaction of a process on itself or on the causes that have produced it; thus, a feedback process can be positive if this back reaction enhances the process itself, or oppositely, negative. This idea of feedback is linked to the possibility that a system can become self-regulated [26]. In this subsection, the main feedback effects will be reviewed, in order to understand how it is possible to track the evolution of the IGM after the formation of the first luminous sources, for this reason, a major focus will be put into those processes that are important at high redshifts. Following the classification adopted by Ciardi & Ferrara (2005) [26], feedback processes can be: radiative, mechanical or chemical.

1.4.1 Radiative feedback

Radiative feedback indicates the processes related to radiation emitted by the first sources (stars and accreting BHs). Photons are able to change the IGM evolution depending on

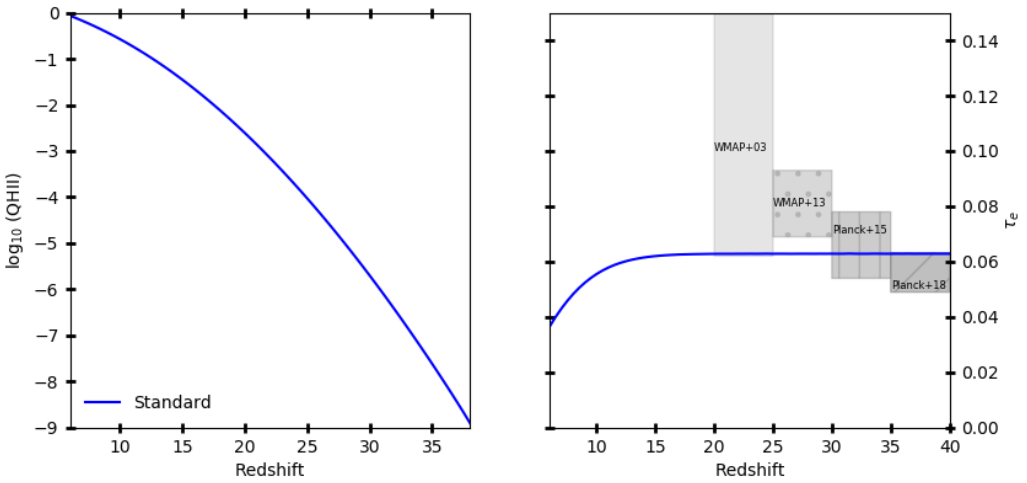

Figure 5: (left) log10 of filling factor (Q_{HII}) vs redshift (z). The filling factor monotonically increases, with z decreasing, until complete reionization ($Q_{HII} = 1$) is achieved at z=6. (right) τ_e vs redshift. Grey boxes indicate values of τ_e measured by observations (references are written inside boxes). These are put at different z just for a better visualization.

their energy, in particular, UV photons in general are able to suppress or delay star formation through a number of processes like:

- **Photoionization/photoevaporation**: UV photons produced by first stars can stop or slow down the formation of new objects. As we have already seen, UV photons drive cosmic reionization, decreasing the amount of neutral hydrogen and making the cooling less efficient. Together with the ionization, UV radiation heats up the gas (especially inside small objects where cooling is inefficient), and if the gas reaches temperatures higher than the virial temperature of the host halo, it can be boiled out of the gravitational potential well of the halo. This latter mechanism is referred to as photoevaporation and it can be responsible for the suppression of star formation inside minihalos. Photoevaporation could also provide a solution for the *Missing Satellite Problem* [20] without invoking alternative cosmological models to the classical ΛCDM one. It is difficult to disentagle between the effect of photoionization and photoevaporation since they are produced by the same field and are both an example of negative feedback [148].

- **H_2 Photodissociation**: This negative feedback effect due to photons in the Lyman-Werner bands has been already discussed at the end of section 1.2. The strength of this phenomenum is highly debated. From one side it has been shown that if the molecular cloud has a low metallicity ($\leq 10^{-2.5} Z_\odot$) a single O star can completely destroy its molecular hydrogen content so that subsequent star forma-

tion is almost quenched [106]. However, hydrodynamical simulations coupled to radiative transfer performed by Susa & Umemura (2006) [149], showed that under certain conditions of density and distance from a Pop.III star, a star forming cloud can survive thanks to the H_2 shell formed in front of the ionization front. According to Machacek, Bryan & Abel (2001) [90], the fraction of gas available for star formation in Pop.III objects of mass M exposed to a Lyman-Werner flux with intensity J_{LW} is $\sim$0.06ln(M/M_{th}) with M_{th} a mass threshold given by:

$$\frac{M_{th}}{M_\odot} = 1.25 \times 10^5 + 8.7 \times 10^5 \left(\frac{J_{LW}}{10^{-21} erg^{-1} cm^{-2} Hz^{-1}} \right) \tag{55}$$

In general this negative feedback effect can be counterbalanced by the positive feedback of H_2 re-formation, the strength of these two competing effects is still the subject of many studies ([2] [117] [120] [147] [150] [170]). Also an X-ray flux can enhance the H_2 fraction, however this positive effect is not enough to counterbalance the photodissociation [65].

- **Photoheating filtering**: the heating associated with photoionization causes the suppression of the formation of low-mass galaxies, so, as already stressed, cosmic reionization has a strong impact on galaxy formation. But we can expect that also reionization itself should depend on the reionization history [59]. From a practical point of view, it is needed a "filtering scale" k_F over which baryonic perturbations are smoothed as compared to the dark matter so that: $\delta_b = \delta_{dm} e^{-k^2/K_F}$. This filtering scale substitutes the Jeans scale and in terms of mass these 2 quantities are related as follows:

$$M_F^{2/3} = \frac{3}{a} \int_0^a da' M_J^{2/3}(a') \left[1 - \left(\frac{a'}{a} \right)^{1/2} \right] \tag{56}$$

This Filtering mass provides a better estimation of the critical mass for galaxy formation as it accounts for the thermal history of the gas, but it should not be taken as a precise value because there can be some effects (e.g. clustering of the sources) that can increase the suppression of minihalos formation [26].

In conclusion, even if all these effects delay star formation it is extremely difficult to assess precisely at which mass scale these processes act. To better appreciate this discrepancy, Fig. 6 shows various predictions on the mass of halos affected by radiative feedback (references in the figure).

1.4.2 Mechanical feedback

Mechanical feedback is related to the mass and energy deposition from first stars and black holes; the main examples are:

- **Blowout/Blowaway**: SN events might induce partial (blowout) or total (blowaway) gas removal from galaxy itself [26]. Blowaway occurs only in objects with

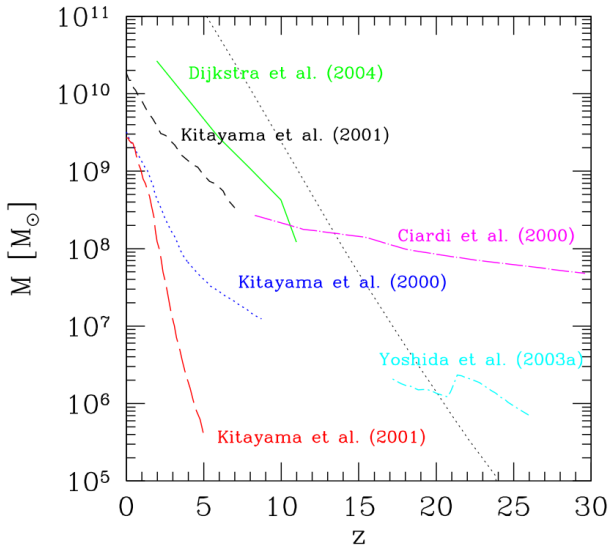

Figure 6: Taken form Ciardi et al. (2005). Mass of halos affected by radiative feedback as a function of redshift under different formulations. For details refers to the papers cited in the plot

M$\leq 5 \times 10^6 M_\odot$ (this limit has been confirmed by 3-D hydrodynamical simulations [103]). This low value is due to the fact that less than 30% of SN energy is converted into kinetic energy of the escaping gas while the remain is radiated away. Moreover, the mechanical feedback is less efficient than expected because SN explosions cause inward shocks that tend to collect gas in central regions of the halo. Again, details on the strength of this feedback are determined by the physical conditions of the medium surrounding the stars and by the stellar mass. SNe explosions, under certain conditions, can favour star formation since H_2 formation is enhanced by gas cooling behind the shocks. Moreover, since the interstellar gas is swept up, there is a formation of a dense shell behind the radiative shock; under appropriate conditions the shell becomes unstable and its fragmentation will trigger star formation [121].

- **Impinging Shocks**: SNe events can influence not only their host galaxy, but also neighbour galaxies, in particular shocks are able to increase the temperature of the IGM. If the gas in a forming galaxy is heated up to a temperature higher than its T_{vir} we can have mechanical evaporation of the gas leading to a complete suppression of star formation (this mechanism is identical to the photoevaporation already discussed). In order to prevent mechanical evaporation, the cooling time of the gas has to be shorter than its sound crossing time so that the gas cools before expanding out of the gravitational potential well and so continues to collapse [26]. If this is the case (as it often is) gas may be stripped from a collapsing perturbation by a shock from a nearby source as the momentum of the shock is sufficient to carry

the gas with it stopping galaxy formation. The scenario just described is typical of the dwarf galaxies with $M \leq 10^9 M_\odot$.

1.4.3 Chemical feedback

According to most scenarios, first stars formed out of primordial gas are very massive (few tens to few hundreds of $M_\odot$) and the ashes of these first SNe explosions should strongly pollute the gas with metals leading to the formation of Pop.II stars (non-zero metals). This transition from metal-free stars to Pop.II stars is accompained with a transition also on the Initial Mass Function (IMF) (from a top-heavy mass function to a Salpeter-like); the critical metallicity at which this transition occurs has been found to be $Z_{cr} = 10^{-5\pm1} Z_\odot$ [130] [131]. The uncertainties are due to the role of dust because dust cooling can induce fragmentation down to sub-solar masses at low metallicities ($\sim 10^{-6} Z_\odot$) otherwise we can have stars of $100 M_\odot$ even at 0.01 $Z_\odot$. Chemical feedback thus, is responsible for a change in chemical composition and IMF of stars and its strength will depend on the number of Pop.III stars that explode (as core-collapse or pair instability supernovae) and on the efficiency of metal ejection. Assessing the importance of chemical feedback is crucial in order to understand whether the role of Pop.III stars was negligible (strong chemical feedback) or not (weak chemical feedback). It seems reasonable to think that Pop.III/Pop.II transition could not be instantaneous as the metal content was not constant across the Universe so that Pop.II and Pop.III stars could actually be coeval. For this reason, the use of the critical metallicity defined above must be adopted only as a local criterion. Many numerical and analytical works ([125] [152] [79] [169] [122] [123]) shows that Pop.III stars continue to contribute to the total Star Formation Rate density at moderate redshifts ($\sim 13 - 18$)

2 The 21cm line as a tracer of the Cosmic Dawn

While the theoretical framework described in Chapter 1 has been well established, many quantities related to the physics of first stars and reionization are still affected by large uncertainties due to the very few observations that we have collected so far. Many difficulties that we encounter when we try to observe the Universe at Cosmic Dawn can be overcome using the 21 centimeter line of HI. This hyperfine transition, is originated by the coupling between the spins of the proton and electron, whose relative directions affect the energy of the electron orbit. So, when the electron flips its spin moving from a state in which the two spins are parallel (higher energy) to a state in which they are anti-parallel (lower energy), we end up with an emission of a photon with $\lambda = 21$ cm (or $\nu = 1420$ MHz). Being a spectral line, this 21cm transition is affected by cosmological redshift, and - at the epoch of our interest - the line is expected to be observed at 30-200 MHz. Using this line as a tracer of Cosmic Dawn allows us to directly probe the IGM since, until reionization is completed, it is constituted mainly by neutral hydrogen. Finally, as it will be discussed below, the transition energy is low enough ($\Delta E = 5.9 \times 10^{-6} eV$) to be a sensitive thermometer of the low-temperature IGM and, as a low-frequency radio transition, it can be seen across the entire IGM against the CMB during the entire epoch of reionization [53] [88]. Before moving to the physical processes that regulate this transition, it is worth to mention that this line, firstly observed in 1951 by Ewen & Purcell [44], has been already widely used in astrophysics to trace the spiral structure of the Milky Way and to measure many rotation curves of spiral galaxies (e.g. M31 [162]).

2.1 Physics of 21cm

To evaluate the strength of the 21cm transition coming from a hydrogen cloud across a certain line of sight, we need to solve the radiative transfer equation for the specific intensity I_ν (intensity per unit frequency) along a path described by coordinate s:

$$\frac{dI_\nu}{ds} = -\alpha_\nu I_\nu + j_\nu \tag{57}$$

where α_ν and j_ν represent the gas absorption and emission terms. In this framework we are considering an external source located on the opposite side to the observer with respect to the HI cloud. This equation can be rewritten for the 21cm transition in terms of the Einstein coefficients (which determines the transition probability) assuming statistical equilibrium for a 2-level atom [164]:

$$\frac{dI_\nu}{ds} = \frac{\phi(\nu) h\nu}{4\pi}[n_1 A_{10} - (n_0 B_{01} - n_1 B_{10}) I_\nu] \tag{58}$$

with $\phi(\nu)$ the line profile function normalized by $\int \phi(\nu) d\nu = 1$ [88]. Here we are denoting with subscript 0 the less energetic hyperfine state in which the spin of the proton and electron are antiparallel (1S singlet) and with 1 the most energetic one in which the two spins are parallel (1s triplet). A_{10}, B_{10} and B_{01} are the Einstein coefficients for spontaneous emission, stimulated emission and stimulated absorption respectively. These

coefficients are linked to each other through standard relations in atomic physics and their values are fixed for each atomic transition considered (e.g. $A_{10} = 2.85 \times 10^{-15}\mathrm{s}^{-1}$ for the 21cm transition, it is very low as expected for forbidden transitions). To better appreciate the link between Eq. (57) and Eq. (58) here is provided the expression for the absorption coefficient α_ν in terms of the Einstein coefficients [164]:

$$\alpha_\nu = \Phi(\nu)\frac{h\nu}{4\pi}(n_0 B_{01} - n_1 B_{10}) \tag{59}$$

Another key quantity in order to solve the radiative transfer equation is the spin temperature of the hydrogen cloud T_S. It is nothing else than the excitation temperature for the 21cm transition, thus, its definition arises from Boltzmann equation for the relative populations of hydrogen atoms in the two spin states: $n_1/n_0 = g_1/g_0 \exp^{-T_\star/T_S}$ where $T_\star = E_{10}/k_B = hc/\lambda_{21cm}k_B = 68mK$ is the temperature equivalent to the transition energy E_{10} and $g_1/g_0 = 3$ is the ratio of the spin degeneracy factors of the two levels. So, T_S regulates the amount of hydrogen atoms in the two different hyperfine levels. As we will see below, in the regime of our interest $T_\star << T_S$ making $n_1 \simeq 3n_0$ and the total number density hydrogen $n_H = 4n_0$. Since we are considering a radio transition, we can use the Rayleigh-Jeans approximation that allows us to express the specific intensity in terms of the brightness temperature $T_b(\nu)$: $I_\nu = 2k_B T_b \nu^2/c^2$ where c is the speed of light and k_B the Boltzmann constant. We remind that the brightness temperature T_b is the temperature required for a blackbody radiator with spectrum B_ν (in our case the Planck function in the Rayleigh-Jeans approximation) such that $I_\nu = B_\nu(T_b)$. Since we are in a cosmological context, we need to consider the expansion of the Universe, thus, the emergent brightness $T'_b(\nu_0)$ measured in a cloud's comoving frame at redshift z, creates an apparent brightness at Earth of $T_b(\nu) = T'_b(\nu_0)/(1+z)$ with the observed frequency $\nu = \nu_0/(1+z)$ [53] [50]. Quantities denoted with the prime are referred to the emitting cloud, while we will work with the observed quantities just defined. Since we are considering the presence of an external source behind the atomic hydrogen cloud we will have a brightness T_R also for the background radiation field incident on the cloud. With the same argument that led to the definition of T'_b we can define T'_R as the observed brightness temperature of the background. A final definition that allows us to rewrite the radiative transfer equation in a simpler way is the optical depth $\tau_\nu \equiv \int ds \alpha_\nu$ (the integral of the absorption coefficient along the ray through the cloud). Starting from Eq. (59) for the absorption coefficient α_ν, substituting n_1/n_0 with the expression given by Boltzmann equation and using relations between Einstein coefficients ($B_{10} = (g_0/g_1)B_{01} = A_{10}(c^2/2h\nu^3)$) the optical depth becomes:

$$\tau_\nu = \int ds \frac{3c^2 A_{10}}{8\pi\nu}(1 - e^{-E_{10}/k_B T_S})\phi(\nu) n_0 \tag{60}$$

With all the quantities defined so far it is possible to rewrite the initial expression for the radiative transfer (Eq. 57) in the Rayleigh-Jeans approximation (thus in terms of the brightness temperature instead of the specific intensity):

$$T'_b(\nu) = T_S(1 - e^{-\tau_\nu}) + T'_R(\nu)e^{-\tau_\nu} \tag{61}$$

The strength of the 21cm signal coming from an hydrogen cloud is estimated starting from the solution of this latter equation where all the terms have been defined throughout this section. To find a solution for Eq. (61), we begin by rewriting Eq. (60) for the optical depth assuming uniformity throughout the cloud and remembering that 1/4 of total hydrogen atoms are in the hyperfine singlet state (so we are assuming again that $T_\star << T_S$):

$$\tau_\nu \simeq \frac{3c^2 A_{10}}{8\pi\nu^2}\left(\frac{h\nu}{k_B T_S}\right)\left(\frac{N_{HI}}{4}\right)\phi(\nu) \tag{62}$$

where N_{HI} is the column density of HI. The line profile $\phi(\nu)$ is mainly determined by the expansion of the Universe (natural, thermal and pressure broadening are negligible in our case) and it can be simply evaluated as $\phi(\nu) \sim 1/\Delta\nu \sim c/\nu\Delta v$ with Δv the velocity broadening. For a linear dimension s $\Delta v \sim sH(z)$ so that $\phi(\nu) \sim \frac{c}{sH(z)\nu}$. The column density N_{HI} along such a segment s is simply $N_{HI} = x_{HI} n_H(z) s$ [53]; now, starting from Eq. (62) we have all the elements to write a more exact expression of τ_ν (we just need to substitute to $\phi(\nu)$ and to N_{HI} in Eq. (62) the two expressions just found) [88]:

$$\tau_\nu = \frac{3}{32\pi}\frac{hc^3 A_{10}}{k_B T_S \nu_0^2}\frac{x_{HI} n_H}{(1+z)(dv_{||}/dr_{||})} \tag{63}$$

$$\simeq 0.0092(1+\delta)(1+z)^{3/2}\frac{x_{HI}}{T_S}\left[\frac{H(z)/(1+z)}{dv_{||}/dr_{||}}\right] \tag{64}$$

where $dv_{||}/dr_{||}$ is the velocity gradient along the line of sight and δ is the fractional overdensity of baryons. These factors appear because in this final expression we have scaled the IGM density at z and the velocity gradient (the Hubble flow) to their mean values (so $n_H = \bar{n}_H(1+\delta)$).
Having the expression for the optical depth, we are now in the position to compute the differential brightness temperature (DBT) which represents the contrast between the brightness temperature of the high-z hydrogen clouds and a background source: $\delta T_b = T_b - T_R$. Substituting the optical depth computed in Eq. (64) inside Eq. (61) where we consider the observed quantities (so dividing by a factor 1+z) we obtain [53]:

$$\delta T_b(\nu) = \frac{T_S - T_R}{1+z}(1 - e^{-\tau_\nu}) \simeq \frac{T_S - T_R}{1+z}\tau_\nu \tag{65}$$

$$\simeq 9 x_{HI}(1+\delta)(1+z)^{1/2}\left[1 - \frac{T_R}{T_S}\right]\left[\frac{H(z)/(1+z)}{dv_{||}/dr_{||}}\right] mK \tag{66}$$

The approximation in Eq. (65) can be done because at redshifts of our interest, the optical depth is small so we can do a first order expansion. Eq. (66) is the one that allows to estimate the strength of the 21cm signal from an HI emitting cloud in contrast with a background source (T_R). There are two relevant backgrounds that we can consider: the CMB or a radio loud point source. In the first case $T_R = T_\gamma$ that can be easily computed at each redshift since we know that CMB temperature decreases with redshift as 1+z and that the present temperature is well established to be 2.728K so $T_\gamma(z) = 2.728(1+z)K$. The 21cm signal is seen as a spectral distortion to the CMB blackbody spectrum and such

distortion form a diffuse background that can be studied across the whole sky in a similar way to CMB anisotropies (but 21cm distortion is much larger than CMB anisotropies which are really small: $\delta T_\gamma \sim 10^{-5}$) [115]. The signal will be seen in absorption when $T_S < T_\gamma$, otherwise it will be seen in emission; as we will discuss later, both regimes are important for the high-z Universe. In the second situation (an example of a radio loud point source could be a quasar) the background will be much stronger than the emitting cloud ($T_R >> T_S$), so we will expect to see the signal always in absorption against the source. Considering different radio loud sources located at different distances (so at different redshifts), we will expect to observe a "forest" of line commonly referred to as "21cm forest" (the mechanism is the same as the one that leads to the Lyα forest) [115]. Throughout this work we will focus only on the first case as we are mainly interested in obtaining information about the global physical properties of the IGM during Cosmic Dawn, in order to be able to infer the properties of the first stars and the first black holes.

2.1.1 The spin temperature

Our starting point is Eq. (66) where $T_R = T_\gamma$. Other than cosmological parameters, there are two key dependences: the neutral hydrogen fraction x_{HI} and the spin temperature of the IGM T_S. As a first approximation $x_{HI} = 1 - \bar{x}_i$ where $\bar{x}_i$ is the global ionized fraction (we are assuming that the IGM is made only by hydrogen), so the amount of neutral hydrogen is determined by the ionization history of our Universe. We already seen how it is possible to compute it in section 1.3, so the main quantity which is left to discuss is T_S; here we will focus on all the relevant processes that can alter the spin temperature. These are mainly three: *(i)* absorption/emission of 21cm photons from the CMB background, *(ii)* collisions with other species (mainly other hydrogen atoms and free electrons), *(iii)* scattering of UV photon via an effect known as *Wouthuysen-Field effect* [115]. If only the CMB was present $T_S = T_\gamma$. However, the presence of other particles, changes the evolution of T_S through the other two effects. The timescales of these processes are much shorter than the expansion time at all redshifts after cosmological recombination, so the value of T_S is set by an equilibrium condition. Taking C_{10} and P_{10} as the de-excitation rates per atom due to collisions and UV scattering respectively and C_{01} and P_{01} the corresponding excitation rates, the equilibrium condition can be written as [88]:

$$n_1(C_{10} + P_{10} + A_{10} + B_{10}I_{CMB}) = n_0(C_{01} + P_{01} + B_{01}I_{CMB}) \tag{67}$$

where I_{CMB} is the specific intensity of CMB photons. Using Rayleigh-Jeans approximation (that allows us to write $I_{CMB} = \frac{T_\gamma c^2}{2k_B\nu^2}$), the relation between the Einstein coefficients $B_{10} = A_{10}(c^2/2h\nu^3)$, the principle of detailed balance $\frac{C_{01}}{C_{10}} = \frac{g_1}{g_0}e^{-T_\star/T_K} \simeq 3(1-\frac{T_\star}{T_K})$ where T_K is the kinetic temperature and defining the effective color temperature for the UV radiation field T_c using $\frac{P_{01}}{P_{10}} \equiv 3(1 - \frac{T_\star}{T_c})$ Eq. (67) becomes:

$$T_S^{-1} = \frac{T_\gamma^{-1} + x_c T_K^{-1} + x_\alpha T_c^{-1}}{1 + x_c + x_\alpha} \tag{68}$$

with $x_c = C_{10}T_\star/A_{10}T_\gamma$ and $x_\alpha = P_{01}T_\star/A_{10}T_\gamma$ the coupling coefficients for collisions and UV scattering. As it will be discussed below, T_c is strongly coupled to T_K by recoil scattering, so, the coupling coefficients determine at which temperature T_S will be coupled: if $x_{tot} = x_\alpha + x_c >> 1$ then $T_S \to T_K$, in the opposite regime ($x_{tot} \simeq 0$), $T_S \to T_\gamma$ [115]. Now we are going to discuss each of these key factors for T_S evolution: x_α, x_c and T_c.
Firstly, we consider collisional excitation and de-excitation between the hyperfine level of atomic hydrogen, these are particularly important in dense gas. Considering a collision of an H atom with a species i, the following expression for x_c^i has been found by Field (1958) [48]:

$$x_c^i \equiv \frac{C_{10}^i}{A_{10}}\frac{T_\star}{T_\gamma} = \frac{n_i k_{10}^i}{A_{10}}\frac{T_\star}{T_\gamma} \tag{69}$$

where k_{10}^i (units of $cm^3 s^{-1}$) is the rate coefficient for spin de-excitation by collisions with species i. The total x_c in Eq. (68) is given by the sum over all species i that may collide with atomic hydrogen, in particular we need to consider: other hydrogen atoms, free electrons and protons (in principle we could consider also other atomic species like helium and deuterium but these turn out to be unimportant [88] [53]. For this reason the total coupling coefficient can be expressed as:

$$x_c = x_c^{HH} + x_c^{eH} + x_c^{pH} = \frac{T_\star}{A_{10}T_\gamma}[k_{10}^{HH}(T_K)n_H + k_{10}^{eH}(T_K)n_e + k_{10}^{pH}n_p] \tag{70}$$

The various k-coefficients can be determined by the quantum mechanical cross sections of the relevant processes. For H-H collisions, this has been intensively computed in [4] and [173] where a full quantum-mechanical treatment is adopted starting from the energy conservation law. Detailed expressions for k_{10}^{eH} can be instead found in [55]; the approach is almost identical to the one used to derive the scattering rate between two hydrogen atoms, but in this case the problem is more complicated since here we have a three-body problem [53]. Collisions with protons are instead considered in [56]. The strength of each of these rates is shown in Fig. (7). There, we can appreciate the fact that, almost at all temperatures, the scattering between electron and hydrogen atoms dominate. However, collisional coupling coefficients depend also on the number density of the species considered. This makes the total x_c relevant only during the dark ages (at later times due to the adiabatic expansion of the Universe number densities of all species are very low), an epoch in which the IGM was mostly constituted by neutral hydrogen with very few electrons. For this reason, although k_{10}^{HH} is rather small compared to k_{10}^{eH}, collisions between hydrogen atoms dominate during dark ages. Collisions with protons are important only at very low temperatures [56].

As already stressed, the coupling between different atomic species, becomes quickly ineffective due to the drop in the number density of the various species so that $x_c \simeq 0$ when $z \leq 70$. However, once star formation begins, we have the production of Lyα photons, which are able to effectively couple T_S to T_K through resonant scattering via a process generally referred (from the name of the discoverers) as *Wouthuysen-Field effect* [167] [48]. This mechanism is illustrated in Fig. 8 where hyperfine sublevels of 1S and

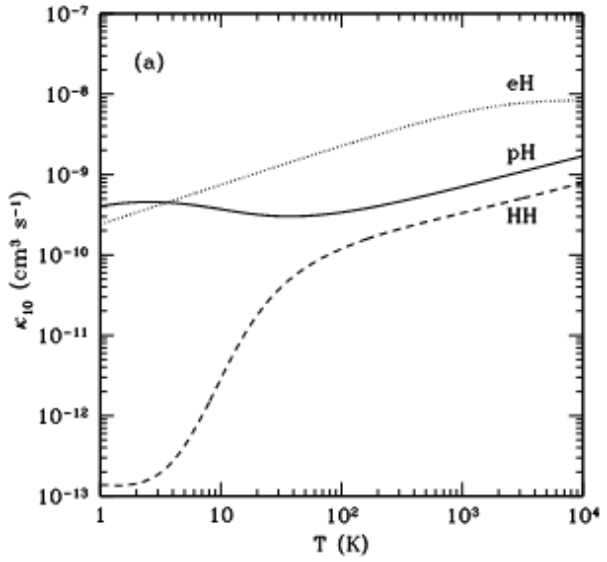

Figure 7: De-excitation rate coefficients for H-H collision (dashed), $H - e^-$ collisions (dotted) and $H - p^+$ collisions (solid). Figure taken from [56].

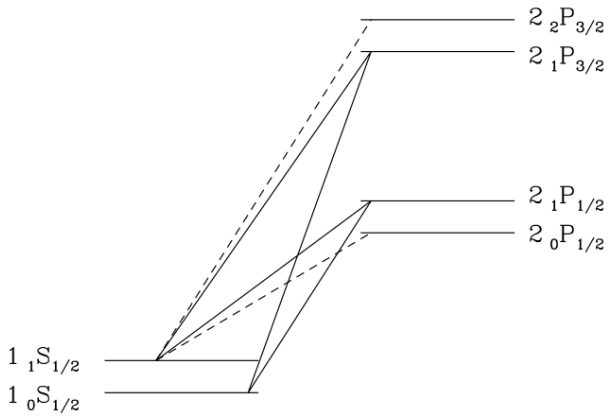

Figure 8: Hyperfine splitting of the 1S and 2P levels. The figure shows transitions that mix the ground-state hyperfine levels (solid) and complementary allowed transitions that do not participate in mixing (dashed). Figure taken from [114].

2P states are drawn. An hydrogen atom initially in the hyperfine singlet state, can be excited by a Lyα photon into either of the central 2P hyperfine states (remember that selection rules require ΔF=0,1 and F=0$\rightarrow$0 is not allowed). This state, can decay to the ${}_1S_{1/2}$ level thus, atoms can change their hyperfine level after the absorption and the consequent re-emission of a Lyman-α photon. In this simplified treatment (physics behind this mechanism is more subtle), we need to consider that the Wouthuysen-Field coupling must depend on the total rate per atom at which Lyα photons are scattered within the gas P_α that is given by [88]:

$$P_\alpha = 4\pi\sigma_0 \int d\nu J_\nu \Phi_\alpha(\nu) \tag{71}$$

where $\Phi_\alpha(\nu)$ is the Lyman-α absorption profile, J_ν is the angle-averaged specific intensity of the background radiation field, $\sigma_\nu \equiv \sigma_0\Phi_\alpha$ is the local absorption cross section and $\sigma_0 \equiv (\pi e^2/m_e c) f_\alpha$ (with $f_\alpha = 0.4162$ the oscillatory strength of the Lyman-α transition.) J_ν is expressed by number of photons and not by energy (photons $cm^{-2}s^{-1}sr^{-1}$), since the quantity by number is conserved during the expansion of the Universe while the energy redshifts away. The line typically has a Voigt profile that accounts for natural and thermal broadening and in the simplest approximation J_ν is considered constant across the line (we will soon see that this is not completely true). The coupling coefficient in terms of P_α can be written as [92]:

$$x_\alpha = \frac{4P_\alpha}{27A_{10}} \frac{T_\star}{T_\gamma} \tag{72}$$

This relation is derived in a similar way to that of the collisional coupling coefficients, where in this case $P_{01} = \frac{4P_\alpha}{27}$ (this relation results from the atomic physics of the hyperfine lines using the assumption of constant radiation field across them). Inserting Eq. (71) for P_α inside Eq. (72), we obtain the following:

$$x_\alpha = \frac{16\pi^2 T_\star e^2 f_\alpha}{27A_{10}T_\gamma m_e c} \int d\nu J_\nu \Phi_\alpha \tag{73}$$

In this expression for x_α we are not specifying any form for J_ν. A common approach is to assume $J_\nu = J_\alpha$ (where J_α is the specific flux at the Lyman-α frequency; this means we are taking J_ν constant across the line). Then we consider a correction factor $S_\alpha = \int dx \Phi_\alpha(x) J_\nu(x)/J_\infty$ (with J_∞ the flux far away from the absorption feature) that accounts for the fact that the flux is not constant as just assumed and describes the detailed structure of the photon distribution in the neighborhood of the Lyman-α resonance. With this adjustment we can write a useful expression for x_α [71]:

$$x_\alpha = \frac{16\pi^2 T_\star e^2 f_\alpha}{27A_{10}T_\gamma m_e c} S_\alpha J_\alpha \tag{74}$$

Collecting the various constants we can finally write:

$$x_\alpha = S_\alpha \frac{J_\alpha}{J_\nu^c} \tag{75}$$

with $J_\nu^c \equiv 1.165 \times 10^{-10}[(1+z)/20] cm^2 s^{-1} Hz^{-1} sr^{-1}$. So, in order to have a final expression for the Lyman-α coupling, the correction factor S_α is the only quantity left to evaluate. Since the Wouthuysen-Field effect couples T_S with the color temperature, together with S_α we need an expression also for T_c already defined at the beginning of this subsection.
T_c is determined by the shape of the photon spectrum near the Lyman-α resonance. This is easier to see if we take the definition of the effective color temperature that obeys to the detailed balance found in [92] (neglecting stimulated emission [118]). Under this assumption it is possible to rewrite the ratio between the excitation and de-excitation rate for UV scattering as [53]:

$$\frac{P_{01}}{P_{10}} \simeq 3(1 + \nu_0 \frac{d \ln n_\nu}{d\nu}) \tag{76}$$

where $n_\nu = c^2 J_\nu / 2\nu^2$ is the photon occupation number. Reminding that we defined the color temperature as $\frac{P_{01}}{P_{10}} \equiv 3(1 - \frac{T_\star}{T_c})$ and that $T_\star = h\nu/k_B$ we can rewrite the definition of T_c as:

$$\frac{h}{k_B T_c} = -\frac{d \ln n_\nu}{d\nu} \tag{77}$$

Typically the color temperature is very close to the kinetic temperature of the gas [53] as the optical depth to Lyman-α scattering is very large leading to a large number of scatterings that bring the radiation field in local equilibrium with the gas for frequencies near the line center [49] [115]. The optical depth to Lyman-α scattering is also known as "Gunn-Peterson optical depth" and it can be expressed as [64] [53]:

$$\tau_{GP} = \frac{\sigma_0 n_{HI}(z) c}{H(z) \nu_\alpha} \simeq 3 \times 10^5 \left(\frac{1+z}{7} \right)^{3/2} \tag{78}$$

The large number of scatterings of Lyman-α photons near the Ly-α resonance that brings $T_c \to T_K$ leads to a distinct feature in the distribution of photons [115]. This feature can be described in terms of the flow of photons in frequency. In the high-redshift Universe, photons are continuously losing energy due to the cosmic expansion but they also lose energy whenever they experience a Lyman-α scattering from a hydrogen atom due to the recoil of the atom. This second effect has been extensively studied by Rybicki (2006) where the following expression for the energy loss (or gain) by the photon per scattering is provided [118]:

$$\frac{\Delta E}{E} = \frac{h\nu}{m_p c^2} \left(1 - \frac{T_K}{T_c} \right) \tag{79}$$

The first factor comes from recoil off an isolated atom while the second corrects for the distribution of initial photon energies [53]. Another source of energy loss is the energy difference between hyperfine levels [28], however this is less important than atom recoil ($\leq 10\%$). The net effect of this loss of energy is to increase the flow to lower energies leading to a deficit of photons near the line center. This process ends up in an asymmetry about the line toward lower frequencies and the presence of such an asymmetry brings the

photon distribution into local thermal equilibrium with $T_c \simeq T_K$ (this can be appreciated also from Eq. (79) where, for $T_c \to T_K$, the recoil factor becomes null). The shape of this feature determines S_α. Since recoils source an absorption feature we reasonably expect $S_\alpha \leq 1$.
The mathematical derivation of S_α (which will not be shown here) is based on a Fokker-Planck approximation of the radiative transfer equation in an expanding universe [118] [71]. A useful approximation for S_α is [53]:

$$S_\alpha \sim \exp\left[-0.803 T_K^{-2/3} \left(\frac{10^6}{\gamma} \right)^{1/3} \right] \tag{80}$$

where $\gamma = \tau_{GP}^{-1}$. Finally, it is worth to emphasize the fact that we focused only on photons redshifting into Lyman-α from frequencies below the Lyman-β resonance. In principle, Lyman-α photons can be produced by atomic cascades from photons redshifting into higher Lyman series resonances [115] (neutral IGM at high-redshifts has so much hydrogen that any Lyman series photon will be soon absorbed). The probability of converting a Lyman-n photon into a Lyman-α photon is set by atomic rate coefficients (see [71] and [114]), for large n there is a conversion factor (often called "recycling factor" f_{rec}) of 30% [115]. When we consider Lyman-n photons, the Wouthuysen-Field coupling is different with respect to the Lyman-α case since now we are looking at photons which are injected into the Lyman-α line rather being redshifted from outside of the line. This difference can be better appreciated looking at figure 9 where the background radiation field near the Lyman-α resonance at z=10 is shown for both continuous photons and photons injected at line center [53].

2.2 The evolution of the IGM

Armed with Eqs. (69), (75) and (80) we are ready to compute the evolution of the spin temperature of the gas through Eq. (68). From these equations and by the fact that $T_c \simeq T_K$, it is evident that the evolution of T_S depends on the kinetic temperature of the gas and on the amount of Lyman-α photons in the Universe; both these quantities are determined by the presence of luminous sources that are able to heat up the gas and to produce Lyman-α photons.

2.2.1 The kinetic temperature evolution

The evolution of gas kinetic temperature is given by energy conservation in an expanding Universe [53] [22]:

$$\frac{dT_k}{dt} = -2H(t)T_K + \frac{2}{3}\sum_i \frac{\epsilon_i}{k_B n} \tag{81}$$

$$\frac{dT_k}{dz} = \frac{2T_K}{1+z} - \frac{2}{3}\sum_i \frac{\epsilon_i}{k_B n H(z)(1+z)} \tag{82}$$

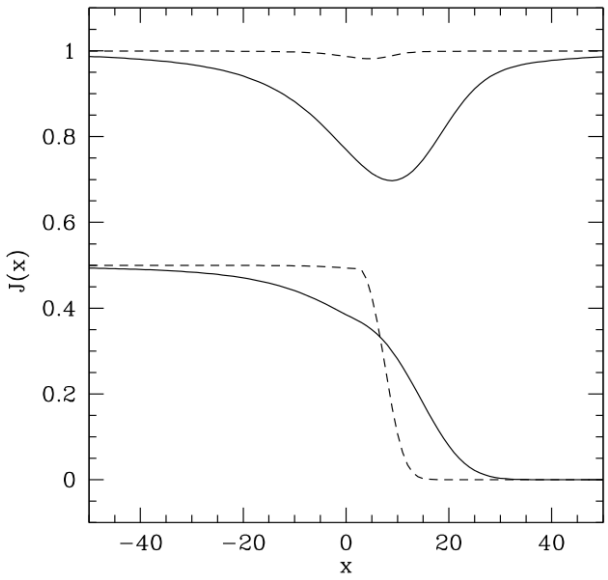

Figure 9: Background radiation field near the Lyman-α resonance at z=10, assuming a Voigt line profile. The upper and lower sets are for continuous photons and photons injected at line center, respectively. $T_K = 10K$ and $T_K = 1000K$ for solid and dashed line respectively. $x \equiv \frac{\nu - \nu_\alpha}{\Delta\nu_D}$ with $\Delta\nu_D$ is the frequency change per scattering. Taken from [114].

These two expressions are completely equivalent as we can easily move from cosmic time to redshift dependence using the relation $\frac{dt}{dz} = -\frac{1}{H(z)(1+z)}$. The first term considers the expansion of the Universe while in the second all the possible sources of heating or cooling i are accounted with ϵ_i (the heating rate per unit volume of process i). In order to compute T_K we just need to integrate one of the two above equations (depending on whether we are interested in the time or redshift evolution) specifying which energy source is present.
Before the formation of the first stars (or *Dark ages*), the only heating mechanism present is Compton scattering between CMB photons and free electrons in the IGM [133] [53] given by:

$$\frac{2}{3}\frac{\epsilon_{comp}}{k_B n} = \frac{\bar{x}_i}{1 + f_{He} + \bar{x}_i}\frac{T_\gamma - T_K}{t_\gamma} \tag{83}$$

with f_{He} the helium fraction by number, $t_\gamma \equiv \frac{3m_e c}{8\sigma_T u_\gamma}$ the Compton cooling time, σ_T the Thomson cross section and u_γ the photon energy density proportional to T_γ^4. Eq. (83) shows that for large values of u_γ typical of the very high-redshift Universe (before recombination), $T_K \to T_\gamma$ meaning that the gas will cool down at the same pace of CMB photons ($\propto (1+z)$). The main effect of this heating process is to couple T_K to T_γ for $z \geq 150$. At lower redshifts Compton heating becomes completely ineffective making the gas to cool adiabatically $T_K \propto (1+z)^2$. As we will see, we are mostly interested in the spin temperature (and so in the kinetic temperature) evolution at much lower redshifts; thus Compton heating will be used only to fix the initial condition on the time/redshift evolution of T_K.
Once first luminous sources appear, the IGM evolution becomes more complex and more uncertain. The first effective heating source that we can think of is X-rays from early galaxies and quasars [53]. The main challenge in modeling the impact of first sources, is that we need to correctly extrapolate relations that are usually inferred from low-redshift ($z \leq 6$) observations to high-redshifts. Concerning X-rays, the local correlation between the SFR and the X-ray luminosity from 2 to 10 keV is taken:

$$L_X = 3.4 \times 10^{40} f_X \frac{SFR}{1 M_\odot yr^{-1}} ergs^{-1} \tag{84}$$

This relation has been discovered by Grimm et al. (2003) [63], and it is based on Chandra and ASCA observations of nearby star-forming galaxies. In particular, the value of the constant correctly matches the proportionality between the X-ray luminosity of a galaxy arising from high-mass X-ray binaries (HMXBs) and the SFR for high values of SFR (which we reasonably expect at high redshifts when star formation just started). This scaling relation is reasonable even at high-z as massive X-ray binaries form when the first massive stars die, only a few million years after star formation commences and so they should also be present in high-redshift galaxies [54]. Nonetheless, our ignorance of the accuracy of this relation at high-redshifts (in particular for what concerns the proportionaliy constant) is parameterized through f_X. This parameter will likely evolve with redshift (e.g. at high-z we can have a top-heavy IMF that likely will increase f_X), but for simplicity we will take it as a constant. A similar assumption has been made by

Madau et al. (2017) [96] who also argued that the contribution of low-mass X-ray binaries (LMXBs) is negligible at high-z as the contribution of LMXBs starts to makes a significant contribution at $z \leq 1.5$. X-rays can heat up the gas thanks to electrons that they can produce with hydrogen or helium photoionization. Such electrons, will redistribute their energy through: *(i)* collisional ionizations (producing more electrons), *(ii)* collisional excitations of HeI and HI or *(iii)* Coulomb collisions with other free electrons. The relative cross sections of these processes determine the fraction of X-ray energy going to heating ($f_{X,h}$) and ionization ($f_{X,ion}$) [53]; we are interested in the first one. These factors have been evaluated by Shull & van Steenberg [139] using Monte Carlo computations in the high-energy limit ($E >> 0.1$keV). The fitting arising from their results is the following:

$$f_{X,h} = C_1[1 - (1 - x_e^{a_1})^{b_1}] \tag{85}$$

with $C_1 = 0.9971$, $a_1 = 0.2263$ and $b_1 = 1.3163$. Notice that x_e is the electron fraction in the neutral gas that must not be confused with ionized fraction (or filling factor) that changes throughout reionization. At the epoch of our interest, $x_e \simeq 10^{-3}$ making $f_{X,h} \simeq 0.2$ [54]. Another possible approach is to take $f_{X,h}$ as a free parameter and combine it with f_X already defined and let $f_{Xh} = f_X \times f_{X,h}$ change (this has been done by Chatterjee et al. (2019) [22]). The last step to relate the X-ray emissivty (ϵ_X) to the global SFR is to assume that SFR is proportional to the collapse fraction f_{coll} and to the star formation efficiency $f_\star$ in a similar way of what has been already done to compute the ionizing efficiency in Section 1.3.1. This leads to [53]:

$$\frac{2}{3}\frac{\epsilon_X}{k_B n H(z)} = 10^3 K f_X \left(\frac{f_\star}{0.1}\frac{f_{X,h}}{0.2}\frac{df_{coll}/dz}{0.01}\frac{1+z}{10}\right) \tag{86}$$

In this formula each quantity has been normalized to its typical value at $z \sim 9$ and accounts only for X-ray heating from stars (HMXRBs). So far we are not including the contribution of black hole accretion to the total X-ray background as it is not easy to compute it starting from analytical calculations. In Section 3 and beyond, once a semi-analytical code will be used, the accreting black hole contribution will be correctly accounted.

Throughout this work X-rays (either from stars or from black holes) will be the only source of heating considered. However, we could mention two additional heating sources: Lyman-α photons and shocks. Lyman-α photons, after they scatter with neutral hydrogen atoms, can deposit energy in the IGM through atomic recoil (we already discussed this mechanism in Section 2.1.1). The typical energy exchange per scattering is much smaller than the one provided by X-rays, this makes the Lyman-α heating effective only in presence of a large number of scatterings (very large Lyman-α flux is required and this is not the case at high redshifts). Moreover, in a static medium, the energy exchange must vanish in equilibrium even though there is a large number of scatterings. Chen & Miralda-Escudé (2004) and Rybicki (2006) showed that this equilibrium is actually reached quite soon, making this source of heating very ineffective and so negligible (especially if compared to the X-ray one) [24] [118] [54].

Also shocks could deposit energy into the IGM. This purely hydrodynamic mechanism

is linked to our modern view of structure formation. Shocks associated with large scale structure occur as gas separates from the Hubble flow and undergoes turnaround before collapsing onto a central overdensity [115]. At each stage of the collapse, some of the gravitational infall energy is transformed into thermal energy through shocks due to the differential accelerations forming a complex newtork of sheets and filaments which has been extensively tested by many cosmological simulations [81] [100]. It has been already assessed that shocks provide considerable heating at late times [21] [30], while there is no general consensus on their importance at early times. As a general condition, we can consider that shocks will form only if their post-shock temperature is larger than the gas kinetic temperature ($T_{sh} > T_K$). For a strong shock in a monoatomic gas the corresponding post-shock temperature is $T_{sh} \simeq \frac{3\mu m_p}{16 k_B} H^2(z) R_{nl}^2(z)$ with R_{nl} the non linear length scale [54]. At the present times $T_{sh} \sim 10^7$ K [21] making shocks important nowadays. However, T_{sh} decreases going back in time, and at moderate redshifts it is smaller than T_K [52]. At very high redshifts (i.e. before reionization), T_K is quite small making shocks non-negligible at those times. One of the most recent works by Ma et al. (2021) based on cosmological simulations coupled with a 3D radiative transfer code [89] [37] [62], found that shock heated ISM during reionization is very efficient at uniformly heating the IGM; this is supported also by some analytical works [52]. However, other simulations suggest that shocks do not strongly modifies the shape of the 21cm signal; in particular if we consider the impact of minihalos where star formation (and so X-ray heating) begins earlier [84]. This motivates our choice to completely neglect shocks throughout this work (in this sense we are consistent with many recent semi-analytical works [3] [29] [22]).

2.2.2 The Lyman-α background

Once T_K is known, only the Lyman-α coupling x_α is left to evaluate. Looking at Eq. (75), since J_ν^c is a known constant, and we already obtained an expression for S_α (see Eq. (80)), it is necessary to compute the evolution of the Lyman-α flux J_α (we focus on the Wouthuysen-Field coupling since, as we already stated, the collisional coupling is not important at the epochs of our interest). This flux is mainly produced by (young) stars, photons emitted between Lyman-α (10.2 eV) and the Lyman limit (13.6 eV), will redshift until they enter a Lyman series resonance. Subsequently, they may generate Lyman-α photons via atomic cascades [71] [114]. Considering this, we can write the average Lyman-α background (in units of $\mathrm{cm^{-2} s^{-1} Hz^{-1} sr^{-1}}$) as [54] [6]:

$$J_\alpha(z) = \sum_{n=2}^{n_{max}} J_\alpha^{(n)}(z) = \sum_{n=2}^{n_{max}} f_{rec}(n) \int_z^{z'_n} dz' \frac{(1+z)^2}{4\pi} \frac{c}{H(z')} \epsilon(\nu'_n, z') \tag{87}$$

where ν'_n is the frequency at redshift z' that redshifts into that resonance at redshift z:

$$\nu'_n = \nu_n \frac{1+z'}{1+z} \tag{88}$$

and:

$$\frac{1+z'_n}{1+z} = \frac{1-(n+1)^{-2}}{1-n^{-2}} \tag{89}$$

is the largest redshift from which a photon can redshift into it. The recycling factor is the one already introduced at the end of Section 2.1.1 and slightly changes depending on the stellar population considered (in [54] is taken f_{rec}=0.63 and f_{rec}=0.72 for Pop.III and Pop.II stars respectively.) Finally, the comoving photon emissivity (defined as the number of photons emitted per unit comoving volume, per proper time and frequency, at restframe frequency at redshift z) is given by [6]:

$$\epsilon(\nu, z) = f_\star \bar{n}_b^0 \epsilon_b(\nu) \frac{df_{coll}}{dt} \tag{90}$$

Here $\bar{n}_b^0$ is the comoving number density of baryons (that can be computed from cosmological parameters) and $\epsilon_b(\nu)$ is the spectral distribution function of the sources (the number of photons produced in the frequency interval $\nu \pm d\nu/2$ per baryon incorporated into stars). Firstly, $\epsilon_b(\nu)$ depends on the sources of radiation considered. If stars dominate over mini-quasars (reflecting the choice of Wyithe & Loeb (2004b) [168]) the dependence shifts on the IMF and metallicity considered. Since real spectra are quite complicated, we can introduce the total number of photons per baryon between Lyman-α and Lyman-limit N_α [53]. Using Leitherer et al. (1999) [87] and Bromm et al. (2001) [16] we can take $N_\alpha = 9690$ for Pop.II stars and $N_\alpha = 4800$ for Pop.III stars. With this approximation Eq. (87) becomes:

$$J_\alpha \simeq \frac{c}{4\pi} \bar{f}_{rec} f_\star \bar{n}_b^0 \delta f_{coll} \frac{N_\alpha}{\Delta\nu} (1+z)^2 \tag{91}$$

where $\Delta f_{coll} \sim f_{coll}$ is the spectrum-weighted collapse fraction over the appropriate redshift intervals [53].
Now we have all the ingredients to compute the kinetic and the spin temperature evolution. The following plots are obtained using the formalism already discussed (T_K is given by Eqs. (82) and (86), T_S by Eqs. (68), (75) and (91) and S_α is evaluated using the approximation in Hirata (2006) [71].) This takes:

$$S_\alpha = (1 - 0.0631789 T_k^{-1} + 0.115995 T_K^{-2} - 0.401403 T_s^{-1} T_k^{-1} + 0.336463 T_s^{-1} T_k^{-2}) \times \tag{92}$$

$$(1 + 2.98394\Psi + 1.53583\Psi^2 + 3.85289\Psi^3)^{-1} \tag{93}$$

$$T_c^{-1} = T_K^{-1} + 0.405535 T_k^{-1} (T_s^{-1} - T_k^{-1}) \tag{94}$$

where:

$$\Psi = (10^{-7} \tau_{GP})^{1/3} T_K^{-2/3} \tag{95}$$

T_K and T_S are both expressed in Kelvin. Since S_α and T_c are functions of T_s as well as T_k and τ_{GP} so a simple and robust way to find T_S for given T_γ, T_k, J_α, and the Gunn-Peterson optical depth is to iteratively compute T_c and S_α for some value of T_S, and then update T_S using Eq. (68). This iteration is initialized with $T_S = T_\gamma$. Results are shown in Figs. (10) and (11); these are obtained using the same formalism of Furlanetto (2006) [54] taking the cosmological parameters at the end of Section 1.1.2. Fig. 10 is obtained considering Pop.II star formation inside atomic cooling halos ($m_{min} = m_4$, $f_\star = 0.1$, N_α=9690 and $f_{rec} = 0.72$). Solid thin and thick curves shows T_K and T_S evolution

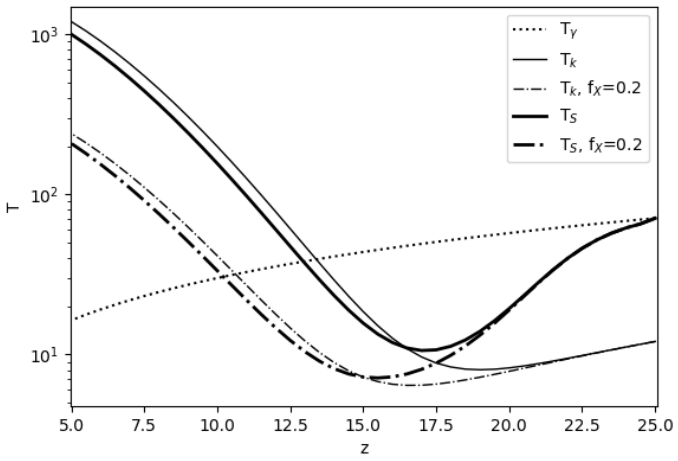

Figure 10: Redshift evolution of the spin temperature (thick lines) and of the kinetic temperature (thin lines) predicted by the analytic model when only Pop II stars are assumed to form (see text). Solid lines assume $f_X = 1$ while dot-dashed lines $f_X = 0.2$. Dotted line shows the evolution of CMB temperature ($\propto (1+z)$).

respectively where $f_X = 1$ and $f_{X,h}$ is evaluated through Eq. (85) using $x_e = 10^{-3}$. X-ray heating starts to be effective from $z \sim 21$ and at $z \simeq 19$ the IGM starts to heats up. Spin temperature decouples for CMB temperature already a $z \sim 25$ and couples almost perfectly to T_K at $z \sim 17$. Gas becomes hotter than CMB at $z \sim 14$. The timing of these critical points in the evolution of T_K is consistent with [54]. Dot-dashed lines take instead $f_X = 0.2$ meaning that the proportionality between star formation and X-ray heating is smaller. As expected, since X-ray heating will be less important, all the evolution is delayed compared to the one with $f_X = 1$ (the IGM starts to heat up at $z \sim 17$ and becomes hotter than CMB at $z \sim 11$). Fig. (11) considers instead Pop.III star formation again inside atomic cooling halos ($m_{min} = m_4$, $f_\star = 0.01$, N_α=4800 and $f_{rec} = 0.63$). In this case, Lyman-α coupling is less efficient (T_S stays coupled to CMB for much longer). The evolution of T_K for $f_X = 1$ is delayed compared to the one obtained for Pop.II with the same f_X reflecting the much lower star formation efficiency $f_\star$. Dot-dashed lines now assume $f_X = 5$ making the X-ray heating more efficient. These plots help us to assess the role in the evolution of the gas temperature of each of the free parameters we have introduced so far. Having the temperature evolution and the ionization history we are now ready to compute the 21cm global signal.

2.3 The evolution of the global signal

From the ionization history computed in Section 1.3 (see Fig. 5) and the thermal history just shown (Fig. 10) the 21cm signal in Fig. (12) arises. In order to obtain this plot, Eq.

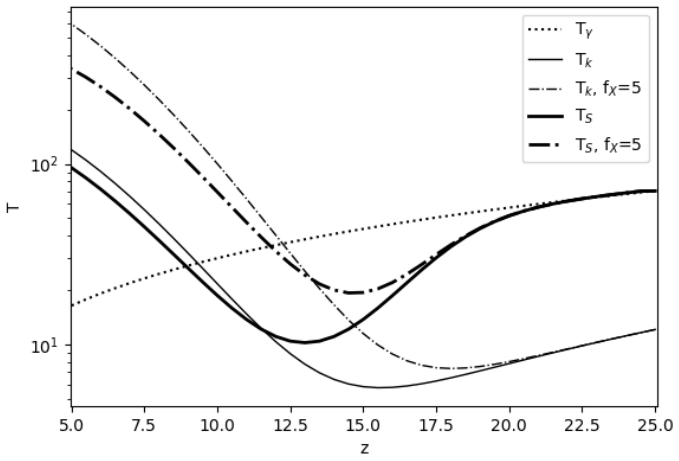

Figure 11: Same as Fig. 10 but assuming only Pop III star formation (see text). Solid lines assume $f_X = 1$ while dot-dashed lines $f_X = 5$. Dotted line shows the evolution of CMB temperature ($\propto (1+z)$).

(66) has been rewritten as:

$$\delta T_b = 26.8 x_{HI}(1+\delta)\left(\frac{\Omega_b h^2}{0.023}\right)\left(\frac{0.15}{\Omega_m h^2 \frac{1+z}{10}}\right)^{1/2}\left(1-\frac{T_\gamma}{T_S}\right) mK \tag{96}$$

and $x_{HI} = 1 - \bar{x}_i$.

The ionization history impacts mainly on the timing at which the 21cm signal vanishes. By $z \sim 7$ reionization is completed making $x_{HI} = 0$, thus $\delta T_b = 0$. The thermal history instead determines the shape of the signal at all redshifts. At z=25 (our initial point), $T_S = T_\gamma$ so the signal is null. With initial star formation, we have the production of Lyman-α photons that starts to couple T_S to T_K. At high redshifts $T_S < T_\gamma$ so we expect to see the signal in absorption. The amplitude of the absorption signal increases until it reaches a maximum (at z$\sim$16) that corresponds to the minimum in the spin temperature evolution (more correctly it is given by the largest difference between T_γ and T_S). Then, as T_S is almost perfectly coupled to T_K that is increasing, the amplitude of the 21cm signal is decreasing until the signal starts to be seen in emission. This transition ($z \sim 14$) corresponds to the point at which the IGM becomes hotter than the CMB. Then $T_K \simeq T_S >> T_\gamma$, the signal saturates and the subsequent evolution will be determined only by the amount of neutral hydrogen (thus by the ionization history). With this simple example, it is now clear how thermal and ionization histories determine the shape of the 21cm global signal (or reversely how to recover information about early conditions of the IGM using 21cm observations). The remaining part of this subsection will be devoted to show some 21cm histories that account for various stellar populations or different prescriptions for star formation.

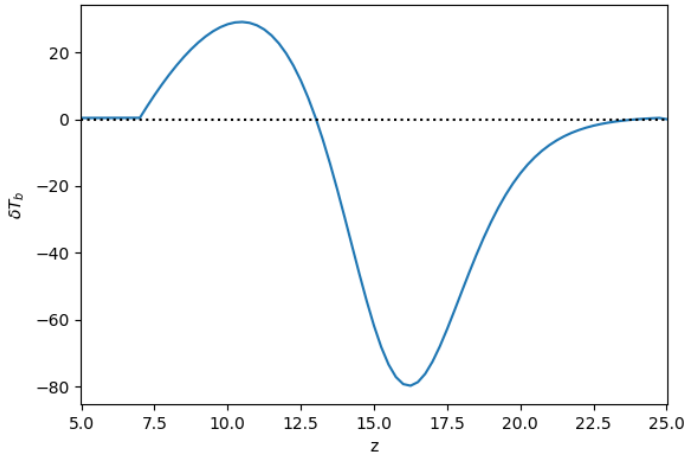

Figure 12: Differential brightness temperature (in mK) vs redshift using thermal and ionization histories computed in Sec. 1.3 and 2.2.

As a reference model, we will consider the 21cm signal in the redshift range $6 \leq z \leq 40$ generated from Pop.II stars forming in atomic cooling dark matter halos. This model has been chosen in order to match the standard 21cm signal generated by Cohen et al. (2017) [29] so the following parameters are adopted: $\Omega_\Lambda = 0.685, \Omega_m = 0.315, \Omega_b = 0.0487, h = 0.673, \sigma_8 = 0.829, f_X = 1, f_\star = 0.05, \zeta = 20$ (the ionizing efficiency defined in Section 1.3.1) and the other parameters for Pop.II stars already discussed. The ionization history for an ionizing efficiency $\zeta = 20$ and a clumping factor C given by Eq. (53) is the one shown in Fig. 5, the 21cm signal is instead shown in Fig. 13. This plot is quite similar to the previous one (Fig. 12) with a stronger and earlier absorption feature; in this section we will refer to this plot as the "standard" 21cm model.

If instead we consider that stars can form also inside molecular cooling halos ($m_{min} = m_3$), we expect to have more star formation, hence more X-rays and ionizing photons causing a faster thermal and ionization evolution of the IGM. In particular, we have considered two different models (A1 and A2): both account for star formation in molecular cooling halos but they differ in the ionizing efficiency ζ (20 for A1, 200 for A2). A1 model thus considers that stars forming in molecular cooling halos have same emitting properties of Pop.II stars forming in atomic cooling halos, while A2 accounts for stars that are producing more ionizing photons than the standard case (which is likely the case for Pop.III stars). We show the ionization history and the 21cm signal for these 2 models in Figs. (14) and (15). We can see that model A1 completely reionize the IGM a bit earlier than the standard case resulting in a Thomson scattering optical depth higher than the standard case (and no longer in agreement with Planck measurements) and in an earlier suppression of the 21cm signal. The absorption feature in the global signal has a smaller amplitude than the standard case since the IGM is heated up very soon and when Lyman-α heating becomes effective the hydrogen is already quite hot. The A2

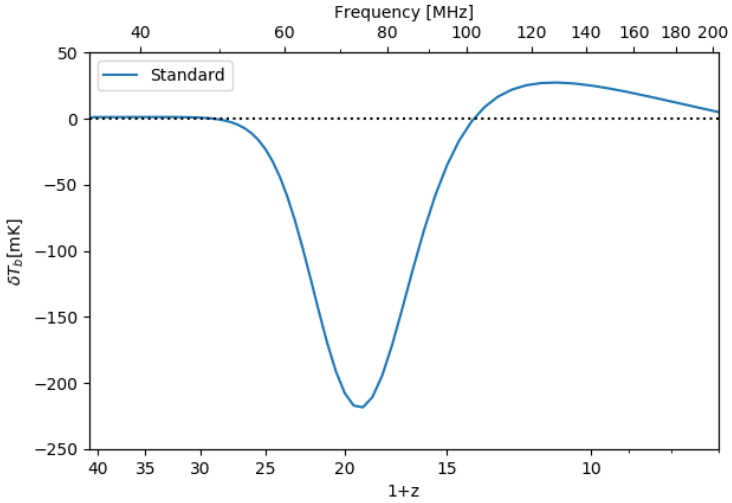

Figure 13: 21cm signal generated in accordance with [29] (differential brightness temperature vs 1+z in log-scale). The top x-axis shows the corresponding observed frequency of the signal.

case is even more extreme since, due to the higher ζ, the ionization proceeds extremely fast and full reionization is reached at $z \sim 17$. This reflects also on the signal that is suppressed before that IGM becomes hotter than the CMB (and so it can be seen only in absorption). This case is extremely unlikely as we know that Pop.III star formation does not proceed at all redshifts and this is proven also by the value of τ_e obtained which is not consistent with any of the constraints given by WMAP and Planck missions.

A first correction to A models is done considering that in molecular cooling halos $m_3 \leq m_{min} < m_4$ we have Pop.III star formation (with $\zeta = 20$) while in more massive halos we have Pop.II star formation ($\zeta = 20$). This case is denoted as "case B" and as usual we plot ionization history and the 21cm signal (Figs. 16 and 17). However, this correction has a small impact on the evolution of x_i with respect to model A2 since we are not shutting down star formation in molecular cooling halos (we are simply distinguishing two scenarios of star formation). For this reason, case B evolution is almost identical to A2 case (reionization is slightly slower).

Now we introduce the new parameter z_{trans}. This is the redshift at which we shut down Pop.III star formation in molecular cooling halos. This parameter should mimic the effect of the Lyman-Werner background (see Section 1.2) responsible for the transition in star forming halos from m_3 to m_4. This is however a very simplified treatment of this transition since we are assuming the IGM to be perfectly uniform such that this transition occurs at the same redshift in every region of the IGM. With the letter C we indicate the scenario where for $z > z_{trans}$ we have Pop.III and Pop.II stars forming in molecular and atomic cooling halos, respectively (like case B), while for $z \leq z_{trans}$ we allow only Pop.II star formation in atomic cooling halos (like the standard case). To investigate with more accuracy this model we consider three different values for z_{trans}: 25, 20 and

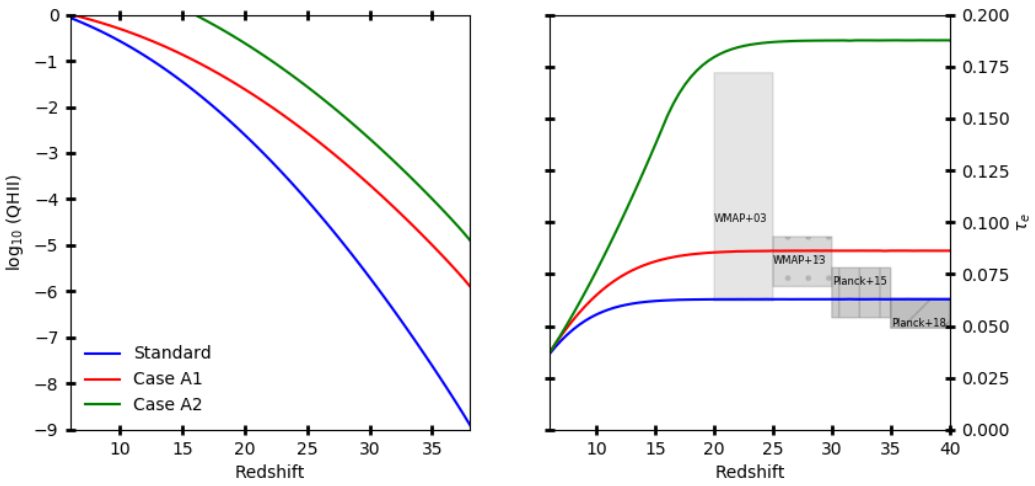

Figure 14: Ionization history and τ_e for Standard, A1 and A2 case (see in the text for details).

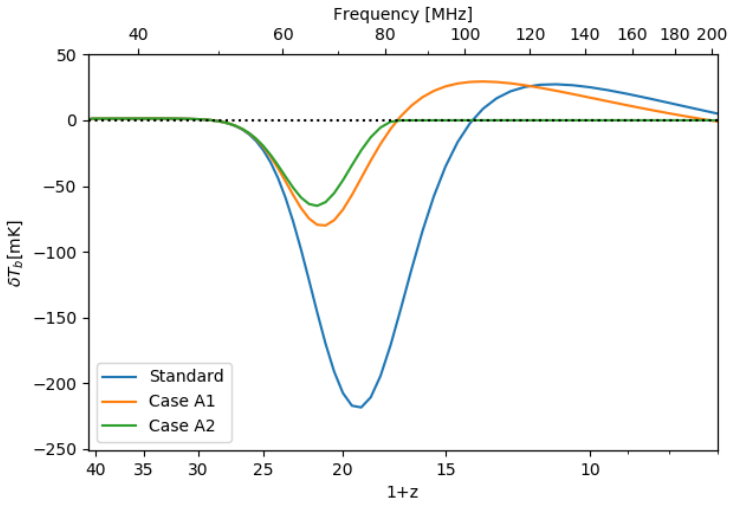

Figure 15: 21cm global signal for Standard, A1 and A2 models (see the text for details).

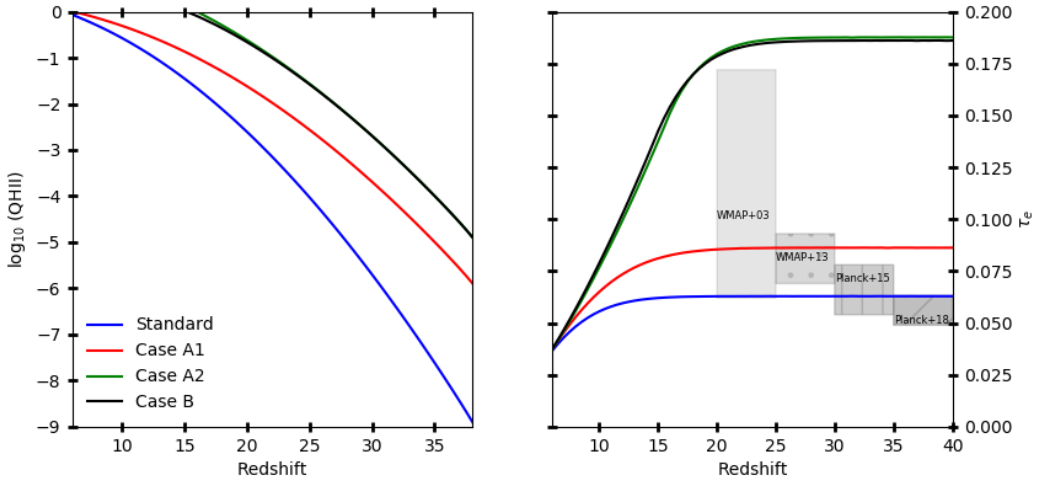

Figure 16: Ionization history and τ_e for Standard, A1, A2 and B models (see the text for details).

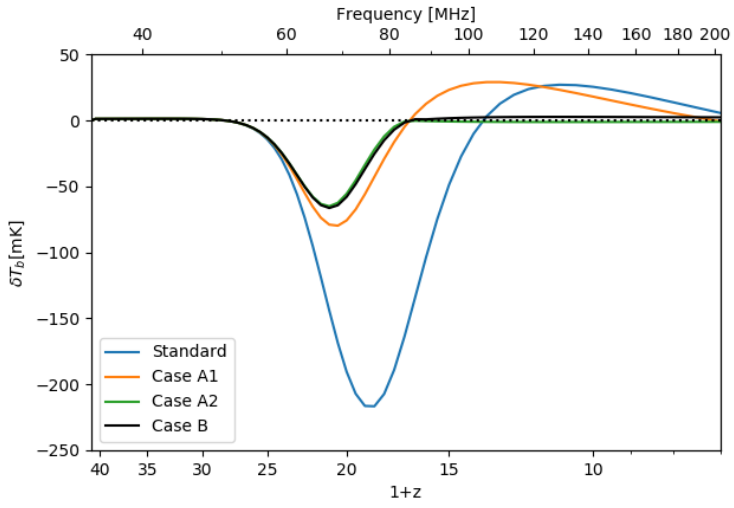

Figure 17: 21cm global signal for Standard, A1, A2 and B models (see the text for details).

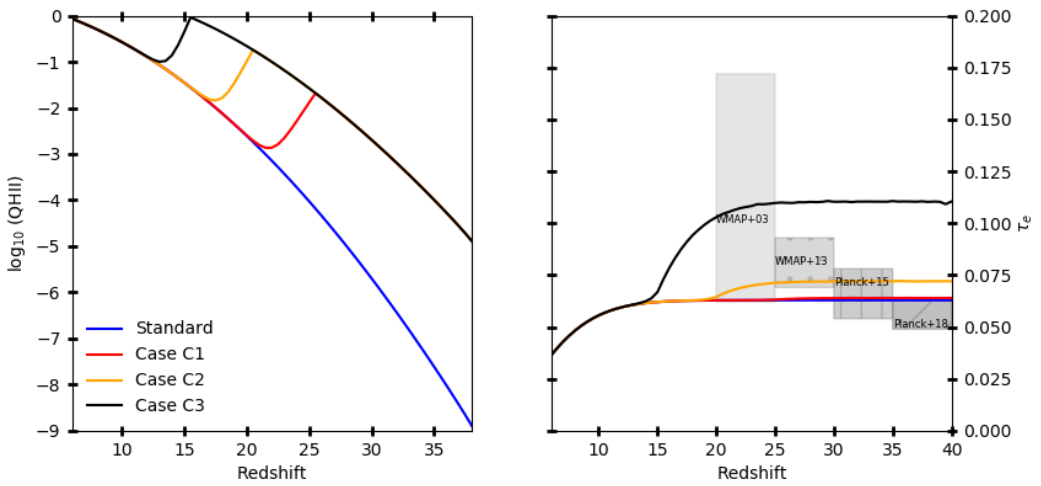

Figure 18: Ionization history and τ_e for Standard, C1, C2 and C3 models (see the text for details).

15 (respectively models C1, C2 and C3). In the left panel of Fig. (18) it is clearly visible the drop in the global ionized hydrogen fraction at $z = z_{trans}$. This delays the redshift of complete reionization and consistently decreases the Thomson scattering optical depth (in closer agreement with observations). For what concerns ionization histories, case C3 is very similar to the standard case while case C1 has a very high value of τ_e. Among the three cases, the most interesting one is C2 ($z_{trans} = 20$) since we obtain a value of τ_e consistent with Planck 2015 measurements [110]. All global signals show a shallower absorption feature meaning that Pop.III stars are very efficient in heating up the gas at moderate-high redshifts.

To conclude this analytical treatment of 21cm signal, a comparison between all the models (for C-models we show only case C2) is shown in Figs. (20) and (21).

These first simplified calculations show that determining the number of sources as well as their emitting properties is crucial to predict the shape of the 21cm global signal; Pop.III stars likely starts to heat up the gas at higher redshift causing a shallower absorption feature in the signal. However, it is important to stress the fact that this is a very simplified treatment as *(i)* we considered only stars as heating and ionizing sources neglecting accreting black holes and *(ii)* this is an analytical calculation based on many simplified assumptions (i.e: Press-Schechter mass function and uniform IGM). We can overcome both these issues moving away from analytical calculations (that require many assumptions/simplifications) to more sophisticated semi-numerical techniques. Recently, these are becoming more and more popular since they can be quite precise without being numerically as expensive as cosmological simulations. [22]

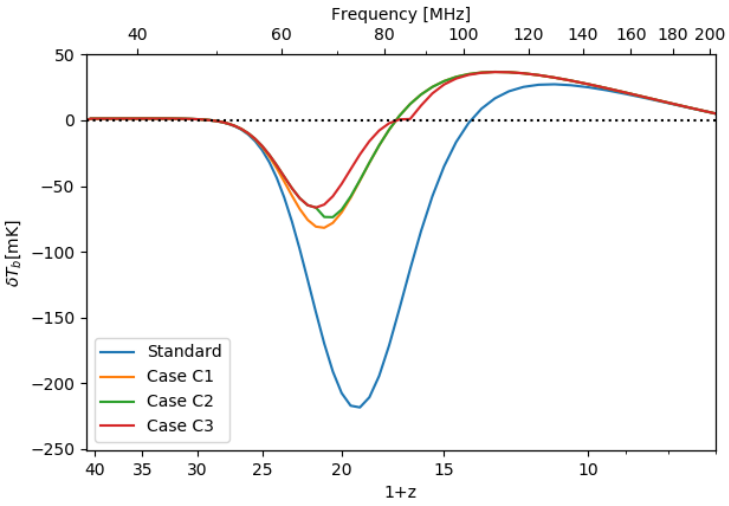

Figure 19: 21cm global signal for Standard, C1, C2 and C3 models (see the text for details).

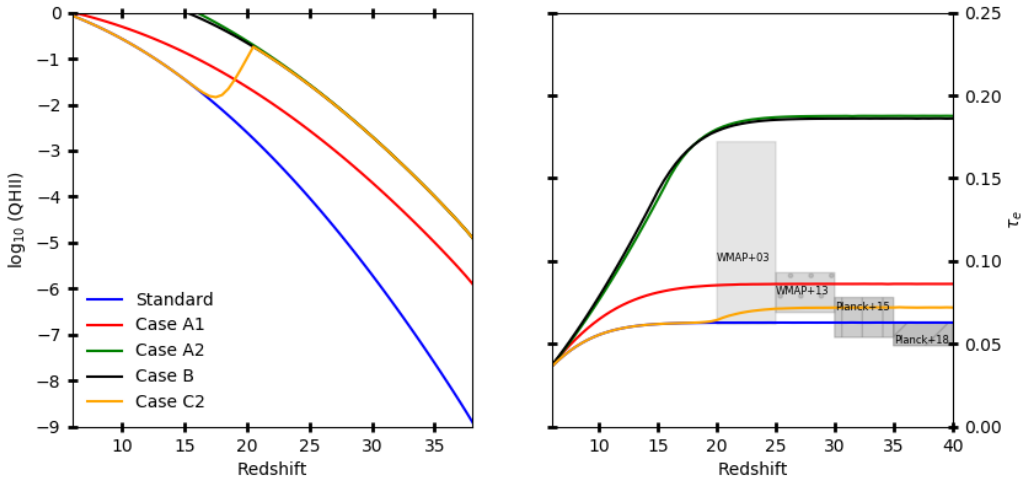

Figure 20: Ionization history and τ_e for Standard, A1, A2, B and C2 case (see in the text for details).

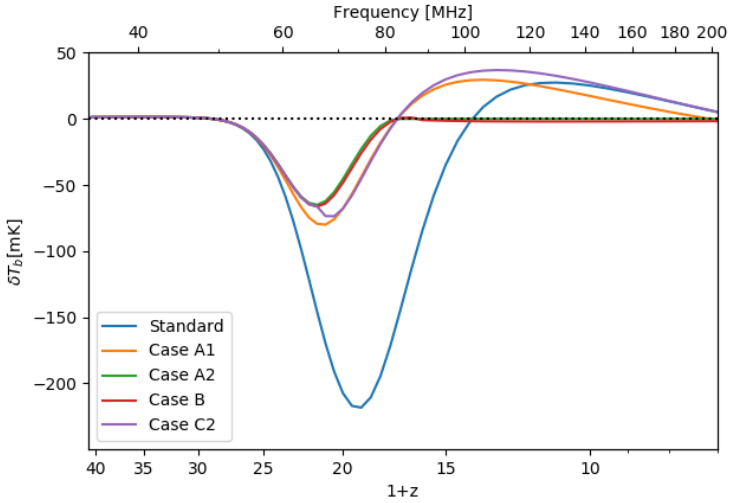

Figure 21: Ionization history and τ_e for Standard, A1, A2, B and C2 case (see in the text for details)

3 CAT

In this section, we will present the semi-numerical code adopted throughout this work: the Cosmic Archaeology Tool (CAT) [153]. This code was first developed to investigate the early evolution of the first supermassive black holes, but since it describes the formation of first stars and BHs in a self-consistent way and follows the co-evolution of nuclear BHs and their host galaxies at z>4 its outputs are useful also to estimate the strength of the 21cm signal generated from the first stars and BHs. In this case, star formation is no longer evaluated through analytical calculations as done in Section 2; this requires to update the various equations used to estimate the background at different wavelengths (UV, Lyman-α, X).

3.1 The structure of CAT

CAT is able to follow both the dark matter and baryonic evolution through two different algorithms implemented in there. The redshift distribution of dark matter halos is described by the galaxy formation model GALFORM [27] [108] that adopts a Monte Carlo dark matter halo merger tree algorithm. The baryonic evolution is tracked by GAMETE/QSOdust (GQD) [155] which is based on various prescriptions for the formation and evolution of each baryonic component (stars, BHs, gas and dust). Now we will deeply discuss each of these two algorithms present in CAT.

3.1.1 GALFORM

GALFORM is a semi-analytical model of galaxy formation that is able to reconstruct the hierarchical merger history (or *Merger tree*) of a given dark matter halo. This Monte-Carlo algorithm, based on the Extended Press-Schechter theory, was originally developed by Cole et al. (2000) [27] and then improved by Parkinson et al. (2008) [108] who perturbed the basic function that drives the algorithm obtaining first-order corrections. GALFORM starts with a DM halo at redshift z_0 of a given mass and follows its evolution back in time reconstructing its progenitors; to understand this process we need to take the definition of the conditional mass function given by the Extended Press-Schechter theory [27]:

$$f(M_1|M_2)d\ln M_1 = \sqrt{\frac{2}{\pi}}\frac{\sigma_1^2(\delta_1-\delta_2)}{[\sigma_1^2-\sigma_2^2]^{3/2}}\exp\left[-\frac{1}{2}\frac{(\delta_1-\delta_2)^2}{(\sigma_1^2-\sigma_2^2)}\right]\left|\frac{d\ln\sigma}{d\ln M_1}\right|d\ln M_1 \tag{97}$$

where f($M_1|M_2$) represents the fraction of mass of halos of mass M_2 at redshift z_2 that is contained in progenitor halos of mass M_1 at an earlier redshift z_1. $\delta_{1,2}$ and $\sigma_{1,2}$ are the linear density thresholds for collapse and the linear density fluctuations inside spheres already defined in Section 1.1.1 for the two DM halos considered. Eq. (97) allows to compute the mean number of halos of mass M_1 into which a halo of mass $M_2 > M_1$ splits after a step up in redshift dz_1 [27]:

$$\frac{dN}{dM_1} = \frac{1}{M_1}\frac{df}{dz_1}\frac{M_2}{M_1}dz_1 \tag{98}$$

The halo is thus decomposed into its progenitors. In order to recover the entire merger tree we just need to repeat this process until the maximum redshift of our interest z_{max} is reached. Actually, the extended Press-Schechter formalism adopted so far, systematically underestimates the mass of the most massive progenitor halos with increasing redshift [108]. This motivates the modification of Eq. (98) introducing a perturbing function G($\sigma_1/\sigma_2, \delta_2/\sigma_2$):

$$\frac{dN}{dM_1} \rightarrow \frac{dN}{dM_1}G(\sigma_1/\sigma_2, \delta_2/\sigma_2) \tag{99}$$

$$G(\sigma_1/\sigma_2, \delta_2/\sigma_2) = G_0\left(\frac{\sigma_1}{\sigma_2}\right)^{\gamma_1}\left(\frac{\delta_2}{\sigma_2}\right)^{\gamma_2} \tag{100}$$

where G_0, γ_1 and γ_2 are free parameters. These are properly tuned in order to obtain an accurate agreement with the Millennium Simulation [143], one of the most popular N-body simulations.
In this work the GALFORM algorithm has been used to generate merger trees for DM halos with masses $10^{9.5} \leq M \leq 10^{14}$ at z=4. This mass range has been divided into 10 logarithmically spaced bins with size 0.5 and for each bin a final halo of mass equal to the central bin value has been considered as a starting point for the code to simulate 10 independent halo merger trees; the total merger tree sample accounts thus for 100 merger trees. The resulting redshift dependent mass distributions of each mass bin

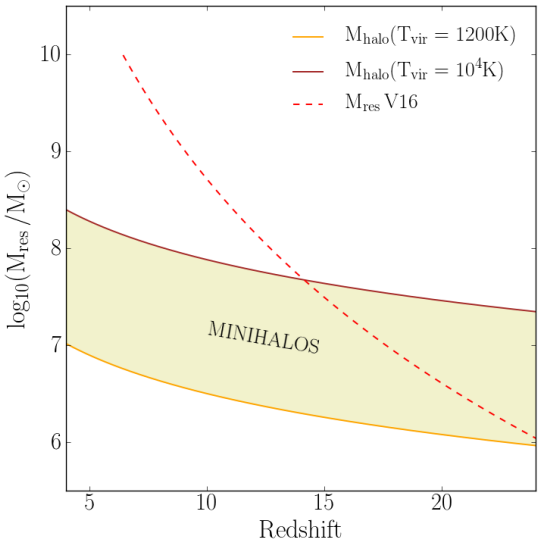

Figure 22: Mass resolution when generating GALFORM merger trees (orange solid line) and merger tree mass resolution of Valiante et al. (2016b, red dashed line) [157] as a function of redshift. For comparison, we also show the redshift dependent minimum mass of atomic cooling halos (brown solid line) so that the yellow shaded region illustrates the masses of dark matter minihalos with 1200K$\leq T_{vir} \leq 10^4$K. Figure taken from Trinca et al. (2021) [153].

are weighted according to the number density of DM halos at redshift z=4, as given by the Sheth and Tormen mass function [137] (see end of section 1.1.2). In our setup $z_{max} = 24$ and there are 800 time steps logarithmically spaced between z=24 and z=4; this makes time steps larger for smaller redshifts ($\sim 4Myr$ at $z \sim 4$, $\sim 0.5Myr$ at $z \sim 20$). The main consequence of this poor time resolution is that merger events can involve more than 2 DM halos allowing multiple mergers. With this algorithm, going enough back in time ($z \sim 20 - 30$), we can achieve a high enough mass resolution to track the evolution of "minihalos" (systems with $T_{vir} \leq 10^4 K$). As already stressed, these systems are extremely important as they are believed to host the very first Pop.III star formation before the Lyman-Werner background is built up. To conclude the discussion about GALFORM, in Fig. (22) it is shown the mass resolution as a function of redshift adopted in CAT (solid orange line) compared to the one adopted in Valiante et al. (2016b) [157] (red dashed line). Adopting the GALFORM algorithm, CAT largely improves the statistics of minihalos compared to the previous version of GAMETE/QSOdust.

3.1.2 GAMETE/QSOdust

Inside CAT, GALFORM rules the dark matter physics while the baryonic evolution is determined by GAMETE/QSOdust (GQD), a semi-analytical model introduced by Valiante et al. (2011) [155] that follows: BH formation and evolution (considering both coalescence and gas accretion), star formation, evolution of the ISM (gas and dust), dust formation (in SN ejecta and in AGB stars) and supernova and AGN feedback. This model was developed to study the origin of z>6 quasars, tracing the formation history of their nuclear supermassive black holes and of their host galaxies. All the free parameters that regulate the various physical processes implemented in GQD have been calibrate to reproduce the observed properties of the quasar SDSS J1148+5251 at z=6.4, a very well known and thoroughly studied system that has been used as a prototypical example of z>6 quasar [155]. This code has been applied to study the co-evolution of SMBHs with their host galaxies, the properties of BH seeds and the early binary BHs formation [155] [156] [157] [158] [159] [160]. For our purposes, we are mostly interested in the evolution of BH accretion and star formation.
Along a merger tree, each progenitor galaxy can form stars according to the available gas budget M_{gas} [123]. The global SFR inside a protogalaxy is given by:

$$SFR = f_{cool} M_{gas} f_{\star} / \tau_{dyn} \tag{101}$$

where τ_{dyn} is the halo dynamical time, $f_{\star}$ is the star formation efficiency (it is one of the free parameters of this model) and f_{cool} quantifies the cooling efficiency. The various feedback processes have a key role in the evolution of star formation as they regulate many parameters in Eq. (101). GQD accounts for them through different prescriptions:

- *Radiative Feedback*
  Radiative feedback regulates f_{cool} and $f_{\star}$ through two main processes: photo-dissociation and photo-heating (both have been already discussed in Section 1.3.1). Star formation in minihalos occurs through molecular cooling. This mechanism relies on the amount of H_2 which can be dissociated by the Lyman-Werner background. In GQD, we can account for this effect with the parameter f_{cool}. In particular, we set $f_{cool} = 1$ in atomic cooling halos while lower values are taken in minihalos depending on the virial halo temperature T_{vir}, redshift, metallicity and Lyman-Werner flux J_{LW} [157] [123]. Unlike photo-dissociation that impacts only on star formation in molecular cooling halos, photo-heating, can inhibit star formation even inside atomic cooling halos. This effect is accounted in GQD by $f_{\star}$. We take $f_{\star} = 0$ when T_{vir} is below than the IGM temperature T_{IGM}. This is computed as $T_{IGM} = Q_{HII}(z) T_{reio} + [1 - Q_{HII}(z)] T_{gas}$ with $T_{reio} = 2 \times 10^4 K$ the post-reionization temperature, $T_{gas} = 170K[(1+z)/100]^2$ and $Q_{HII}(z)$ the filling factor (defined in Section 1.3) [123].

- *Mechanical feedback*
  Mechanical feedback affects the amount of gas available for star formation (M_{gas}). The two relevant processes that drive gas outflows from galaxies are SN explosions

and the winds powered by the energy released during BH accretion (AGN feedback). These two outflow rates are respectively described as follows [153]:

$$\dot{M}_{ej,SN} = \frac{2E_{SN}\epsilon_{w,SN}R_{SN}(t)}{\nu_e^2} \tag{102}$$

$$\dot{M}_{ej,AGN} = 2\epsilon_{w,AGN}\epsilon_r\dot{M}_{accr}\left(\frac{c}{\nu_e}\right)^2 \tag{103}$$

$R_{SN}(t)$ is the SN explosion rate and E_{SN} the average explosion energy per SN (2.7×10^{52} for Pop.III stars, 1.2×10^{51} for Pop.II stars, from [157]), $\dot{M}_{accr}$ is the gas accretion rate, ϵ_r the AGN radiative efficiency and ν_e the escape velocity of the gas. In the two above equations we have two new free parameters that must be calibrated: the SN- and AGN-driven wind efficiencies ($\epsilon_{w,SN}$ and $\epsilon_{w,AGN}$ respectively).

- *Chemical feedback*
  Adopting the same formalism in Valiante et al. (2016b) and in Sassano et al. (2021) [157] [123], stars in GQD form according to a Larson IMF [86]:

$$\phi(m_\star) \propto m_\star^{\alpha-1}\exp(-m_{ch}/m_\star) \tag{104}$$

with m_{ch} the characteristic mass ($20M_\odot$ for Pop.III stars and the possible range of stellar mass is $10M_\odot \leq m_\star \leq 300M_\odot$, $0.35M_\odot$ for Pop.II/I stars with $0.1M_\odot \leq m_\star \leq 100M_\odot$), $\alpha = -1.35$. The critical metallicity that defines the transition Pop.III/Pop.II stars is set at $Z_{cr} = 10^{-3.8}Z_\odot$ in accordance with de Bennassuti et al. (2014) [33]. Evolving stars progressively enrich the IGM with metals and dust and their abundances depend on the evolutionary stage of the star. The values adopted are taken from van den Hoek & Groenewegen (1997) and Zhukovska et al. (2008) for AGB stars (1-8 $M_\odot$) [161] [172], Woosley & Weaver (1995) and Bianchi et al. (2009) for core-collapse SNe (10-40$M_\odot$) [166] [9] and Heger & Woosley (2002) and Bianchi et al. (2009) [68] [9] for pair-instability SNe (140-260$M_\odot$). Pop III stars are assumed to evolve instantaneously (i.e. their lifetime is the characteristic time-interval of the merger tree), while Pop II/I stellar lifetimes are computed according to the parametric form proposed by Raiteri et al. (1996) [116] and depend on the stellar mass and metallicity [123].

Supermassive BHs are considered to form via both gas accretion and mergers starting from less massive progenitors commonly referred to as *seeds*. Without going into too many details, we can divide these seeds by mass into two categories: light seeds ($\sim 10 - 10^3 M_\odot$) coming from Pop.III remnants [66] [94] and heavy seeds ($\sim 10^4 - 10^5 M_\odot$) formed after a direct collapse of a giant molecular cloud mediated by the formation of a super-massive star [17] [78]. The relative importance of these two channels is extensively discussed in [157] [73]. After the formation of BH seeds, we need to consider their growth via gas accretion and coalescence. Following Valiante et al. (2011) [155], we will assume that a merger event between two BHs can occur only if the mass ratio of their interacting

host DM halos is $\mu > 1/10$ (considering two DM halos with $M_1 > M_2$, $\mu \equiv M_2/M_1$); the characteristic time interval of the merger event is comparable with the time step of CAT simulation [153]. BH accretion is instead ruled by the Bondi-Hoyle-Lyttleton (BHL) accretion rate [12] [72] given by:

$$\dot{M}_{BHL} = \alpha \frac{4\pi G M_{BH}^2 \rho_{gas}(r_A)}{c_s^3} \tag{105}$$

where c_s is the sound speed and $\rho_{gas}(r_A)$ is the gas density evaluated at the Bondi radius $r_A = 2GM_{BH}/c_s^2$ (i.e. the radius of gravitational influence of the BH). This gas distribution is approximated as an isothermal sphere with a flat core (see expression in [157]). The parameter α does not appear in the original BHL model but it is usually introduced in numerical simulations. This is a correction factor accounting for the enhanced gas density in the inner regions around the central BH. As it has been discussed by Schaye et al. (2015) [128], due to the lack of resolution of the simulations, the actual BHL accretion rate tends to be strongly underestimated. α becomes then the fourth free parameter introduced in CAT. The BH accretion in GQD/CAT cannot exceed the Eddington limited so that $\dot{M}_{accr} = \min(\dot{M}_{BHL}, \dot{M}_{Edd})$ with M_{Edd} computed from the standard definition of the Eddington luminosity L_{Edd} as $M_{Edd} = \frac{L_{Edd}}{\epsilon_r c^2}$ and taking $\epsilon_r = 0.1$.
These baryonic prescriptions allow us to associate to each DM halo in a merger tree simulation many baryonic quantities (e.g. SFR, BH accretion rate, metallicity etc.). However, for the computation of the 21cm global signal, we will be mostly interested in cosmic mean quantities rather than in local quantities. After having run a CAT simulation of 100 merger trees as described in Section 3.1.1, we will have quantities referring to each DM halo participating to the merger history of each considered galaxy at z=4; from such an output we need to recover the global quantities. Hereafter we will briefly describe how to do this: as an example we will show how to move from the SFR inside each DM halo to the comoving star formation rate density. We start by considering one merger tree of a $10^{9.5} M_\odot$ DM halo at z=4. Inside this merger tree, for each of the 800 redshift steps, we sum all the SFR of DM halos present at that redshift. After this passage we end up with the total SFR at every redshift for the merger tree considered. We then repeat this operation for all the 10 merger trees of the $10^{9.5} M_\odot$ halo at z=4, we sum these contributions and then divide by the number of merger trees (10). This procedure must be done also for all the other merger trees for DM halos of different mass at z=4. Now, we simply need to weight the obtained results for each merger tree, according to the number density of DM halos at z=4 as given by the Sheth and Tormen mass function. In practice, to each halo is associated a certain comoving number density dN/dM (in Mpc^{-3}) that multiplies the total SFR of merger trees of different halo masses. In this way we are considering that low-mass halos are more frequent than high-mass halos, so, merger trees of $10^{9.5} M_\odot$ will weight more than merger trees of $10^{14} M_\odot$ to the total contribution of the SFRD. This procedure described for the case of SFR will be repeated whenever we need to move from a local quantity to a global one and it will be frequently applied in Section 3.2.

3.1.3 Model calibration

As already stressed, CAT depends on some free parameters that need to be calibrated. For the DM merger trees we need to tune G_0, γ_1 and γ_2 in Eq. (100) in order to obtain merger histories consistent with the N-body Millennium simulation. For the baryonic evolution instead there are four free parameters: the star formation efficiency $f_\star$ that determines the global SFR in Eq. (101), the SN and AGN wind efficiencies $\epsilon_{w,SN}$, $\epsilon_{w,AGN}$ present in Eqs. (102) and (103) for the gas outflows and the BH accretion parameter α in Eq. (105). In the first version of GQD presented in Valiante et al. (2011) [155] these were tuned to reproduce the SMBH mass and the properties of the host galaxy of SDSSJ1148+5251 at z = 6.4 [45]; in this version of GQD implemented in CAT instead we will follow Trinca et al. (2021) [153] who tune the free parameters in order to reproduce a realistic population of galaxies and AGNs at z>4. First, we require the accordance between our model and the observed total star formation rate density (SFRD) which measures the total stellar mass formed per unit time in a comoving volume. Then we compare the mass and bolometric luminosity of the most massive systems hosting accreting BHs predicted by CAT at z>5 with the values inferred from quasar observations at similar redshifts. Our reference model takes $f_\star = 0.05$, $\epsilon_{w,SN} = 1.6\times10^{-3}$, $\epsilon_{w,AGN} = 2.5 \times 10^{-3}$ and $\alpha = 90$. Some model variants are considered in Trinca et al. (2021) [123] [153], but in this work we will focus only on this reference model. To conclude this discussion about CAT we show the redshift evolution of the comoving SFRD in Fig. (23) and the bolometric luminosity as a function of the black hole mass for high redshift quasars Fig. (24) taken from [153] (the bolometric luminosity is simply evaluated as $L_{bol} = \epsilon_r \dot{M}_{accr} c^2$). Solid and dashed red lines in Fig. (23) refer to the comoving SFRD when all CAT galaxies and CAT galaxies with $M_{UV} < -17.7$ are considered. This cut at $M_{UV} = -17.7$ reflects the current observational limits of UV surveys: accounting for galaxies with $M_{UV} < -17.7$ means that we are considering only the detectable sources. From Fig. (23) it is evident that our reference model is in good agreement with the observed SFRD (the dashed red line is consistent with different observations reported in the legenda); however CAT predicts a large number of currently undetected sources ($M_{UV} > -17.7$), which dominate the SFRD at z>4 (solid red line). Looking instead at Fig. (24), results of the reference model at z=5,6,7 are shown as yellow, orange and dark red points, while the empty black points are the observations of all z>5.8 quasars. Our CAT simulated samples is mainly constituted by low-mass objects with only few objects with a mass comparable to the observed sample. Despite our limited statistics, the most massive BHs predicted by CAT at similar redshifts populate the observed range of quasar masses and luminosities showing that our choice for the value of the free parameters is consistent with observations.

3.2 CAT and the 21cm signal

For each merger tree simulation, CAT provides the main physical properties of stars, BHs, gas and dust inside each DM halo; some of these quantities (like the SFR) will allow us to estimate the expected 21cm signal in post-processing. Estimating the 21cm

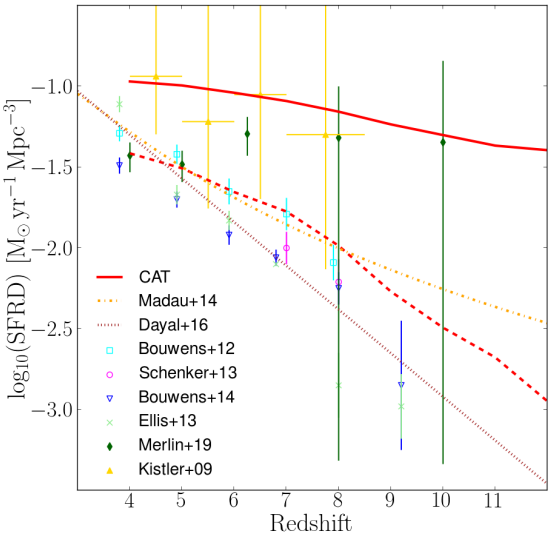

Figure 23: Redshift evolution of the comoving SFRD when the entire galaxy population is considered (red solid lines) and when only galaxies with $M_{UV} < -17.7$ are accounted for (red dashed lines, see the text the motivation for this choice). Model predictions are compared with different observational results: González et al. (2011), Bouwens et al. (2012), Labbé et al. (2013), Stark et al. (2013), Schenker et al. (2013), Ellis et al. (2013), Duncan et al. (2014), Bouwens et al. (2014), Oesch et al. (2014), Grazian et al. (2015), Song et al. (2016) ([60] [13] [85] [144] [129] [40] [35] [14] [107] [61] [141]). The yellow dashed-dotted line shows the empirical SFRD by Madau & Dickinson (2014) [95] while the brown dotted line shows the model prediction by Dayal et al. (2016) [32]. Figure taken from Trinca et al. (2021) [153]

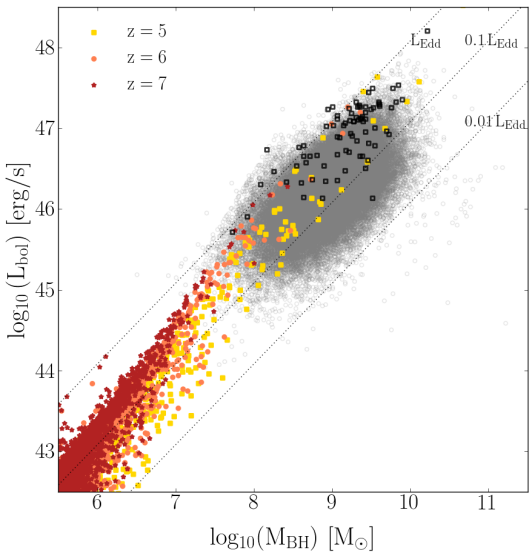

Figure 24: Bolometric luminosity as a function of the black hole mass for high redshift quasars. Colored data points represent the quasar sample of the CAT reference model at z=5 (yellow), 6 (orange), and 7 (red). Black empty squares represent a collection of observed quasars at redshift 5.8<z<7.5, while grey data show a large sample of quasars between 0.6<z<2 drawn from the SDSS-DR7 quasar catalog by Shen et al. (2011) [135] and for which MgII-based BH masses have been derived. Dotted lines marks the position of BHs with $L_{bol} = L_{Edd}$, $0.1L_{Edd}$ and $0.01L_{Edd}$. Figure taken from Trinca et al. (2021) [153]

global signal starting from CAT represents a marked improvement with respect to the analytical calculations done in Section 2, not only because now we will consider also BHs as sources able to ionize and heat up the IGM, but also because we can now drop many simplifications adopted in Section 2 relying only on physical prescriptions implemented in CAT and on the calibration of the free parameters already discussed. For this reason, the formalism used to evaluate the 21cm global signal starting from CAT outputs is slightly different from the one adopted in Section 2 where only analytical calculations were used. The main difference is that quantities like the SFR that in Section 2 were estimated starting from the collapse fraction derived from the Press-Schechter halo mass function now are directly taken from CAT outputs. In particular, starting from CAT and using some relations that link the photon production with the rate of star/BH formation, we will be able to derive the rate of photon production at the interesting wavelengths (UV ionizing, Lyman-α, X). Starting from these quantities, we can compute the evolution of T_K, T_S and δT_b using the Eqs. (82), (68) and (96) already found in Section 2. As stressed in Section 3.1.1 and 3.1.2, we need to remember that the contribution of merger trees of different halo mass have to be weighted according to the number density of DM halos at z=4 derived by the Sheth-Tormen mass function. Considering 100 merger trees of 10 different halo masses ensures a complete and robust statistics and constitutes a representative sample of the halo population at $4 \leq z \leq 24$. Since CAT simulation runs in this redshift range, also the 21cm global signal will be evaluated at this epoch. Before discussing the various contributions to the UV, Lyman-α and X background of stars and BHs we will rewrite the equations to compute the ionization history and the Lyman-α flux in a more practical way.

We have already shown in Section 1.3 that the ionized volume is determined by the total number of ionizing photons Q_i (see Eq. 46); instead of looking for an expression for the total number of ionizing photons, we will evaluate it from CAT outputs and the result obtained will be taken as an input value to determine the global ionization history. We will thus use the solutions given by Eqs. (47) and (48) as a function of redshift:

$$Q_{HII}(z_{obs}) = \frac{f_{esc}}{\bar{n}_H^0} \int_{z_{obs}}^{\infty} dz \left|\frac{dt}{dz}\right| \dot{Q}_i e^{F(z_{obs},z)} \tag{106}$$

$$F(z_{obs}, z) = -\alpha_B \bar{n}_H^0 \int_{z_{obs}}^{z} dz' \left|\frac{dt}{dz'}\right| C(z')(1+z')^3 \tag{107}$$

In order to be consistent with the work of Trinca et al. (2021) [153], when CAT outputs are used to recover ionization histories we will use a constant clumping factor C=3 and an escape fraction $f_{esc} = 0.15$. $\dot{Q}_i$ is the ionizing photon rate (number of photons cm^{-3} s^{-1}) sometimes denoted also as $\dot{n}_{ion}$; z_{obs} is the redshift at which we want to compute the filling factor. The expression for the Thomson scattering optical depth which will be used to verify if the agreement with Planck observations is the same found in Section 1.3.3 (Eq. 54). For what concerns thermal histories we need to quantify *(i)* the X-ray heating which determines T_K and *(ii)* the Lyman-α flux necessary to compute T_S. The first contribution depends on whether we are considering stars or BHs, so a deeper discussion will be presented in the next part of this section and in Section 3.2.1. J_α can

be computed from Eq. (87) using the comoving photon emissivity ϵ (number of Lyman-α photons per unit comoving volume, proper time and frequency) computed starting from the output of CAT. Using the formalism adopted by Dayal et al. (2008) [31], we can consider that the amount of Lyman-α photons is set by the amount of UV photons produced by stars and BHs which do not escape from galaxies where they are generated (being so proportional to $Q(1 - f_{esc})$) It is also introduced the factor f_α which is the fraction of Lyman-α photons that escape the galaxy without being destroyed by dust (we will take this parameter to be unity for simplicity). With this assumption we can recover an approximate expression for J_α similar to Eq. (91) found in Section 2.2.2:

$$J_\alpha(z_{obs}) \simeq \frac{c}{4\pi} \int_{z_{obs}}^{\infty} dz \left|\frac{dt}{dz}\right| \frac{(1+z)^2}{H(z)} \frac{\dot{Q}_i(1 - f_{esc})}{\Delta\nu} f_\alpha \tag{108}$$

with $\Delta\nu = \nu_{LL} - \nu_\alpha$ the frequency interval between the Lyman limit and the Lyman-α line. The main advantage of this formalism is that we do not need any new quantity to compute the Lyman-α background since we only use the ionizing UV photon rate needed also to recover the filling factor. All equations are now updated in order to accept CAT outputs as input values, we just need to know how to obtain the ionizing photon rate and the X-ray heating for the two main sources that heated up and reionized our Universe: stars and BHs.

3.2.1 Stellar contribution

The first contribution to the 21cm global signal we will consider comes from stellar emission. The relevant quantities from CAT are: the SFR ($M_\odot$/yr) and metallicity (in order to disentagle between Pop.III/Pop.II contribution) of each star forming galaxy at each redshift. The ionizing (>13.6 eV) photon rate can be recovered using time- and metallicity-dependent UV luminosities from Bruzual & Charlot (2003) [18] for Pop.II stars and from Schaerer (2002) [126] for Pop.III stars in the same spirit of what has been done by de Bennassuti et al. (2017) [34]. Thanks to these works, we are able to associate to each star forming galaxy a certain UV luminosity (or flux) depending on the stellar metallicity and on stellar age. This result is summarized in Fig. (25) taken from [34]. Here we can appreciate the fact that the ionizing photon flux rapidly decreases within the first 100Myr from star formation making the contribution to the total ionizing photon rate of old stellar population almost negligible. As expected, low-metallicity stars have a larger ionizing flux reflecting their higher temperatures and thus their harder spectra. In practice, at each redshift we consider all the star forming galaxies (SFR>0) and for each of these we compute the newly formed stellar mass ($M_\star = SFR \times \Delta t$). For each of these galaxies CAT provides us the stellar metallicity and we can therefore compute the corresponding UV luminosity assuming a stellar age of Δt (1 Myr). This procedure neglects the contribution of older stellar populations, which however is significantly smaller given the rapid drop of the ionizing photon flux with stellar age shown in Fig. (25). Multiplying the total stellar mass by the UV flux, we can obtain the photon rate (number of photons s^{-1}) inside each galaxy participating to the merger

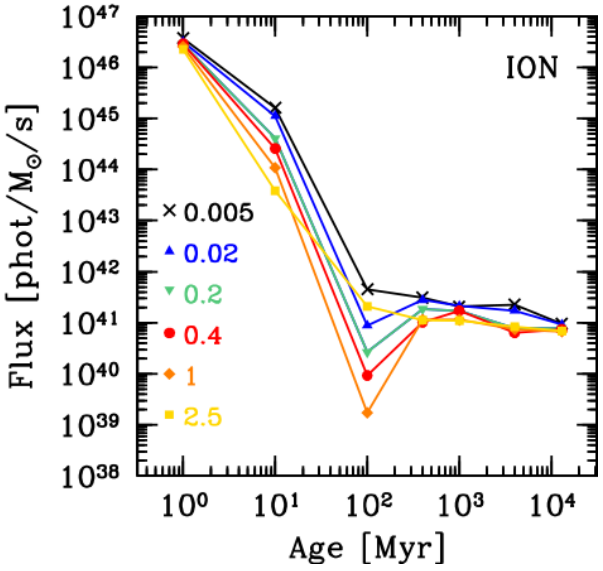

Figure 25: Ionizing photon flux (number of photons $M_{\odot}^{-1}s^{-1}$) for Pop.II stars as a function of stellar age as computed by Bruzual & Charlot (2003) [18]. Different colors refer to different metallicities as shown by the labels: $Z/Z_{\odot} = 0.005$, 0.02, 0.2, 0.4, 1, 2.5 (black crosses, blue up-triangles, green down triangles, red dots, orange diamonds, gold squares). Figure taken from de Bennassuti et al. (2017) [34].

tree at the redshift considered. Summing the contribution of each of these systems present at the redshift considered and repeating this procedure for every redshift step between $4 \leq z \leq 24$ allows us to obtain the global ionizing photon rate for each merger tree. Finally we just need to "weight" this result for the number density of DM halos with same mass at z=4; our final result will be the ionizing photon rate density. Just as an example the ionizing photon rate density obtained from the sample of merger trees already discussed is shown in Fig. (26). With this approach it is quite easy to disentagle between Pop.II and Pop.III contribution; in our simulation Pop.II stars are always dominant except for very high redshifts (z>23). As expected Pop.III contribution disappears at lower redshifts ($z < 12$) when the IGM is already chemical enriched. Notice that there is a non-negligible Pop.III contribution to the total ionizing photon rate density at moderate z ($12 \leq z \leq 15$). The very first peak in the ionizing photon production around $z \sim 24$ is due to star formation in molecular cooling minihalos, we will see that this feature has an important outcome to the global 21cm signal but this will be discussed later. A completely analogous plot is shown in Fig. (27) where molecular cooling halos are now "shutted down" (so we are considering SFR and accreting BHs only in DM halos with a mass larger than the mass corresponding to a virial temperature $T_{vir} \geq 10^4$). The first peak in the ionizing photon rate density is still present but now it is less extended in redshift and is only due to Pop.II stars (the Pop.III contribution is always subdominant). Finally notice that this result is given in cosmological units

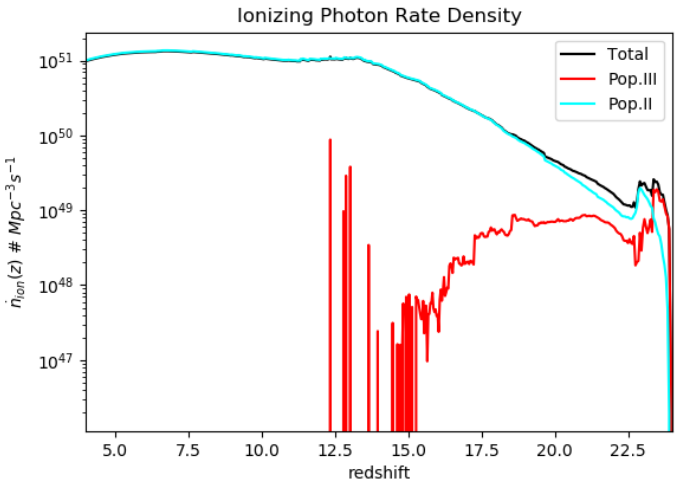

Figure 26: Ionizing photon rate density (number of photons $Mpc^{-3}s^{-1}$) vs z. Pop.II (cyan solid line), Pop.III (red solid line) and total (black solid line) contributions are shown.

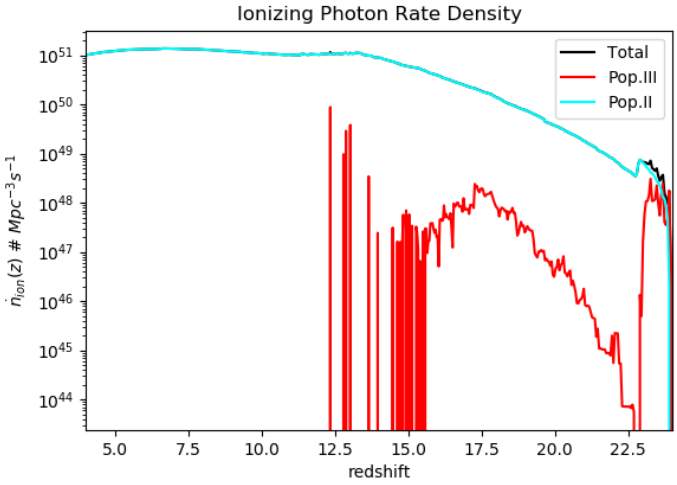

Figure 27: Same as Fig. (26) without molecular cooling halos.

M_{BH}	Eddington Ratio		
	0.01	0.1	1
$10^2 M_\odot$	47.28	47.76	48.15
$10^3 M_\odot$	48.70	49.28	49.77
$10^4 M_\odot$	50.01	50.70	51.29
$10^5 M_\odot$	51.20	51.97	52.62
$10^6 M_\odot$	52.28	53.12	53.83
$10^7 M_\odot$	53.22	54.13	54.89
$10^8 M_\odot$	54.00	54.92	55.69
$10^9 M_\odot$	54.76	55.68	56.45
$10^{10} M_\odot$	55.50	56.43	57.20

Table 1: Ionizing UV photon rate in logarithmic units for different BH masses in solar masses (values in the first column) and Eddington ratios (values in the first row). Taken from GQD in the version of Valiante et al. (2016b) [157]

(number of photons $Mpc^{-3}s^{-1}$) while in Eq. (106) we want $\dot{Q}_i$ in cgs units, so we need to do this conversion before using this result to evaluate the filling factor (and J_α).
Now we need to quantify the X-ray heating from stars. In this case we can still use the relation between L_X and SFR defined by Grimm et al. (2003) [63] (see Eq. (84)), so as before we need to compute the total SFR at each redshift. However, we are interested in the X-ray emissivity rather than in the X-ray luminosity. As already done also for the ionizing photon rate density, we have to weight each DM halo merger tree for the number density of DM halos at z=4, this will convert the SFR to a SFR density $\dot{\rho}_\star$. We can thus express ϵ_X as [22]:

$$\epsilon_X = 3.4 \times 10^{40} f_{Xh} \frac{\dot{\rho}_\star}{M_\odot yr^{-1} Mpc^{-3}} ergs^{-1} Mpc^{-3} \tag{109}$$

With this section we have shown that is quite easy to quantify the star contribution to the ionization and thermal history starting from CAT since we only need to have the SFR and metallicity of each star forming system at each redshift.

3.2.2 Black holes contribution

Now we move to a new contribution which was left out during analytical calculations: the one coming from the emission associated to BH accretion. In this case we need to import from CAT the BH accretion rate and mass. The ionizing photon rate density produced by accreting BHs can be estimated in a similar way of the stellar emission, Table (1) shows the $\log_{10}$ ionizing photon rate for BH masses between $10^2 M_\odot$ and $10^{10} M_\odot$ and Eddington ratios $\dot{M}_{Edd}$ between 0.01 and 1. The Eddington ratio r for each BH is defined from its accretion rate $\dot{M}_{accr}$ and mass M_{BH} as follows:

$$r = \frac{\dot{M}_{accr}}{\dot{M}_{Edd}} = \frac{\dot{M}_{accr}\epsilon_r c^2}{L_{Edd}} = \frac{\dot{M}_{accr}\epsilon_r c^2 \sigma_T}{4\pi c G M_{BH} m_p} = \frac{\dot{M}_{accr}}{2.2 \times 10^{-8} M_{BH}} \tag{110}$$

where the last equality considers a radiative efficiency $\epsilon_r = 0.1$. We remind that in the reference model of CAT the accretion is Eddington limited so the Eddington ratio r cannot be larger than unity. Using Table (1) and taking $\dot{M}_{accr}$ and M_{BH} from CAT for each galaxy hosting a nuclear active black hole we can easily obtain the ionizing photon rate density from BHs adopting the same procedure described for stars case only considering $\dot{M}_{accr}$ and M_{BH} in place of SFR and metallicity. Actually, with this calculation we are not considering that AGN may be (at least partially) obscured at the wavelengths of our interest. Neglecting AGN obscuration causes an overestimation of the total amount of ionizing photons. UV AGN obscuration has been extensively treated by Merloni et al. (2014) who studied the incidence of nuclear obscuration on a complete sample of 1310 AGN selected on the basis of their rest-frame 2–10 keV X-ray flux from the XMM-COSMOS survey, in the redshift range 0.3<z<3.5 (much recent epoch with respect to the one we are focusing on) [99]. They found that the obscured AGN fraction F_{obs} is fitted by the following formula:

$$F_{obs} = A + \frac{1}{\pi} \arctan\left(\frac{l_0 - l_X}{\sigma_X}\right) \tag{111}$$

where l_X is the logarithmic X-ray AGN luminosity in the 2-10 keV band. The other factors are parameters whose best-fit is: A=0.56, $l_0 = 43.89$ and $\sigma_X = 0.46$ [99]. This fitting formula has been found considering all redshifts bins, however F_{obs} can slightly change with redshift (we do not consider this small effect). In our treatment, we will consider that a fraction equal to $1 - F_{obs}$ of all AGN present is unobscured and so it will contribute to the total amount of ionizing photons while the remaining part, being obscured, will be neglected. Notice that this treatment is a bit simplified as F_{obs} corresponds to the obscuration fraction of a single AGN (so we should consider that all AGN are obscured of a fraction F_{obs} instead of taking a percentage F_{obs} of all AGN entirely obscured as we are doing). Moreover, we are extrapolating to high redshifts a relation which has been calibrated at much lower redshifts. In order to apply Eq. (111) we only need to estimate the total X-ray luminosity in the 2-10 keV band. This has been calculated applying a correction factor K_X to the bolometric luminosity of the AGN so that $L_{X,2-10keV} = K_X L_{BOL}$. We took the correction factor from Duras et al. (2020) [36]:

$$K_X(L_{BOL}) = a\left[1 + \left(\frac{\log(L_{BOL}/L_\odot)}{b}\right)^c\right] \tag{112}$$

where a=10.96, b=11.93, c=17.79. This relation is valid for both type 1 and type 2 AGN (the sampled analysed included $\sim$ 1000 type 1 and type 2 AGN) [36]. With this result we can compute the X-ray luminosity L_X that must be substituted inside Eq. (111) to obtain the UV obscuration fraction of AGNs. With this approach, we obtained the total ionizing photon rate from both BHs and stars shown in Fig. (28). The ionizing photon rate emitted by accreting BHs at z>18 is negligible due to the strong obscuration that these systems suffer (see the difference between the yellow and green lines in Fig. (28). At z < 17.5, the BH contribution to the ionizing photon rate increases but it is always subdominant with respect to the stellar contribution, making reionization mainly

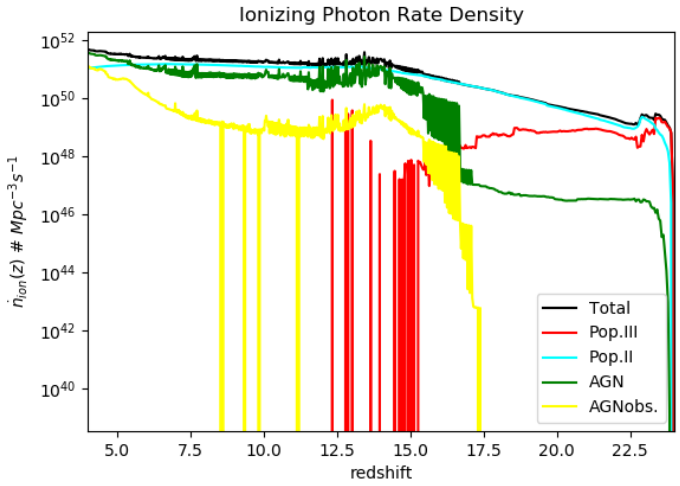

Figure 28: Ionizing photon rate density (number of photons $Mpc^{-3}s^{-1}$) vs z. Pop.II (cyan solid line), Pop.III (red solid line), total AGN (green solid line), AGN after correction for obscuration (yellow solid line) and total (black solid line) contributions are shown.

driven by stars except at the lowest redshifts. In the same spirit above, we have done also a second run in which we deleted the contribution of mini-halos (see Fig. (29)). We already seen that the Pop.III contribution at high-redshifts becomes negligible, however Fig. (29) clearly shows that the AGN contribution to the total ionizing UV photon rate does not change with respect to the first case when all halos are considered (yellow and green curves in the two plots are identical). AGNs produce also X-ray photons able to heat up the gas. The formalism adopted above to compute L_X from the bolometric luminosity is useful also to compute the X-ray emissivity. However, as we have already done for UV photons, we must consider that a certain amount of X-photons (probably smaller than the UV one since X-ray photons are more energetic) will not escape from the galaxy where they are produced: again we want to compute an obscuration factor in order to correct the X-ray luminosity that we observe. Our reference model for X-ray obscuration of AGNs is the one proposed by Ueda et al. (2014) [154]. In this work, the X-ray absorption correction is evaluated starting from one of the most complete and largest sample of AGNs between $0 \leq z \leq 5$ from surveys performed with Swift/BAT, MAXI, ASCA, XMM-Newton, Chandra, and ROSAT [154]. This correction is expressed in terms of the $\psi(L_X, z)$ parameter which represents the fraction of absorbed AGNs in total AGNs. It is expressed as a linear function of $\log L_X$ within a range $\psi_{min} = 0.2$ and $\psi_{max} = 0.84$:

$$\psi(L_X, z) = \min[\psi_{max}, \max[\psi_{43.75}(z) - \beta(\log L_X - 43.75), \psi_{min}]] \qquad (113)$$

where $\beta = 0.24$ and $\psi_{43.75}(z)$ represents the absorption fraction of AGNs with $\log L_X = 43.75$ located at z. Actually this redshift dependence disappears for $z \geq 2$ (which is our case) and $\psi_{43.75} = 3^{a_1}\psi^0_{43.75}$ with $a_1 = 0.48$ and $\psi^0_{43.75} = 0.43$. The total X-ray

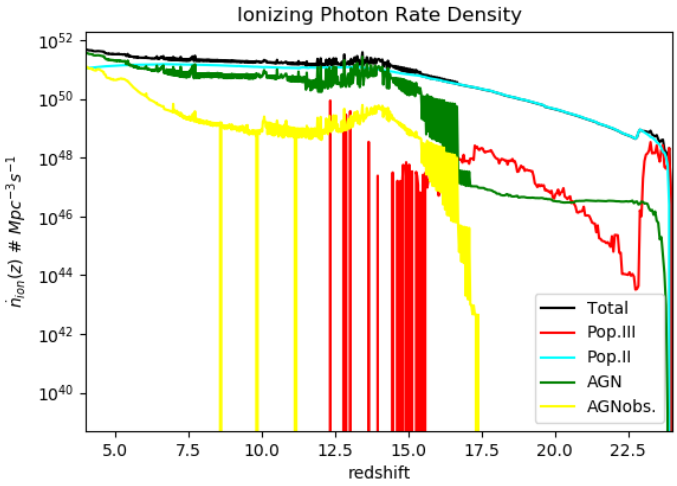

Figure 29: Same as Fig. (28) without molecular cooling halos.

luminosity from AGNs is simply $L_{X,unobs} = L_X(1 - \psi(L_X))$. With this final calculation, now we are able to compute each of the three backgrounds relevant for the 21cm signal either from stars or from BHs.

3.2.3 A radio background

So far, we focused on estimating three backgrounds from CAT: X-ray, UV ionizing and Lyman-α. However we will see that also the radio background may have an impact on the 21cm signal. The reason why this radio background can modify the shape of the 21cm signal will be discussed at the end of this section, for the moment we just focus on the physical motivation that may suggest that a strong radio diffuse background was present already at high redshifts ($z \geq 15$) [42] [97] and how to derive it starting from CAT outputs.

If we consider the first Pop.III star formation around $z \sim 30$, we may end up with a non-negligible accreting BH seeds population already at $z \sim 15 - 20$; such a population could be responsible for a continuous radio emission (which will impact on the shape of the 21cm global signal). This scenario has been widely studied in the literature (e.g. Haiman et al. (2004), Wilman et al. (2008), Ewall-Wice et al. (2014, 2018, 2019), Bolgar et al. (2018), Mebane et al. (2019) [67] [165] [41] [42] [43] [11] [97].) This radio emission at high-z can be motivated only if we assume that *(i)* a non-negligible fraction of BHs was present already at high-z, *(ii)* these BHs were accreting at least at an Eddington pace and *(iii)* these BHs had a radio-loudness similar to the one observed in AGN at present time. Following the formalism of Ewall-Wice et al. (2018) [42], to quantify this BH radio emission we start from a simple proportionality relation between the emissivity ϵ_ν and the BH density ρ_{BH}:

$$\epsilon_\nu(z) \propto f_{duty}(z) f_{edd}(z) \rho_{BH}(z) \tag{114}$$

where f_{edd} is the Eddington ratio and f_{duty} is the duty cycle. All these quantities are redshift-dependent since different studies suggest that both Eddington ratio and the duty cycle can have larger values going back in time (e.g. $f_{edd}(z \sim 0) \sim 10^{-2}$ while $f_{edd}(z \sim 4) \sim 0.3$ [136]). However, the redshift dependence of the Eddington ratio does not concern us as f_{edd} is provided by CAT. The radio luminosity is derived using the black hole fundamental plane relation found by Wang et al. (2006) between the radio luminosity, the soft X-ray (0.1-2.4keV) luminosity and the BH mass [163]:

$$\log\left(\frac{L_r}{10^{40} ergs^{-1}}\right) = \xi_{RX} \log\left(\frac{L_X}{10^{44} ergs^{-1}}\right) + \xi_{RM} \log\left(\frac{M}{10^8 M_\odot}\right) + k \tag{115}$$

where k, ξ_{RX} and ξ_{RM} are constants whose value is constrained by the best-fit to the observations. Moreover, to match the typical radio loudness found in SDSS/FIRST AGN by Ivezic et al. (2002) [75] we boost the luminosity of radio-loud quasars (which are approximately 10% of the total) by a factor $10^R = 10^3$. With this approximation, Eq. (114) becomes:

$$\epsilon(\nu, z) = 1.2 \times 10^{22} \left(\frac{f_L}{0.1}\right)\left(\frac{f_{duty}}{1}\right)\left(\frac{10^R}{10^3}\right)\left(\frac{f_X}{0.1}\right)^{0.86}\left(\frac{\rho_{BH}}{10^4 h^2 M_\odot Mpc^{-3}}\right)\left(\frac{\nu}{1.4GHz}\right)^{-0.6} \tag{116}$$

where f_L is the fraction of the radio-loud quasars and the result is given in W Hz^{-1} h^3 Mpc^{-3}. From CAT we can easily estimate ρ_{BH} and f_{Edd} from the BH mass, however all the other parameters are degenerate in our model. We will thus incorporate all these free parameters in a single one f_R that boosts the radio emissivity in a similar way done by Mebane et al. (2020) [97]:

$$\epsilon(\nu, z, f_R) = 1.2 \times 10^{22} \left(\frac{f_R}{1}\right)\left(\frac{\rho_{BH}}{10^4 h^2 M_\odot Mpc^{-3}}\right)\left(\frac{\nu}{1.4GHz}\right)^{-0.6} \tag{117}$$

From the radio emissivity we can compute the specific intensity of the radio background experienced by clouds of neutral hydrogen at redshift z $J_\nu(z, f_R)$ [97]:

$$J_\nu(z, f_R) = \frac{c}{4\pi}(1+z)^3 \int_z^\infty \frac{dz'}{(1+z')H(z')} \epsilon\left(\nu \frac{1+z'}{1+z}, z', f_R\right) \tag{118}$$

where, for our purposes, ν will always be the rest-frequency of the 21cm line (ν = 1420.41MHz). The final quantity we are interested in is the brightness temperature of this radio background at $\nu = 1420.41$MHz:

$$T_{rad}(z) = \frac{c^2 J_\nu(z, f_R)}{2\nu^2 k_B} \tag{119}$$

What emerges from this scenario is that, if we have a relatively large BH population at high-redshifts we can have a large radio background with a brightness temperature at the 21cm frequency given by Eq. (119). This would modify the shape of the 21cm signal since now we are not considering only the CMB as a background source but also this

new background. Instead of $T_R = T_\gamma$ in Eq. (96) we have to substitute $T_R = T_\gamma + T_{rad}$ making the ratio T_R/T_S larger. If this enhancement of the radio background occurs at moderately high-redshifts ($z \geq 15$), the absorption feature located at those redshifts would become much deeper due to the higher T_R/T_S ratio. The motivation that induced the scientific community to consider this additional background will be shown in Section 5.1

Now it is possible to appreciate how, starting from CAT simulations, we are able to obtain all the source-related quantities that are needed to estimate the 21cm signal. In this work, after having run simulations of 100 merger trees (10 for each mass bin considered), we have written some Python scripts that implemented the equations that have been discussed in this Section taking CAT outputs as input values. With this procedure, we first estimated the relevant backgrounds and then we obtained the ionization, thermal and 21cm signal evolution between $4 \leq z \leq 25$.

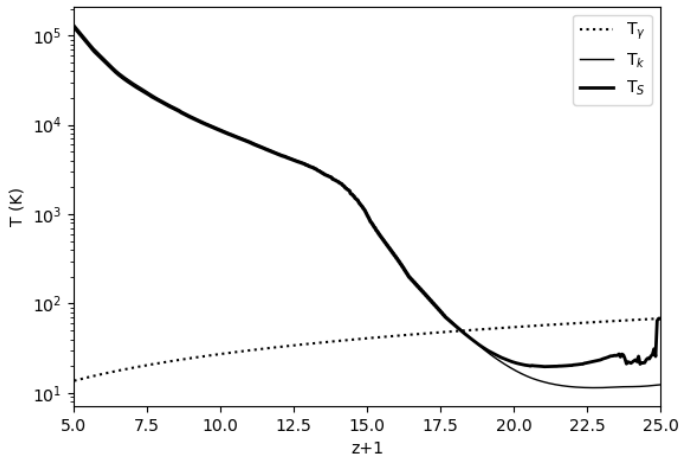

Figure 30: Redshift evolution of the spin temperature (thick line) and of the kinetic temperature (thin line) computed starting from CAT outputs. Dotted line shows the evolution of the CMB temperature ($\propto$ (1+z)).

4 Results

Hereafter we present the results of the 21cm signal generated with CAT outputs according to the procedure described in the previous section. The cosmology adopted is consistent with the latest measurements of Planck Collaboration et al. (2018) [111]: $\Omega_\Lambda = 0.685$, $\Omega_m = 0.315$, h=0.674, $\Omega_b = 0.05$ so that the age of the Universe at the final redshift z=4 is $t_H \sim 1.53$Gyr. We first provide the thermal and ionization histories in Fig. (30) and Fig. (31). The thermal history that we obtained starting from CAT outputs shows a global trend somehow similar to the one we computed in Section 2.3 with an analytical treatment according to the results obtained by Cohen et al. (2017) [29]. As already discussed throughout Section 2, in Fig. (30) we can see that at the beginning the IGM is cooling adiabatically, however, soon after the star formation begins (mainly Pop.III star formation), the kinetic temperature starts to increase ($z \sim 23.5$) thanks to the X-ray heating until it becomes hotter than the CMB photons ($z \sim 17$). The spin temperature instead, once the first structures are formed, is driven toward the kinetic temperature by the Lyman-α photons produced by the first stars until at $z \sim 18$ a tight coupling between T_K and T_S is reached (from this moment and for the entire redshift interval considered $T_K = T_S$). This global trend is shared by both the analytical calculation made in Section 2.3 and the semi-numerical computation described in Section 3.2. If, from one side it is true that the main physical processes that we are considering are basically the same (X-ray heating, Wouthuysen-Field effect which are both widely discussed in Sections 2.1 and 2.2), we have also to consider that the radiation produced by star formation and black hole accretion computed using CAT, accounts for more complex physical processes including the various feedback effects (according to the prescriptions discussed in Section

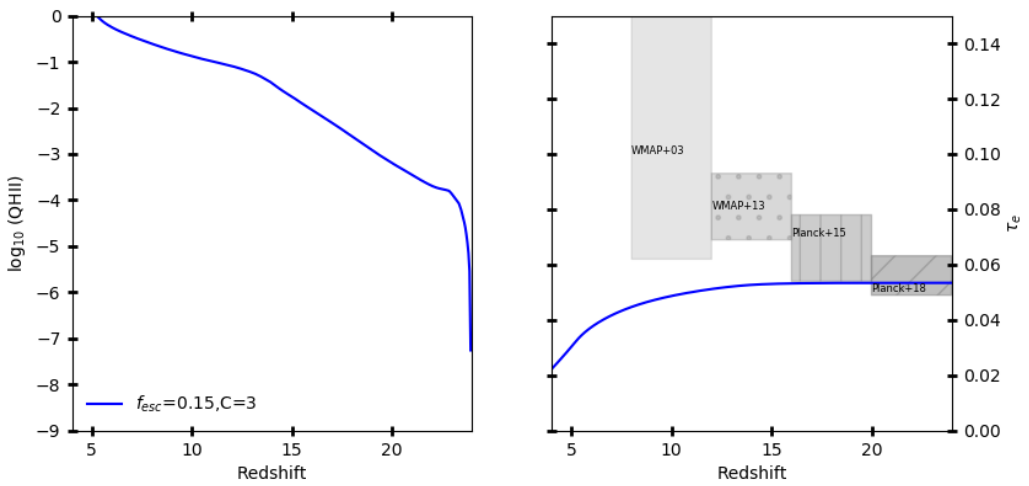

Figure 31: Ionization history and τ_e computed starting from CAT outputs and with $f_{esc} = 0.15$, C=3.

3.1.2). The increased complexity of the physics behind structure formation is reflected in a more complex evolution of the kinetic and spin temperature. For example, the spin temperature evolution shows an interesting feature at high-redshift where a rapid decrease of T_S is evident between $23.5 \leq z + 1 \leq 25$ (see Fig. (30)). The coupling between the spin and the kinetic temperature occurs quite soon ($z + 1 \sim 20$). CAT allows us to consider separately the various contribution of Pop.III, Pop.II stars and accreting BHs to the thermal evolution of the IGM. We show this in Fig. (32) where the contribution of Pop.III, Pop.II and accreting BHs is represented by red, cyan and yellow lines respectively. Pop.III stars are subdominant at heating up the gas. For $z + 1 \geq 17.5$ only Pop.II stars are responsible for the rising of the kinetic temperature of the IGM, while accreting BHs become important at intermediate and low redshifts (they are dominant between $10 \leq z + 1 \leq 16$). Fig. (31) shows that all the various sources are able to completely reionize the gas at $z \sim 5$ obtaining thus a value of the Thomson scattering optical depth ($\tau_e = 0.053$) perfectly consistent with Planck Collaboration et al. (2018) observations [111].
The 21cm signal with such ionization and thermal histories is shown in Fig. (33). The absorption feature is located at very high redshifts ($20 \leq z + 1 \leq 25$) reflecting the rapid and early decrease of the spin temperature. The transition from an absorption to an emission signal occurs at $z + 1 \sim 18.5$ when T_S becomes larger than the CMB photon temperature. The signal vanishes at $z+1 \sim 6$ when the hydrogen is completely ionized. In this plot we are using a logarithmic scale in the x-axis in order to show also the observed frequency of the signal (top x-axis). To better appreciate the 21cm absorption feature at high-redshift, Fig. (34) shows a zoom of Fig. (33) centered at $z \sim 20$ where the x-axis is now in a linear scale. From this figure it is evident that the absorption feature does

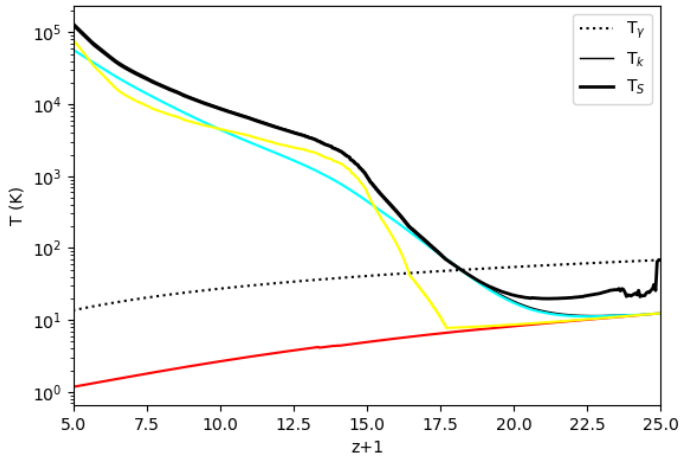

Figure 32: Same as Fig. (30) but separating the different contributions to the kinetic temperature evolution. Red, cyan and yellow lines refer to T_K if only Pop.III stars, Pop.II stars and accreting BHs are present.

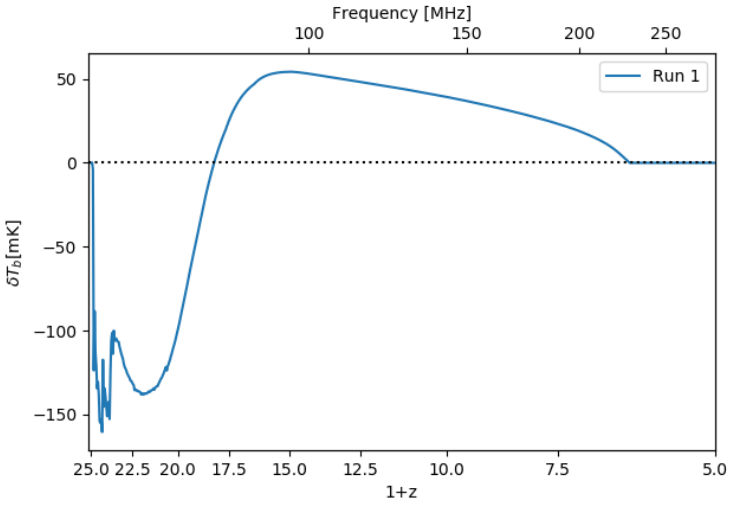

Figure 33: 21cm global signal starting from CAT outputs (see the text for details).

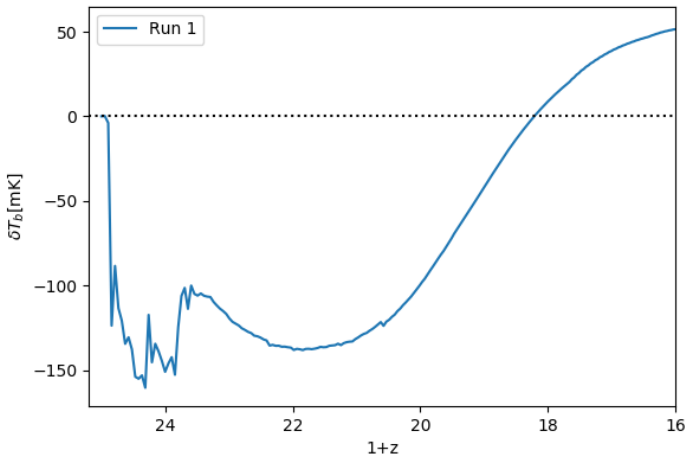

Figure 34: Same as Fig. (33) where the x-axis is now in a linear scale and the redshift interval considered is $16 \leq z + 1 \leq 25$.

not show a smooth profile showing a first stronger drop at a frequency corresponding to the signal at $z + 1 \sim 24$, then a sharp increase in the differential brightness temperature and finally a second drop which proceeds until a frequency corresponding to $z + 1 \sim 21$ when the signal starts to decrease its intensity (from now on we will refer to this feature as "two-peak absorption"). This is an interesting feature which has not been observed in the literature so far and that reflects the evolution of T_S in this redshift interval. It is worth noticing also that the signal is not continuous at these redshifts with many local rises and drops in the signal evolution. The possible causes and implications of this two-peak absorption feature will be extensively discussed in Section 5.

4.1 Removing mini-halos

The previous plots consider structure formation inside either molecular or atomic cooling halos following the prescriptions presented in Section 3.1.2 and 3.1.3. In this section we will produce analogous plots without the contribution of molecular cooling halos in order to see how the 21cm global signal changes. In practice, we now read from CAT outputs also the mass of each DM halo present in the merger tree and we restrict to sources hosted by dark matter halos with $T_{vir} > 10^4$ (computed by inverting Eq. (28)). It is important to stress, however, that this procedure is applied by post-processing CAT simulations output. Hence the evolution of Lyman-α cooling halos is still sensitive to physical processes occuring in their low mass progenitors, at higher redshift. The temperature evolution is shown in Fig. (35). When only Lyman-α cooling halos are considered, we still see the absorption feature, but the structure of the signal is different, with a less pronounced drop in the spin temperature. The ionization history instead is very similar to the one obtained when we consider the entire sample of halos (see Fig.

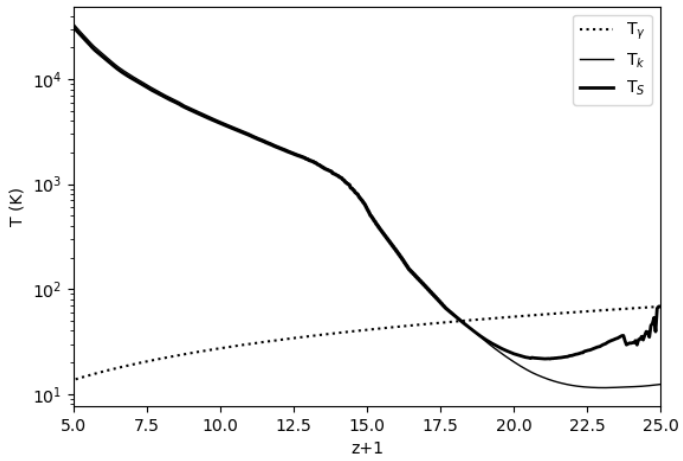

Figure 35: Same as Fig. (30) without considering the contribution of mini-halos.

(36) for a comparison); the only small difference is present at high-redshifts where the ionization proceeds a bit slower when we do not consider the contribution of mini-halos. This small difference does not affect the value of the Thomson scattering optical depth making also this second ionization history consistent with Planck measurements. The resulting 21cm signal, compared to the one previously obtained, and the corresponding zoom-in centered in the absorption feature are shown in Figs. (37) and (38). Also in this case the absorption feature of the 21cm global signal seems to show two peaks, however now these two peaks are less distinguishable since the rise between the two peaks is less pronounced (now the first peak is shallower than the second one). Moreover, compared to the previous result, the depth of the absorption feature is much lower in the first peak and only slightly lower in the second.

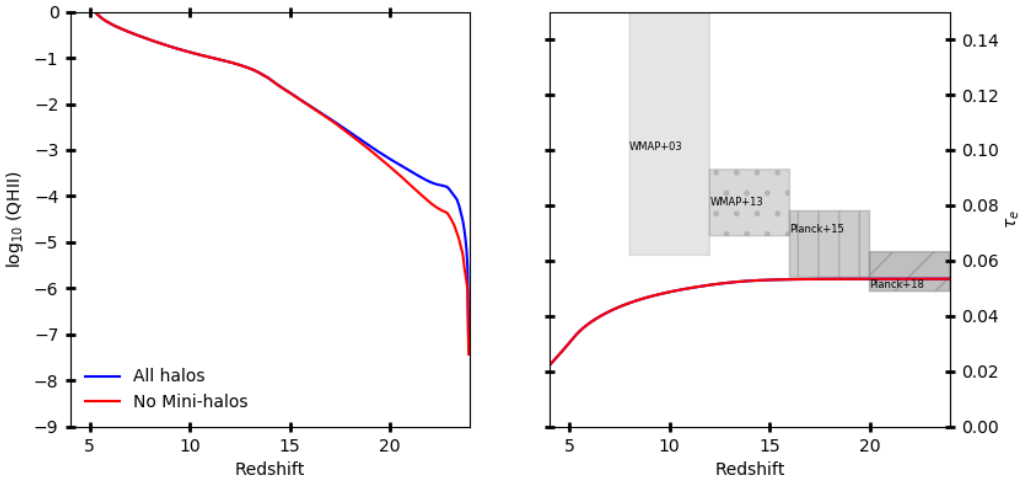

Figure 36: Same as Fig. (31) without considering the contribution of mini-halos (red solid line).

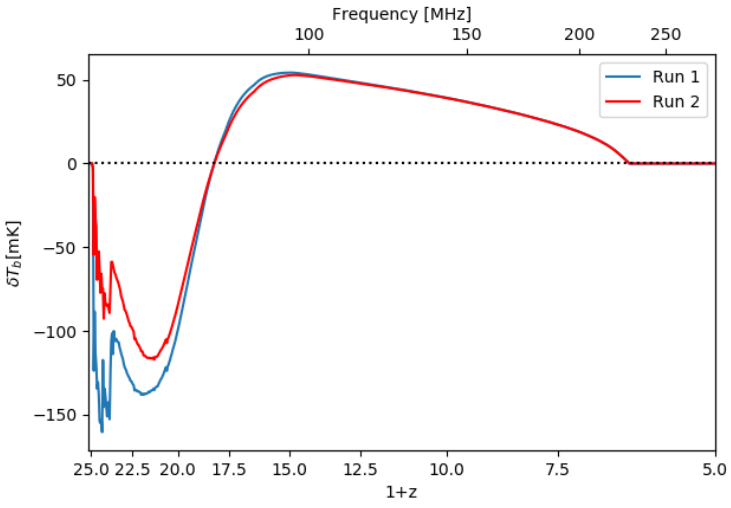

Figure 37: Same as Fig. (33) without considering the contribution of mini-halos (red solid line).

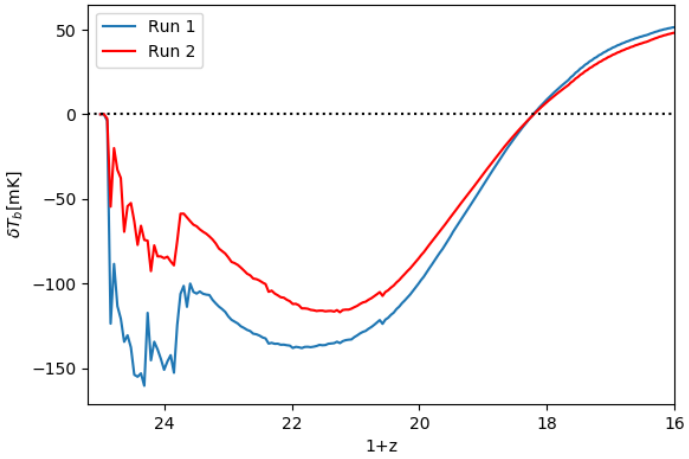

Figure 38: Same as Fig. (34) without considering the contribution of mini-halos (red solid line).

5 Discussion and future perspectives

The thermal history obtained in Fig. (30) suggests that a large amount of Lyman-α photons is produced already at high redshift, causing an early drop in the T_S evolution as a consequence of the tight coupling between the spin temperature and the kinetic temperature. This can better appreciated looking at Fig. (39) that plots the Lyman-α flux J_α (in units cm^{-2} s^{-1} Hz^{-1} sr^{-1}) as a function of redshift. J_α increases very rapidly already at high-z showing a peak between $23 \leq z \leq 24$. The same plot is done also when star formation inside mini-halos is neglected (Fig. (40)). The first peak is now shallower (decreases almost by an order of magnitude) indicating that the fast increase in J_α observed in Fig. (39) is mainly (but non completely) due to star formation inside mini-halos. It is worth to stress the fact that, even if when we remove the contribution of mini-halos, this first peak in the Lyman-α background at $z + 1 \sim 23$ is still present even if it is shallower.

The ionization history shown in Fig. (31) is consistent with the latest measurements of τ_e by the Planck Collaboration 2018 [111] and it shows two sharp rises: the first one at the beginning of the redshift interval considered which is mainly driven by stars, while the second one at lower redshift (z$\sim 6-8$) driven by AGNs. When we neglect the contribution of mini-halos we obtain a ionization history consistent with Planck measurements as well (there is only a negligible difference at high-redshifts); this suggests us that Pop.III star formation in mini-halos does not have a key role in the global reionization of the IGM.

Globally, the 21cm signal obtained in Fig. (33) is in broad agreement with the one computed in Section 2.3 (in particular if we look at the reference model computed following Cohen et al. (2017) [29] and shown in Fig. (13)). The two main differences are: *(i)* the

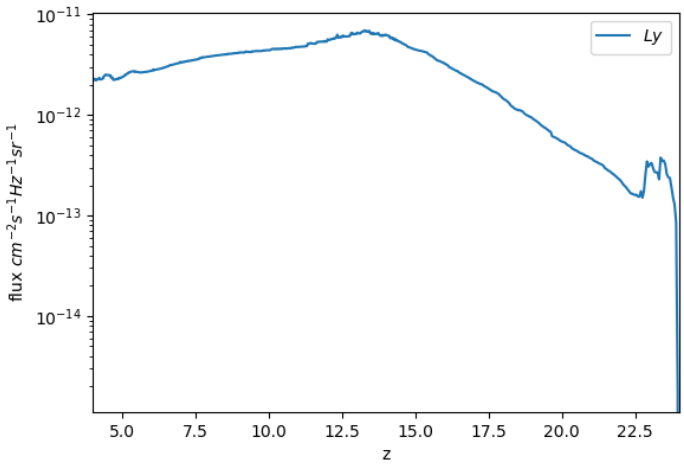

Figure 39: Lyman-α flux J_α computed from CAT (in units cm^{-2} s^{-1} Hz^{-1} sr^{-1}) vs z.

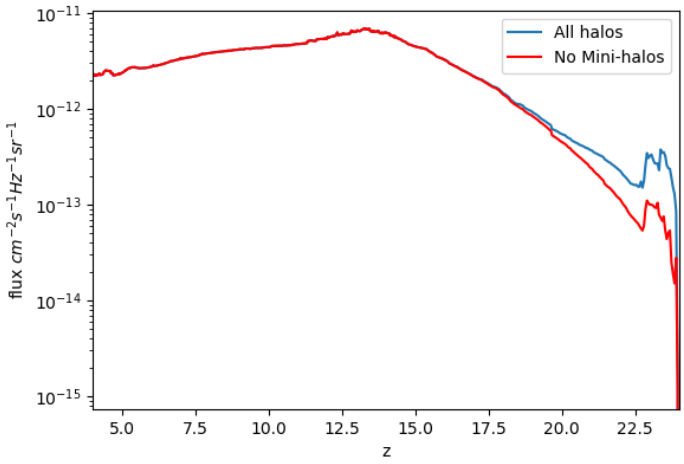

Figure 40: Same as Fig. (39) without considering the contribution of mini-halos (red solid line).

redshift evolution of the signal that now is slightly anticipated (the absorption feature is present already at z>20 and the signal starts to be seen in emission already at $z \sim 17$) and *(ii)* the shape of the absorption feature (two-peak absorption feature) located at $z \sim 23 - 19$. The anticipated redshift evolution of our 21cm global signal is driven by star formation in mini-halos. With respect to the models that consider star formation only inside atomic cooling halos we find that both the X-ray heating and the Lyman-α coupling start to be important at earlier epochs. This is shown also by Ewall-Wice et al. (2019) where different scenarios are considered [43]. The timing of our 21cm global signal is almost perfectly consistent with the "small halos scenario" (see figure 2 in [43]) that considers Pop.III star formation in molecular cooling halos. It is important to mention, however, that in our model we do not consider the effect of baryon-dark matter streaming velocities, which delay the onset of star formation inside mini-halos at very high redshift (see for instance Schauer et al. (2019) [127]). When the gas decoupled from radiation, it was streaming relative to the dark matter with a root-mean-square speed of $v_{bc} \simeq 10^{-4}c = 30\text{km s}^{-1}$). Since this relative velocity needs to be dissipated on virialization of the gas it prevents the baryons from settling into the DM potential wells during the growth of the halo [88]. Ultimately, this effect limits Pop.III star formation inside mini-halos (we have not enough baryons inside low-mass DM halos) shifting thus the absorption feature to lower redshifts.

If the timing of the 21cm global signal can be easily explained and there are some analogies with other works, the peculiar shape of the absorption feature that we obtained cannot been found in any other numerical or semi-numerical work aiming to compute the 21cm signal from the epoch of reionization (e.g. Cohen et al. (2017), Chatterjee et al. (2019), Ewall-Wice et al. (2020), Ahn & Shapiro (2021) [29] [22] [43] [3]). This double-peak in the absorption feature must be attributed to the rapid increase of the Lyman-α background followed by a small decrease and then a second and less rapid increase as shown in Fig. (39). This peculiar evolution in the Lyman-α flux (and thus in the spin temperature evolution) is driven by star formation (accreting BHs are subdominant at such high-z). The two-peak absorption feature may suggest that star formation occurred strongly and very rapidly at the beginning (probably in mini-halos) causing the first peak in the Lyman-α background and in the 21cm signal. Then, Pop.III and Pop.II stars formed during this first burst in star formation were responsible of various chemical, radiative and mechanical feedback effects that shut down star formation in molecular cooling halos, decreased the global SFR and caused a drop in the Lyman-α flux. Finally, the SFR proceeded almost at a constant pace in atomic cooling halos. In order to check this hypothesis we investigated the 21cm global signal computed when star formation in mini-halos is artificially removed (plots have been already described in Section 4.1). Contrary to what expected, the absorption feature of the 21cm global signal still shows two peaks. However, now these two peaks are less distinguishable since the rise between the two peaks is less important and the first peak is shallower than the second one. Moreover, with respect to the first signal, the depth of the absorption feature is much lower in the first peak and only slightly slower in the second peak. This is easily explained when we look at the difference in the evolution of the Lyman-α background (see Fig. (40))

in the two simulations. As shown also from the ionization history, the contribution of mini-halos is relevant only at the highest redshift (the first peak around $z+1 \sim 23$ is strongly affected) while between $19 \leq z+1 \leq 22$ the difference between the blue and red curves is way smaller. It is worth to stress the fact that, even if we have erased the contribution of mini-halos, the first peak in the Lyman-α flux (and in the absorption feature) is still present (even if shallower). This suggests that: *(i)* CAT predicts a non-negligible star formation in atomic cooling halos already at high-redshifts and *(ii)* the double-peak absorption feature cannot be addressed entirely to star formation in mini-halos. Since at very high redshifts the impact of accreting BHs is negligible compared to the one of stars, the sharp drop in the Lyman-α emission at $z \sim 23$ responsible for the double-peak absorption feature in the 21cm global signal, indicates that there must be a drop also in the star formation rate density as well as in the number density of ionizing photons (we remind that the Lyman-α background is computed starting from the UV ionizing background assuming an escape fraction $= 1 - f_{esc}$ as discussed in Section 3.2.1). This drop in the SFR density can be appreciated in the upper-left panel of Figs. (41), (42) and (43). In Fig. (41) we consider star formation also in mini-halos and we disentagle between the Pop.III contribution (halos with Z$<Z_{crit} = Z_{\odot}^{-3.8}$, red line) and Pop.II contribution (halos with Z$\geq Z_{crit} = Z_{\odot}^{-3.8}$, cyan line). In Fig. (42) we do not consider the contribution of mini-halos and still we disentangle between Pop.III/Pop.II contribution while in Fig. (43) we make a comparison between the two cases highlighting only the total contribution (with and without mini-halos, as shown by the solid and dashed lines, respectively). All these quantities are shown in the redshift range $17 \leq z \leq 24$ since we want to interpret the origin for the double-peak absorption feature found in the 21cm global signal emitted at these redshifts. Looking at the upper-left panel of Fig. (41), it is evident that the Pop.III contribution dominates over the Pop.II one only at the very beginning indicating that chemical feedback responsible for the metal enrichment of the IGM is extremely efficient. At $z \sim 23.5$ we can see a drop in the Pop.III contribution which almost does not affect the total SFR density indicating that some feedback process is turned on and self-regulates the amount of Pop.III stars. We marked this event with a green column. The second important feature in the global SFR density is the already mentioned drop at $z \sim 23$ determined by the drop of the Pop.II contribution which already dominates the total SFR density. This feature, marked with a light grey column, suggests that there should be some kind of mechanism (likely a feedback effect) that partially halts star formation. When we do not consider star formation inside mini-halos (see the upper-left panel of Fig. (42)), the contribution of Pop.III stars is much lower indicating that a dominant fraction of Pop.III stars is formed inside mini-halos. The total SFR density (again dominated by Pop.II stars) instead, is lower compared to the previous case (this can be better appreciated looking at the upper-left panel of Fig. (43)) telling us that also some Pop.II stars are formed inside mini-halos. The drop in the SFR density is still present even if it less pronounced. These trends in the star formation rate density of Pop.III and Pop.II stars show the importance of feedback in regulating star formation. When we disentangle between the Pop.III/Pop.II contribution, we observe that the drop in the SFR density occurs earlier for Pop.III stars. This is a consequence

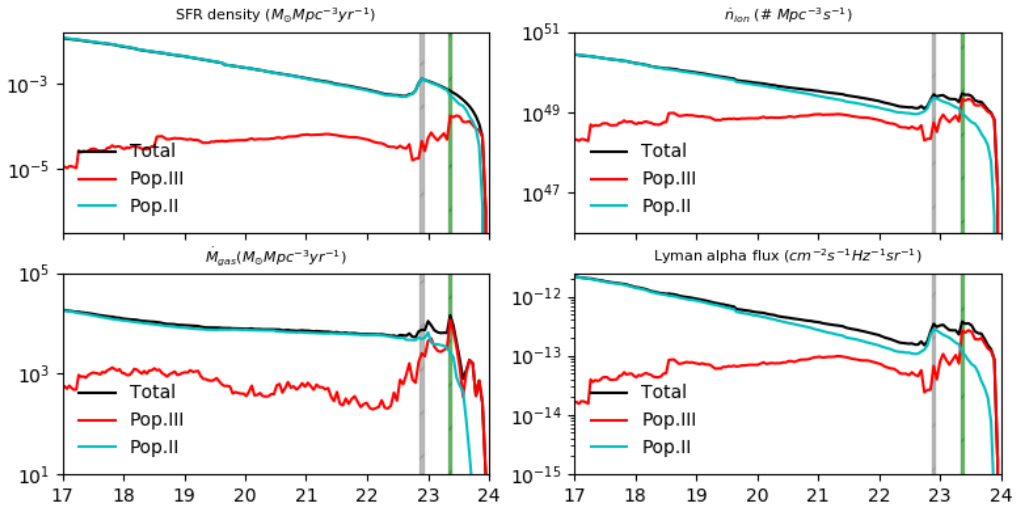

Figure 41: SFR density (upper-left panel) in $M_\odot \mathrm{Mpc}^{-3}\mathrm{yr}^{-1}$, number of UV photons emitted per unit time and volume ($\mathrm{Mpc}^{-3}s^{-1}$, upper-right panel), mass of gas ejected out of the galaxies in the IGM per unit time and volume ($M_\odot \mathrm{Mpc}^{-3}\mathrm{yr}^{-1}$, lower-left panel) and Lyman-α flux (lower-right panel) in $\mathrm{cm}^{-2}\mathrm{s}^{-1}\mathrm{Hz}^{-1}\mathrm{sr}^{-1}$ in the redshift interval $17 \leq z \leq 24$. For each panel we show the contribution coming from Pop.III and Pop.II star forming halos (red and cyan lines respectively) and the total trend (black line). The green and the light grey vertical lines mark the redshift where there is a sharp drop in the Pop.III and Pop.II SFR density respectively (see the text for details).

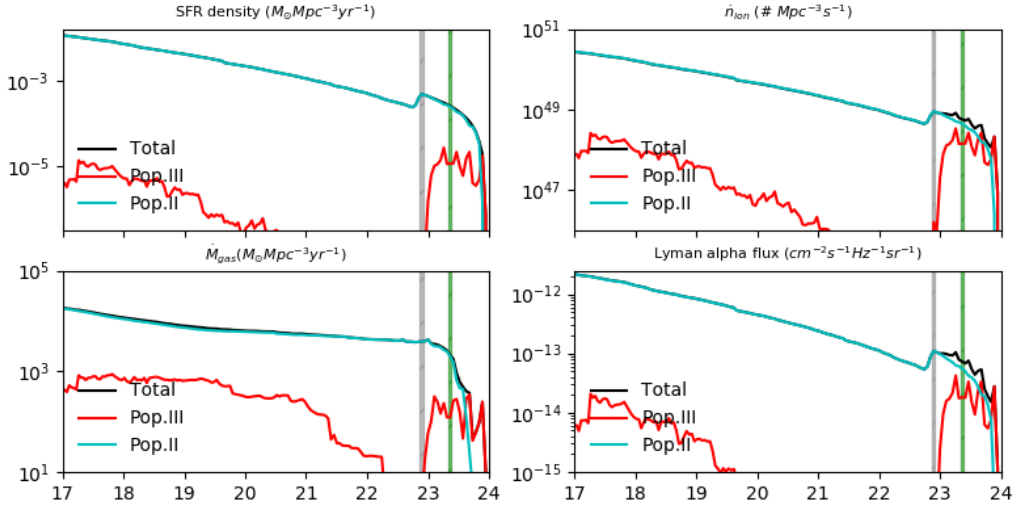

Figure 42: Same as Fig. (41) without considering the contribution of mini-halos

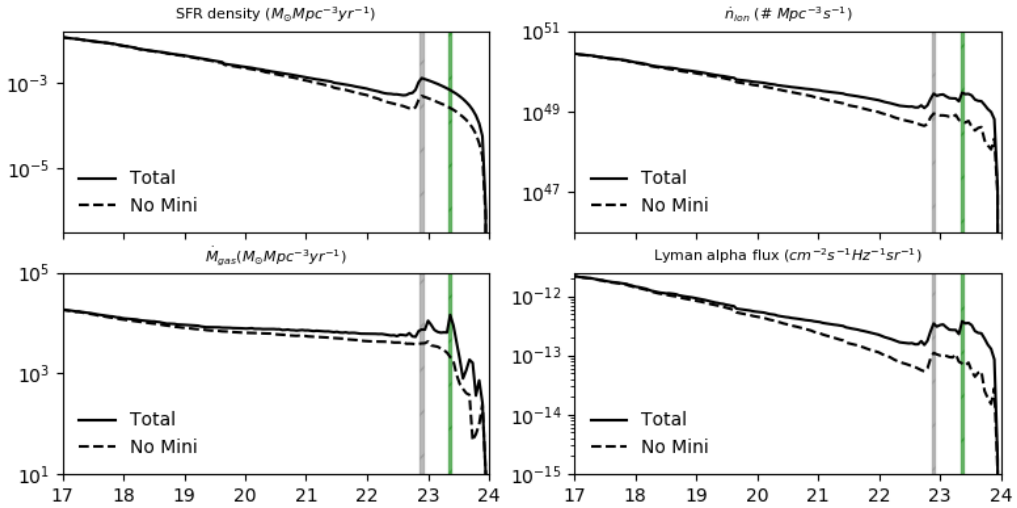

Figure 43: Same as Fig. (41) but comparing the results with (solid lines) and without (dashed lines) the contribution of mini-halos, independently of the nature of the stellar populations.

of the fact that Pop.III stars experience earlier mechanical feedback due to supernovae explosions (they have higher masses and thus shorter lifetimes) and they also experience a very efficient chemical feedback (many Pop.III stars explode as pair-instability supernovae which efficiently enrich the ISM with metals to super-critical metallicities, causing a rapid Pop III/Pop II transition in the stellar populations). Similarly, the drop in the Pop.II star formation rate density is probably due to mechanical feedback expelling gas inside Pop.II star forming systems and/or depleting gas from their Pop.III progenitors. The global trend of the SFR density determines the number density of UV ionizing photons $\dot{n}_{ion}$ and the Lyman-α flux J_α which are shown in the upper-right and lower-right panels of Figs. (41), (42) and (43). We already showed these quantities in Figs. (28) and (39) but now we can analyse these quantities in relation to the total SFR density described above. In particular, we can see that when we have the peak in the Pop.III star formation at the redshift marked by the green column, we obtain a peak also in the number density of UV ionizing photons as well as in the Lyman-α flux. Unlike the SFR density, in these two cases, the Pop.III peak is dominant with respect to the Pop.II contribution and thus it is visible even when we look at the total trend. Indeed, Pop.III stars have harder spectra and emit a larger fraction of ionizing photons compared to Pop.II stars. When mini-halos are not considered, the Pop.III peak is no longer visible since, as we have already seen, the Pop.III SFR density decreases significantly. In the lower-left panel of Figs. (41), (42) and (43) we show the mass of gas ejected per unit time and volume $\dot{M}_{gas}$ by both supernovae events and AGN winds (notice however that at these redshifts the latter contribution is subdominant, because the BH masses are still

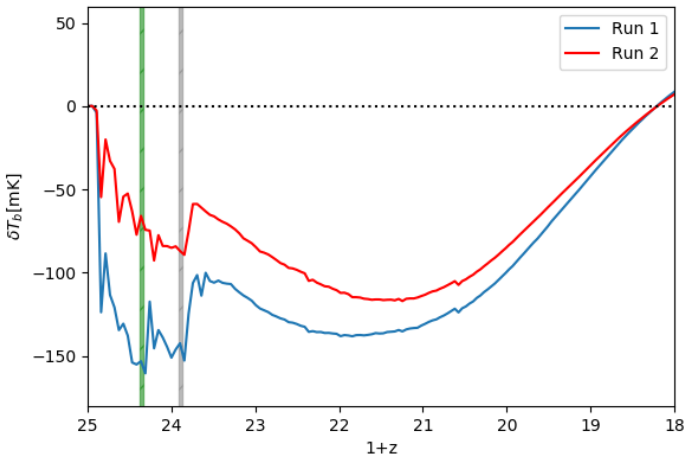

Figure 44: Same as Fig. (37) showing also the redshift step when a drop in Pop.III SFR density (green column) and in Pop.II SFR density (light grey column) occurred.

relatively small). When we consider all the halos present at each redshift we have a peak in the mass of ejected gas at the two marked redshifts. This supports the scenario in which the drop in the total SFR density is driven by mechanical feedback of effects due to supernova explosions. This process acts both on mini-halos and on Lyman-α cooling halos, explaining why the drop in the SFR density is present also when we do not consider mini-halos. It is worth noticing that the amount of gas ejected is larger when we consider the entire sample of halos since a large contribution comes from Pop.III stars which expel a large amount of matter when they explode as pair-instability supernovae. The Pop.II contribution instead begins later since Pop.II stars - due to their lower masses - are expected to explode at later times compared to Pop.III stars (Pop.II stars have masses distributed according to a Larson IMF with a characteristic mass much lower than the one taken for Pop.III stars so they have smaller masses and larger lifetimes). When the contribution of mini-halos is not considered (see Fig. (42)), Pop.III stars eject less gas while the contribution of Pop.II stars is still important and likely causes the drop in the SFR density at $z \sim 23$. We conclude this discussion showing the comparison of the two histories of the 21cm global signal obtained from CAT outputs, highlighting the two drop events in the SFR density described above. It is evident that, when structure formation is halted (or delayed), we will have a strong decrease in the production of Lyman-α photons. This leaves a signature in the 21cm global signal since, a weaker Lyman-α background ends up in a weaker coupling between the spin and kinetic temperature. If the gas is colder than the CMB, this causes a sharp rise in the differential brightness temperature. The 21cm global signal thus, not only provides information about structure formation but it can possibly put constraints on the type and strength of feedback mechanisms present in the high-redshift Universe.

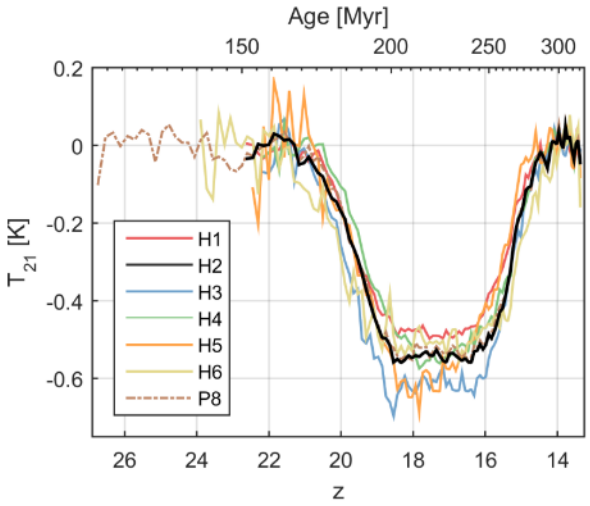

Figure 45: 21cm global signal detected by the EDGES collaboration: differential brightness temperature (in Kelvin degrees) vs z. Different solid lines refer to different fits of the signal (see Bowman et al. (2018) [15].)

5.1 The EDGES detection

Observing the 21cm global signal, is one of the most important purposes of many radio observational campaigns. However, so far there are no confirmed detections of this signal and only one potential observation claimed by Bowman et al. (2018) [15] (see Fig. 45). Before discussing this detection and the comparison with our results, it is important to stress the fact that there is no general consensus on this detection, as other authors (e.g. Hills et al. (2018) [70]) questioned the modeling of the foregrounds and thus, the truthfulness of this signal. The signal in Fig. (45) shows an absorption feature centered at 78MHz ($z \sim 17.2$), with a differential brightness temperature of 500mK and with a flat profile. The timing of this signal is shifted toward lower redshifts compared to the one that we obtained with CAT, it is instead more consistent with the analytical calculations done in Section 2 (see Fig. (13)). However, the timing is not a critical aspect of the EDGES detection (it is not difficult to theoretically justify the timing of the absorption feature advocating some of the physical processes that can prevent or delay star formation in mini-halos at high redshift (such as strong feedback and streaming velocities). The depth of the EDGES observation is instead much more difficult to explain: it is three times larger than the one predicted by CAT which is in accordance with many other works (e.g. Cohen et al. (2017), Chatterjee et al. (2019), Ahn & Shapiro (2021) [29] [22] [3]). This unexpected feature of the EDGES signal has been strongly debated by many authors (e.g. Jana et al. (2018), Kaurov et al. (2018), Hills et al. (2018), Ewall-Wice et al. (2018, 2019), Mirocha & Furlanetto (2019) [76] [82] [70] [42] [43] [102]) and all of them agree that there are two possible ways to interpret the large depth of this signal: *(i)* this detection is not a "real" detection being instead a result of a wrong

fitting procedure (e.g. incorrect model for the foreground emission) or *(ii)* there is some physical process relevant during Cosmic Dawn that we are missing out. Assuming that this is a "real" detection (so we are ruling out the first hypothesis) in order to measure such a large depth we need to have a much larger ratio T_γ/T_S in the Eq. (96) for the differential brightness temperature (if T_γ/T_S is very large, $1-(T_\gamma/T_S)$ would be large in absolute value and negative making δT_b large in absolute value and negative as well). Thus, the EDGES detection requires the gas to be colder than predicted by most of the models that we have discussed so far (so that, once Lyman-α coupling starts to be effective, T_S is driven at lower temperatures than predicted so far) or a radiation background larger than expected. Both these conditions are rather difficult to explain since we already accounted for the adiabatic cooling of the gas (so to make the gas colder we would need some other unknown physical process) and the temperature of the CMB is well known thanks to the many observations done in the past few decades. The first hypothesis made by Barkana (2018) [7] is to consider a new coolant of the gas: charged DM particles. Dark matter is the only constituent of the Universe which is colder than the early cosmic gas but at the same time we know that baryonic particles can interact with DM mainly through gravity. However, weak and non-gravitational interaction could be possible and if that is true they could be responsible for an extra cooling of the gas [7]. For this reason, the EDGES detection may open a new path to test new dark matter physics [7] [22] [51] [112] [140].
We now discuss the second possibility: having a stronger radiation background. Since assuming that the CMB is hotter is not justified by current tight observational constraints, the only way to fulfill this hypothesis is to assume that there is an additional radio background, stronger than the CMB (see the discussion at the end of Section 3.2.3) [46] [47]. This could be originated either by a population of early accreting BHs/mini-quasars originated by Pop.III stars [42] [43] [97] or by Pop.III supernovae explosions [76]. Since, as shown in Section 3.2.3, we can estimate the radio background produced by early accreting BHs starting from CAT outputs, hereafter we will show how our 21cm signal in Fig. (33) changes when this latter contribution is considered and how the strength of the signal compares to the depth observed by EDGES. We will use the formalism introduced in Section 3.2.3, in particular Eqs. (117), (118) and (119). We will consider this additional radio background only for the signal generated by all halos (both atomic and molecular cooling), in order to maximize the number of accreting BHs at high-redshifts which are formed as remnants of first stars inside mini-halos [42]. We start by computing the BH mass density predicted by CAT. The result given in $M_\odot/\mathrm{Mpc}^3$ is shown in Fig. (46). The flat profile at $z \geq 16$ reflects the population of light ($\simeq 100 M_\odot$) BH seeds which at high redshifts do not experience efficient gas accretion and significant mass growth. At intermediate redshifts ρ_{BH} strongly increases reaching $\sim 10^4 M_\odot$ Mpc^{-3} at $z \sim 13$. This result is highly consistent with the small-halo model found by Ewall-Wice et al. (2019) who estimated the BH population between $11 \leq z \leq 22$ with a very similar approach with respect to the one we have adopted (semi-analytical calculation, SF inside mini-halos). Starting from the BH mass density and artifically assuming that all the BHs are active (which is a strong overestimate of their real contribution, see below), we estimated the

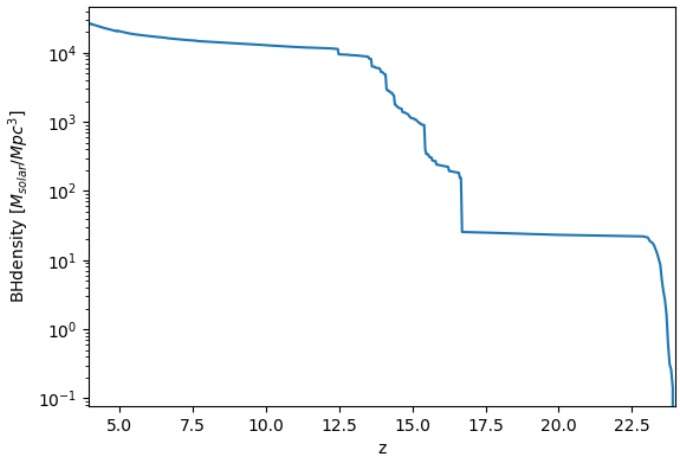

Figure 46: BH density (in $M_\odot/\mathrm{Mpc}^3$) evaluated from CAT outputs vs z. In the model, we consider both light and heavy BH seeds and their mass growth is estimated depending on the gas supply in the nuclear regions of their host galaxies (see section 3.2.2).

radio emissivity ϵ_ν, the specific intensity J_ν and the brightness temperature of the radio background T_{rad} at $\nu = 1420.41$MHz through Eqs. (117), (118) and (119). Results for J_ν and T_{rad} are shown in Figs. (47) and (48) where different values for the radio boost factor f_R are assumed. As expected, the larger is the boost factor, the larger will be also J_ν and T_{rad}; since f_R is just a multiplication factor, it does not change the shape of the curves. With these results we can easily compute the 21cm global signal, just by replacing T_γ with $T_{rad} + T_\gamma$. Results for different values of f_R are shown in Fig. (49). Looking only at the depth of the absorption feature around $z + 1 \sim 20$ we find that the value of f_R that better matches the EDGES detection is $f_R = 20$ (green solid curve). This value seems to be quite reasonable as $f_R \leq 50$ might be plausible [97]. However, now we end up with a second absorption feature of almost the same depth as the first one at moderate redshifts ($z + 1 \sim 12$). This is due to the fact that T_{rad} is very high ($\sim 10^5 K$) at those redshifts, even higher than the X-ray heated IGM. Such a strong radio background is the result of the fact that we assume all the BHs predicted by CAT to be actively accreting and hence to contribute to the radio background, when instead the emission is effectively coming only from BHs that are capable of accreting gas. For this reason, we now focus on $f_R = 20$ (the value that more correctly reproduces the depth of the EDGES absorption feature) and we will disentangle between BHs accreting at different paces (dividing the entire BH sample by their Eddington ratio). Fig. (50) shows ρ_{BH} computed starting from all BHs (cyan solid curve), BHs with an Eddington ratio larger than 0.01 (orange dashed curve) and BHs with an Eddingtion ratio larger than 0.1 (green dot-dashed curve). We remind that in our reference model of CAT, super-Eddington accretion is not allowed (so f_{edd} will always be smaller than unity). Orange and cyan curve

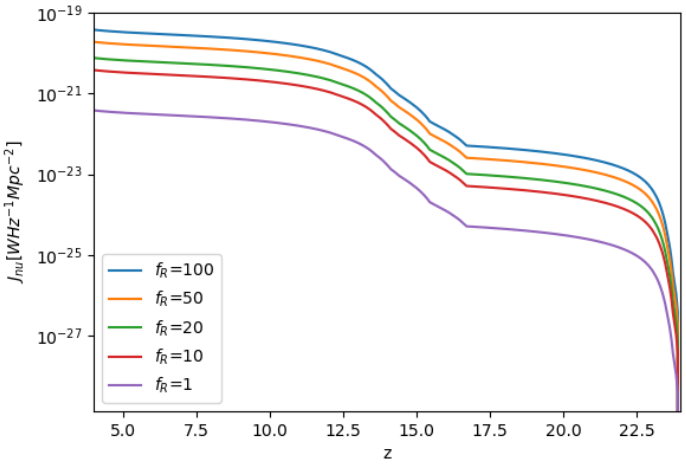

Figure 47: J_ν (in W Hz^{-1} Mpc^{-3}) vs z. Cyan, orange, green, red and purple solid lines refer to f_R =100, 50, 20, 10, 1 respectively (see text).

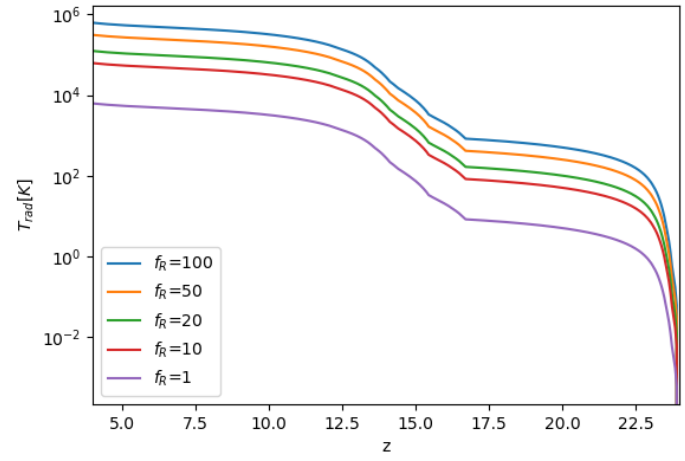

Figure 48: T_{rad} (in Kelvin degrees) vs z. Cyan, orange, green, red and purple solid lines refer to f_R =100, 50, 20, 10, 1 respectively (see text).

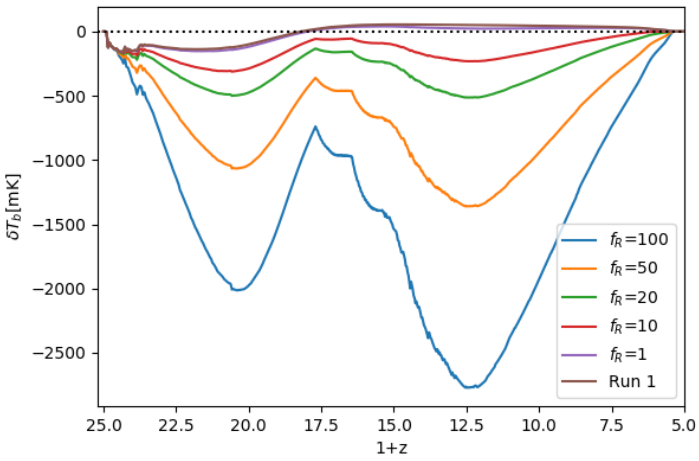

Figure 49: 21cm global signal once the radio background is incorporated (see the text for details). Cyan, orange, green, red and purple solid lines refer to f_R =100, 50, 20, 10, 1 respectively. Brown curve is the standard curve computed without taking into account the radio background.

are identical for $z \geq 16$ meaning that all BHs at those redshifts are accreting with an $f_{edd} \geq 0.01$. The main difference between orange and cyan curve is present at lower redshifts ($8 \leq z \leq 14$) when the orange curve is one order of magnitude below the cyan curve. Within this redshift interval, if we consider only accreting BHs instead of the entire sample as above, we expect to end up with a lower radio background. The green curve is lower than the orange already at high-z as this considers only strongly accreting BHs ($f_{edd} \geq 0.1$). These trends are present also in Figs. (51) and (52) where the specific radio intensity and the radio temperature of the background are shown.

Looking finally at the 21cm signals generated after these "cuts" (see Fig. (53)) we can see that, once we correctly account for only active BHs and we neglect the contribution of BHs that are not accreting, the second strong absorption feature at lower redshifts is no longer present even if -due to the reduced heating rate- the 21cm signal is always seen in absorption throughout reionization. With the more extreme cut at $f_{edd} \geq 0.1$ (green line), also the absorption feature at $z + 1 \sim 20$ is shallower, losing its agreement with EDGES observation. The less extreme cut at $f_{edd} \geq 0.01$ seems to be the most reasonable choice as it shows an absorption feature consistent with EDGES and the second absorption feature disappears at lower redshift. In general, when adding a radio contribution, the strength of the signal is given by the interplay between the X-ray heating and the evolution of the radio background temperature at $\lambda = 21.1cm$. Since accreting BHs are responsible both for ϵ_X and T_{rad}, in order to assess the importance of each background it is crucial to know both the X-ray obscuration of AGNs $\psi(L_X, z)$ and the fraction of the radio-loud quasars f_R. The values of these parameters have been already extensively discussed (see the Section 3.2.2 for K_X and above for f_R), however,

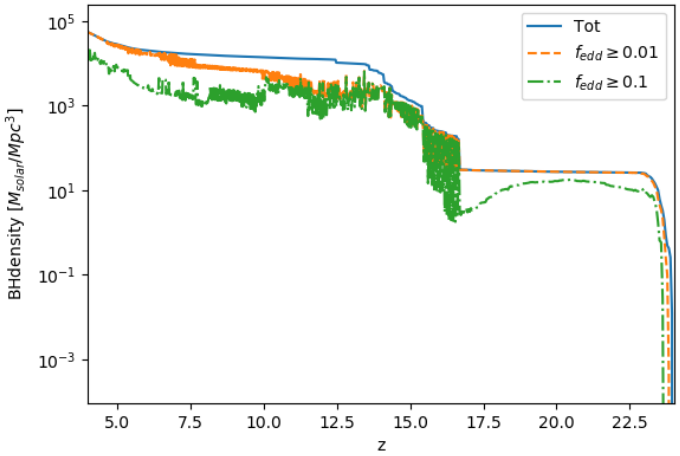

Figure 50: BH density (in $M_\odot/\text{Mpc}^3$) evaluated from CAT outputs vs z. Cyan solid curve considers all BHs, orange dashed and green dot-dashed represent BHs with an Eddington ratio f_{edd} larger than 0.01 and 0.1 respectively.

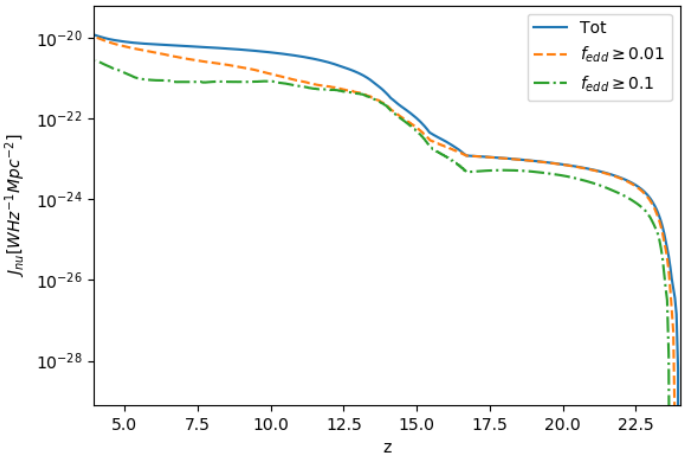

Figure 51: J_ν (in W Hz^{-1} Mpc^{-3}) vs z assuming $f_R = 20$. Cyan solid curve considers all BHs, orange dashed and green dot-dashed take BHs with an Eddington ratio f_{edd} larger than 0.01 and 0.1 respectively.

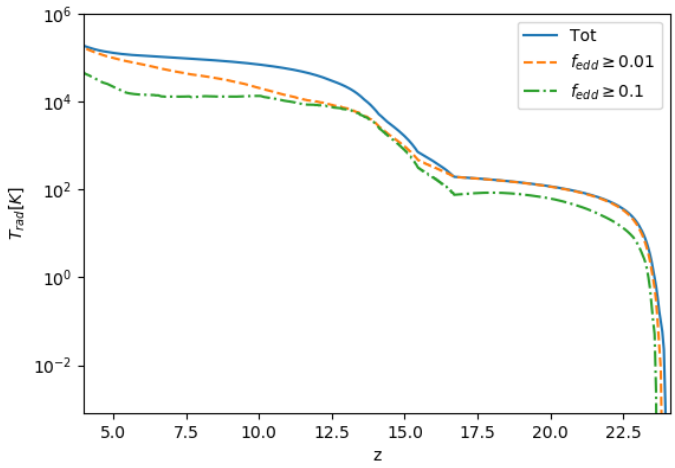

Figure 52: T_{rad} (in Kelvin degrees) vs z assuming $f_R = 20$. Cyan solid curve considers all BHs, orange dashed and green dot-dashed take BHs with an Eddington ratio f_{edd} larger than 0.01 and 0.1 respectively.

to put better constraints on them it will be very important to increase the statistics of high-redshift quasars. The results obtained so far are consistent with a recent work of Mebane et al. (2020) [97]. In that work their best-fit to EDGES was obtained with $f_R = 50$ ($f_R = 10$) without (with) considering X-ray obscuration of AGNs.

The most critical aspect of the EDGES detection is the flatness of the absorption profile. After having added the radio background, our model is still not consistent with the flat-absorption profile given by EDGES. Also other models in the literature that are able to explain the depth of the profile are not able to reproduce the flat-profile ([43] [97]). Among timing, depth and shape of the EDGES detection, the latter one is probably the most challenging to explain. Kaurov et al. (2018), focused only on this aspect (without worrying about the depth of the signal) and suggested that the shape of the EDGES signal can be explained if the bulk of UV photons are produced by rare and massive halos [82]. Pop.III stars formed in such halos, produce a large amount of Lyman-α photons that would lead to a rapid coupling between T_S and T_K. Then, the quick rise of the gas temperature would erase the signal. This explanation has been proposed also by Chatterjee et al. (2020) [23]. This scenario is somehow similar to the one we proposed in Section 5 in order to explain the "double-peak" profile shown in Fig. (33) with the two differences that: *(i)* we do not have a quick rise of the gas temperature and *(ii)* our "burst" of Pop.III star formation occurs mainly in the less-massive, molecular cooling halos.

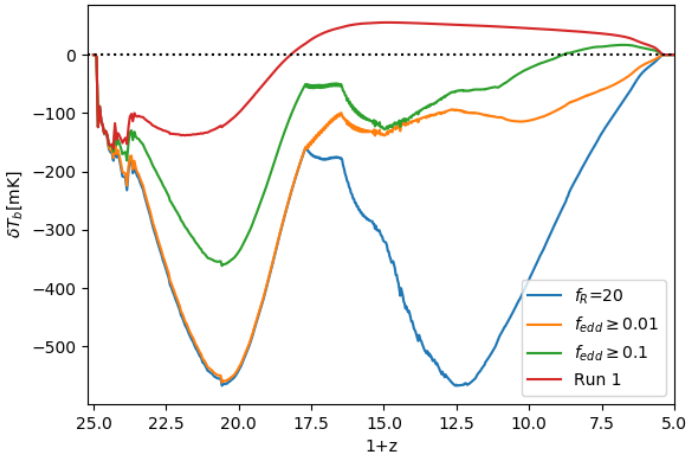

Figure 53: 21cm global signal once the radio background is incorporated (see the text for details) with $f_R = 20$. Cyan curve considers all BHs, orange and green take BHs with an Eddington ratio f_{edd} larger than 0.01 and 0.1 respectively. Red curve is the standard curve computed without taking into account the radio background.

5.2 Future Perspectives

During the past decade, a lot of work has been done in order to model (either with cosmological simulations or with semi-numerical calculations) the expected 21cm signal from Cosmic Dawn. The work presented in this thesis is based on these early studies but with a particular focus on the properties of Pop.III stars and early black hole accretion. While many models of the 21cm global signal from cosmic dawn have been proposed (especially in the last 5 years), observations are still missing. The work presented here confirms how rich is the physical information encoded in the 21cm global signal. Detections of the redshifted 21cm line will offer a new window onto the properties of the Universe during the epoch of reionization filling in a crucial gap in observations of the period where the first structures and stars had formed [115]. For this reason there are several ongoing and planned observational campaigns aiming to detect the 21cm signal from Cosmic Dawn. Except for the detection claimed by the EDGES collaboration (already discussed in the previous section), no experiment has observed such a signal so far. The most serious challenge is given by astrophysical foregrounds that bury the 21cm signal; their subtraction is based on the fact that these signals are expected to be spectrally smooth, unlike the true 21cm signal that should have a well defined structure in the frequency space. Among the current ongoing experiments it is worth to mention: LOFAR (Low Frequency Array), LWA (Long Wavelenght Array), MWA (Murchison Widefield Array) and PAPER (the Precision Array for Probing the Epoch of Reionization). The most interesting mission which is starting these days is HERA (The Hydrogen Epoch of Reionization Array) in the South African Karoo Radio Astronomy Reserve. Even if this radio telescope has

not observed any signal yet, recently it put some new and more sensitive constraints either on astrophysics or on the cosmology during the epoch of reionization (see HERA Collaboration (2021a) [69]). In particular HERA data has put constraints on the X-ray and radio background in the redshift interval $7.9 < z < 10.4$. This is only a first step, many others are expected in the coming years. Another crucial mission for the future is SKA (Square Kilometer Array). It is supposed to become operative by the late 2020s and it consists in two interferometers: SKA1-LOW in Australia whose focus is the 21cm cosmology and SKA1-MID in South Africa. To conclude this section it is worth to mention another very useful observational probe of the 21cm cosmology: the 21cm power spectrum. Even if the global 21cm signal provides us information about the mean evolution of the sources, we need to remember that each quantity fluctuates significantly [53]. For example, around galaxies the Lyman-α background and the X-ray heating will be stronger causing fluctuations in the 21cm signal. Many techniques have been developed in order to estimate the 21cm power spectrum (and higher-order statistics like the bispectrum) so that nowadays together with the estimation of the global signal many works provide also the power spectrum. Summarizing, the 21cm cosmology is now of primary scientific interest as demonstrated by the many observational campaigns in progress and planned.

6 Conclusions

Throughout this work, after having set the cosmological framework and having discussed the main physical processes that determine the shape of the 21cm global signal from Cosmic Dawn, we used the semi-numerical code CAT in order to compute the rate of structure formation and their properties between $4 \leq z \leq 24$ so that we were able to estimate the 21cm global signal arising from the emission of first stars and first BHs. We remind that the main effects we incorporated in the modeling of the global 21cm signal are: the X-ray heating from both stars (using the SFR-L_X relation from Grimm et al. (2003) [63]) and BHs (applying a correction factor K_X to the bolometric luminosity to be consistent with the work of Duras et al. (2020) [36]), the Lyman-α coupling and the various radiative/mechanical/chemical feedback effects responsible for shutting down (or delaying) star formation both inside molecular cooling halos and atomic cooling halos. We did not account for heating due to shocks and for dark matter-baryon streaming velocity responsible for an additional suppression of star formation. We find that:

- Ionization histories obtained from CAT are consistent with the latest Planck measurements assuming an escape fraction $f_{esc} = 0.15$ and a constant clumping factor C=3.
- The contribution of accreting BHs to the ionization and thermal histories is relevant at intermediate-low redshifts ($z \leq 16$) while at the early times these are entirely determined by Pop.III/Pop.II stars.
- If we consider all the star forming halos (including molecular cooling halos with a virial temperature $10^3 K \leq T_{vir} \leq 10^4 K$), the 21cm global signal shows a double-peak absorption feature. This particular shape never observed in the scientific literature, could be a consequence of our detailed modeling of chemical and mechanical feedback effects. In our scenario we have a burst of Pop.III star formation in mini-halos that quickly builds up a strong Lyman-α background that drives T_S toward T_K causing the first peak in the absorption feature. This is followed by a decrease in the SFR probably due to an interplay of chemical and mechanical feedback from Pop.III supernova effects. Finally there is a second increase in the SFR that causes a second rise in the production rate of Lyman-α photons and so the second peak in the absorption feature since the number of more massive atomic cooling halos progressively increases with time. The timing of the absorption feature found in this first run is anticipated with respect to many other semi-numerical calculation (e.g. Cohen et al. (2017), Chatterjee et al. (2019, 2020) [29] [22] [23]), it is however consistent with the "small halo scenario" in Ewall-Wice et al. (2019) [43].
- When we do not consider structure formation inside the less massive molecular cooling halos, the first peak in the Lyman-α and UV photon production becomes shallower (the contribution of Pop.III stars becomes negligible but still there is some non-negligible Pop.II star formation in atomic cooling halos already at high-redshifts) making the first peak in the absorption feature less deep. This could

suggest that the "double-peak" absorption feature found in the first run is caused by the contribution of mini-halos. If this is true, early star formation in mini-halos has an impact not only in the timing and in the depth of the absorption feature of the 21cm global signal, but also in its shape. However, since the first peak is not completely erased when star mini-halos are no more accounted for, another possibility is that this particular shape may be caused by the effect of gas depletion in mini-halos caused by Pop III SN explosions, that lead to a lower star formation efficiency in Lyman-α cooling halos where Pop.II stars form.

- We compared our 21cm global signal obtained considering all star forming halos with the EDGES detection reported by Bowman et al. (2018) [15]. With respect to this signal we found that the timing of our signal is anticipated (by $\Delta z \sim 3$, see Fig. (33) and (45)), the depth of our absorption feature is roughly three times smaller with a non-flat profile (we predict a rapid decrease of the differential brightness temperature with a more gentle rising). We attempted to reproduce the depth of the absorption feature considering an additional radio background produced by the emission of early accreting BH seeds (adopting the same formalism of Ewall-Wice et al. (2018) and Mebane et al. (2020) [42] [97]). We found that considering only BHs which are accreting with an Eddington ratio $f_{edd} \geq 0.01$ and a boost factor of the radio luminosity $f_L = 20$ we obtain the same differential brightness temperature of $\delta T_b = -500mK$. In this case the signal is always seen in absorption since the temperature of the radio background at $\lambda = 21.1$cm exceeds the kinetic temperature of the gas in the entire redshift interval considered. This result is consistent with what has been found by Mebane et al. (2020) [97].

References

[1] Abel, T., & Haiman, Z. (2000), to appear in H2 in Space, Paris, France, (1999), ed. F. Combes and Guillaume. Pineau des Forets.

[2] Abel, T., et al., The H II Region of a Primordial Star, (2007), ApJ, 659, L87

[3] Ahn, K. & Shapiro, P. R., Cosmic Reionization May Still Have Started Early and Ended Late: Confronting Early Onset with CMB Anisotropy and 21 cm Global Signals, (2021), ApJ, 914, 1.

[4] Allison, A. C. & Dalgarno, A., Spin Change in Collisions of Hydrogen Atoms, (1969), ApJ, 158, 423.

[5] Barkana, R. & Loeb, A., In the Beginning: The First Sources of Light and the Reionization of the Universe, (2001), Phys. Rep., 349, 125-238.

[6] Barkana, R. & Loeb A., Detecting the earliest galaxies through two new sources of 21cm fluctuations, (2005b), ApJ, 626, 1.

[7] Barkana, R., Possible interaction between baryons and dark-matter particles revealed by the first stars, (2018), Nature, 555, 71.

[8] Bernardeau, F. et al., Large-scale structure of the Universe and cosmological perturbation theory, (2002), Phys. Rep., 367, 1-248.

[9] Bianchi, S. et al., (2009), Astronomical Society of the Pacific Conference Series Vol. 414, Cosmic Dust - Near and Far. p. 65.

[10] Bland-Hawthorn, J., & Maloney, P.R., The Escape of Ionizing Photons from the Galaxy, (1999), ApJ, 510, 33.

[11] Bolgar, F. et al., Imprints of quasar duty cycle on the 21cm signal from the Epoch of Reionization, (2018), MNRAS, 478, 5564.

[12] Bondi, H., On spherically symmetrical accretion, (1952), MNRAS, 112, 195.

[13] Bouwens, R. J. et al., Lower-luminosity galaxies could reionize the universe: very steep faint-end slopes to the UV luminosity functions at $z \geq 5-8$ from the HUDF09 WFC3/IR observations, (2012), ApJ, 752, 1.

[14] Bouwens, R. J. et al., UV-continuum Slopes at z$\sim$ $4-7$ from the HUDF09+ERS+CANDELS Observations: Discovery of a Well-defined UV Color-Magnitude Relationship for $z \geq 4$ Star-forming Galaxies, (2014), ApJ, 754, 83.

[15] Bowman, J. D. et al., An absorption profile centred at 78 megahertz in the sky-averaged spectrum, (2018), Nature, 555, 67.

[16] Bromm, V., et al., Generic Spectrum and Ionization Efficiency of a Heavy Initial Mass Function for the First Stars, (2001), ApJ, 552, 464-472.

[17] Bromm, V. & Loeb, A., Formation of the First Supermassive Black Holes, (2003), ApJ, 596, 34.

[18] Bruzual, G. & Charlot S., Stellar population synthesis at the resolution of 2003, (2003), MNRAS, 344, 1000.

[19] Bryan, G. L., & Norman, M., Statistical Properties of X-Ray Clusters: Analytic and Numerical Comparisons, (1998), ApJ, 495, 80.

[20] Bullock, J. S., Kravtsov, A. V., & Weinberg, D. H., Reionization and abundance of galactic satellites, (2001), ApJ, 548, 33.

[21] Cen, R. & Ostriker J. P., Where are the baryons?, (1999), ApJ, 514, 1.

[22] Chatterjee, A., et al., Ruling out 3 keV warm dark matter using 21 cm-EDGES data, (2019), MNRAS, 487, 3560.

[23] Chatterjee, A. et al., A hint on the metal-free star formation rate density from 21cm-EDGES data, (2020), MNRAS, 496, 1445.

[24] Chen, X., Miralda-Escudé J., The Spin-Kinetic Temperature Coupling and the Heating Rate due to Lyman Alpha Scattering before Reionization: Predictions for 21cm Emission and Absorption, (2004), ApJ, 602, 1.

[25] Ciardi, B., Ferrara, A., & Abel, T., Intergalactic H2 Photodissociation and the Soft Ultraviolet Background Produced by Population III Objects, (2000), ApJ, 533, 594

[26] Ciardi, B. & Ferrara, A., The First Cosmic Structures and their Effects, (2005), Space Sci. Rev., 116, 625–705.

[27] Cole, S. et al., Hierarchical galaxy formation, (2000), MNRAS, 319, 168.

[28] Chuzhoy, L. & Shapiro, P. R., Heating and cooling of the intergalactic medium by resonance photons, (2007), ApJ, 655, 843.

[29] Cohen, A. et al., Charting the parameter space of the global 21-cm signal, (2017), MNRAS, 472, 1915.

[30] Davè, R. et al., Baryons in the Warm-Hot Intergalactic Medium, (2001), ApJ, 552, 473.

[31] Dayal, P. et al., Signatures of reionization on Lyα emitters, (2008), MNRAS, 389, 1683.

[32] Dayal, P. et al., The habitability of the Universe through 13 billion years of cosmic time, (2016), ApJ, 836, 16.

[33] de Bennassuti, M. et al., Decoding the stellar fossils of the dusty Milky Way progenitors, (2014), MNRAS, 445, 3039.

[34] de Bennassuti, M. et al., Limits on Pop III star formation with the most iron-poor stars, (2017), MNRAS, 465, 926.

[35] Duncan, K. et al., The mass evolution of the first galaxies: stellar mass functions and star formation rates at $4 < z < 7$ in the CANDELS GOODS-South field, (2014), MNRAS, 444, 2960.

[36] Duras, F. et al., Universal bolometric corrections for AGN over 7 luminosity decades, (2020), A&A, 636, A73.

[37] Eide, M. B. et al., Large scale simulations of H and He reionization and heating driven by stars and more energetic sources, (2020b), MNRAS, 498, 6083.

[38] Eisenstein, D. J. & Hu, W., Baryonic Features in the Matter Transfer Function, (1998), ApJ, 496, 605.

[39] Eisenstein, D. J. & Hu, W., Power Spectra for CDM and Variants, (1999), ApJ, 511, 5.

[40] Ellis, R. S. et al., The abundance of star-forming galaxies in the redshift range 8.5-12: new results from the 2012 Hubble ultra deep field campaign, (2013), ApJ, 763, 7.

[41] Ewall-Wice, A. et al., Detecting the 21-cm forest in the 21-cm power spectrum, (2014), MNRAS, 441, 2476.

[42] Ewall-Wice, A. et al., Modeling the radio background from the first black holes at cosmic dawn: implications for the 21cm absorption amplitude, (2018), ApJ, 868, 63.

[43] Ewall-Wice, A. et al., The Radio Scream from Black Holes at Cosmic Dawn: A Semi-Analytic Model for the Impact of Radio Loud Black-Holes on the 21 cm Global Signal, (2020), 492, 6086.

[44] Ewen, H. I., & Purcell, E. M., Observation of a Line in the Galactic Radio Spectrum: Radiation from Galactic Hydrogen at 1,420 Mc./sec., (1951), Nature, 168, 356.

[45] Fan, X. et al., Evolution of the Ionizing Background and the Epoch of Reionization from the Spectra of z 6 Quasars, (2002), AJ, 123, 1247.

[46] Feng, C. & Holder, G., Enhanced Global Signal of Neutral Hydrogen Due to Excess Radiation at Cosmic Dawn, (2018), ApJ, 858, 2.

[47] Fialkov, A & Barkana, R., Signature of Excess Radio Background in the 21-cm Global Signal and Power Spectrum, (2019), MNRAS, 486, 1763.

[48] Field, G. B., Excitation of the Hydrogen 21cm line, (1958), Proc. I. R. E., 46, 240.

[49] Field, G. B., The Time Relaxation of a Resonance-Line Profile, (1959a), ApJ, 129, 551.

[50] Field, G. B., An Attempt to Observe Neutral Hydrogen Between the Galaxies, (1959b), ApJ, 129, 525.

[51] Fraser, S. et al., The EDGES 21 cm anomaly and properties of dark matter, (2018), Physics Letters, 785, 159.

[52] Furlanetto, S. R. & A. Loeb, Large-scale structure shocks at low and high redshifts, (2004), ApJ, 611, 642–654.

[53] Furlanetto, S. R., Oh S. P., Briggs F. H., Cosmology at Low Frequencies: The 21 cm Transition and the High-Redshift Universe, (2006a), Phys. Rep., 433, 181.

[54] Furlanetto, S. R., The global 21-centimeter background from high redshifts, (2006b), MNRAS, 371, 867.

[55] Furlanetto, S. R., & Furlanetto, M. R., Spin-exchange rates in electron-hydrogen collisions, (2007a), MNRAS, 374, 547–555.

[56] Furlanetto, S. R., & Furlanetto, M. R., Spin exchange rates in proton-hydrogen collisions, (2007b), MNRAS, 379, 130–134.

[57] Giallongo, E., et al., A Low Upper Limit to the Lyman Continuum Emission of Two Galaxies at z∼3, (2002), ApJ, 568, L9-L12.

[58] Gnedin, N. Y., & Hui, L., Probing the Universe with the Lyalpha forest - I. Hydrodynamics of the low-density intergalactic medium, (1998), MNRAS, 296, 44

[59] Gnedin, N. Y., Effect of Reionization on Structure Formation in the Universe, (2000b), ApJ, 542, 535.

[60] Gonzalez, V. et al., Evolution of galaxy stellar mass functions, mass densities and mass-to-light ratios from $z \sim 7$ to $z \sim 4$, (2011), ApJ, 735, 34.

[61] Grazian, A. et al., The galaxy stellar mass function at $3.5 \leq z \leq 7.5$ in the CANDELS/UDS, GOODS-South, and HUDF fields, (2015), A&A, 575, 96.

[62] Graziani, L., Ciardi, B., & Glatzle, M., X-ray ionization of the intergalactic medium by quasars, (2018), MNRAS, 479, 4320.

[63] Grimm, H.-J., M. Gilfanov & R. Sunyaev, High-mass X-ray binaries as a star formation rate indicator in distant galaxies, (2003), MNRAS, 339, 793–809.

[64] Gunn, J. E., Peterson B. A., On the Density of Neutral Hydrogen in Intergalactic Space, (1965), ApJ, 142, 1633.

[65] Haiman, Z., Abel, T., & Rees, M. J., The Radiative Feedback of the First Cosmological Objects, (2000), ApJ, 534, 11.

[66] Haiman, Z. & Loeb, A., What Is the Highest Plausible Redshift of Luminous Quasars? (2001), ApJ, 552, 459.

[67] Haiman, Z. et al., Modeling the Counts of Faint Radio-Loud Quasars: Constraints on the Supermassive Black Hole Population and Predictions for High Redshift, (2004), ApJ, 612, 698.

[68] Heger, A. & Woosley S. E., The Nucleosynthetic Signature of Population III, (2002), ApJ, 567, 532.

[69] HERA collaboration, HERA Phase I Limits on the Cosmic 21-cm Signal: Constraints on Astrophysics and Cosmology During the Epoch of Reionization, (2021a), accepted to ApJ (in press.)

[70] Hills, R. et al., Concerns about Modelling of the EDGES Data, (2018), Nature, 564.

[71] Hirata, C. M., Wouthuysen–Field coupling strength and application to high-redshift 21-cm radiation, (2006), MNRAS, 367, 259.

[72] Hoyle, F., Lyttleton R. A., The effect of interstellar matter on climatic variation, (1939), Proceedings of the Cambridge Philosophical Society, 35, 405.

[73] Inayoshi, K. et al., The Assembly of the First Massive Black Holes, (2020), A&A, 58, 27.

[74] Inoue, A. K, et al., VLT narrow-band photometry in the Lyman continuum of two galaxies at z$\sim$3, (2005), A&A, 435, 471-482.

[75] Ivezic, Z. et al., Optical and Radio Properties of Extragalactic Sources Observed by the FIRST and SDSS Surveys, (2002), AJ, 124, 2364.

[76] Jana, R. et al., Radio background and IGM heating due to Pop III supernovae explosions, (2018), MNRAS, 483, 5329.

[77] Jeans, J. H., Astronomy and Cosmogony, (1928), (Cambridge: Cambridge University Press)

[78] Johnson, J. L. et al., The growth of the stellar seeds of supermassive black holes, (2012), ApJ, 750, 66.

[79] Johnson, J. L. et al., The First Billion Years project:the impact of stellar radiation on the co-evolution of Populations II and III, (2013), MNRAS, 428, 1857.

[80] Kamionkowski, D. N., et al., Small-Scale Cosmic Microwave Background Anisotropies as a Probe of the Geometry of the Universe, (1994), ApJ, 426, L57.

[81] Kang, H. et al., Shock waves in the large-scale structure of the Universe, (2005), ApJ, 620, 21–30.

[82] Kaurov, A. A. et al., Implication of the Shape of the EDGES Signal for the 21 cm Power Spectrum, (2018), ApJL, 864, L15.

[83] Kolb, E. W., & Turner, M. S. (1990), The Early Universe (Redwood City, CA: Addison-Wesley)

[84] Kuhlen, M., Madau P. & Montgomery R., The spin temperature and 21cm brightness of the intergalactic medium in the pre-reionization era, (2006), ApJ, 637, L1.

[85] Labbè, I. et al., The spectral energy distributions of $z \sim 8$ galaxies from the IRAC ultra deep fields: emission lines, stellar masses and specific star formatin rates at 650 Myr, (2013), ApJ, 777, 19.

[86] Larson, R. B., Early star formation and the evolution of the stellar initial mass function in galaxies, (1998), MNRAS, 301, 569.

[87] Leitherer, C., et al., Starburst99: Synthesis Models for Galaxies with Active Star Formation, (1999), ApJS, 123, 3.

[88] Loeb, A. & Furlanetto, S.R., The First Galaxies in the Universe, (2013), (Princeton, NJ: Princeton University Press).

[89] Ma, QB. et al, Investigating X-ray sources during the epoch of reionization with the 21 cm signal, (2021), ApJ, 912, 143.

[90] Machacek M. M., Bryan G. L., & Abel T., Simulations of Pregalactic Structure Formation with Radiative Feedback, (2001), ApJ, 548, 509.

[91] Madau, P. & Shull, J. M., Cosmic Metal Production and the Contribution of QSO Absorption Systems to the Ionizing Background, (1996), ApJ, 457, 551

[92] Madau, P. et al., 21-CM Tomography of the Intergalactic Medium at high redshift, (1997), ApJ, 475, 429.

[93] Madau, P., (1999), in AIP Conf. Proc. 470, After the Dark Ages: When Galaxies were Young, Eds. S. S. Holt & E. P. Smith (Woodbury: AIP), 299.

[94] Madau, P. & Rees, M. J., Massive Black Holes as Population III Remnants, (2001), ApJ, 551, L27.

[95] Madau, P. & Dickinson, M., Cosmic star formation history, (2014), ARA&A, 52, 415.

[96] Madau, P. & Fragos, T., Radiation backgrounds at cosmic dawn: X-rays from compact binaries, (2017), ApJ, 840, 39.

[97] Mebane, R. H. et al., The effects of population III radiation backgrounds on the cosmological 21-cm signal, (2020), MNRAS, 493, 1217.

[98] Mellema, G., et al., Simulating cosmic reionization at large scales – II. The 21-cm emission features and statistical signals, (2006), MNRAS, 372, 679.

[99] Merloni, A. et al., The incidence of obscuration in active galactic nuclei, (2014), MNRAS, 437, 3550.

[100] Miniati, F. et al., Properties of Cosmic Shock Waves in Large-Scale Structure Formation, (2000), ApJ, 542, 608-621.

[101] Miralda-Escudé, J. et al., Reionization of the Inhomogeneous Universe, (2000), ApJ, 530, 1.

[102] Mirocha, J. & Furlanetto, S. R., What does the first highly-redshifted 21-cm detection tell us about early galaxies? (2019), MNRAS, 483, 1980.

[103] Mori, M., et al., Early Metal Enrichment by Pregalactic Outflows. II. Three-dimensional Simulations of Blow-Away, (2002), ApJ, 571, 40.

[104] Navarro, J. F., Frenk, C., & White, S. D. M., A Universal Density Profile from Hierarchical Clustering, (1997), ApJ, 490, 493.

[105] Navarro, J. F., et al., The diversity and similarity of simulated cold dark matter haloes, (2010), MNRAS, 402, 21

[106] Nishi, R., & Tashiro M., Self-Regulation of Star Formation in Low-Metallicity Clouds, (2000), ApJ, 537, 50

[107] Oesch, P. A. et al., The Most Luminous $z \sim 9-10$ Galaxy Candidates Yet Found: The Luminosity Function, Cosmic Star-formation Rate, and the First Mass Density Estimate at 500 Myr, (2014), ApJ, 786, 108.

[108] Parkinson, H. et al., Generating Dark Matter Halo Merger Trees, (2008), MNRAS, 383, 557.

[109] Peebles, P.J.E., The Large-scale Structure of the Universe, (1980), (Princeton, NJ: Princeton University Press).

[110] Planck Collaboration XIII, Planck2015 results. XIII. Cosmological parameters., (2016), A&A, 594, A13,

[111] Planck Collaboration VI, Planck2018 results. VI. Cosmological parameters., (2020), A&A, 641, A6.

[112] Pospelov, M. et al., Room for New Physics in the Rayleigh-Jeans Tail of the Cosmic Microwave Background, (2018), Phys. Rev. Lett., 121, 031103.

[113] Press, W. H., & Schechter, P., Formation of Galaxies and Clusters of Galaxies by Self-Similar Gravitational Condensation, (1974), ApJ, 187, 425.

[114] Pritchard, J. R., & Furlanetto, S. R., Descending from on high: Lyman-series cascades and spin-kinetic temperature coupling in the 21-cm line, (2006), MNRAS, 367, 1057.

[115] Pritchard, J. R., & Loeb A., 21-cm cosmology in the 21st Century, (2012), Reports on Progress in Physics, 75, 086901

[116] Raiteri, C. et al., (1996), Memorie della Società astronomica italiana, 67, 817.

[117] Ricotti, M., et al., Feedback from Galaxy Formation: Production and Photodissociation of Primordial H2, (2001), ApJ, 560, 580.

[118] Rybicki, G. B., Improved Fokker-Planck Equation for Resonance-Line Scattering, (2006), ApJ, 647, 709–718.

[119] Sahni, V. & Coles, P., Approximation methods for non-linear gravitational clustering, (1995), Phys. Rep., 262, 1-135.

[120] Sakurai, Y. et al., Hyper-Eddington mass accretion on to a black hole with super-Eddington luminosity, (2016a), MNRAS, 461, 4496.

[121] Salvaterra, R., et al., Induced Formation of Primordial Low-Mass Stars, (2003), NewA, 10, 113.

[122] Sarmento R. et al., Following the cosmic evolution of pristine gas. ii. the search for pop iii-bright galaxies, (2018), ApJ, 854, 75.

[123] Sassano, F. et al., Light, medium-weight or heavy? The nature of the first supermassive black hole seeds, (2021), MNRAS, 506, 613.

[124] Scalo, J., (1998), in ASP conference series Vol 142, The Stellar Initial Mass Function, eds. G. Gilmore & D. Howell, p. 201 (San Francisco: ASP)

[125] Scannapieco E., Schneider R., & Ferrara A., The Detectability of First Stars, (2003), ApJ, 589, 35.

[126] Schaerer D., On the properties of massive Population III stars and metal-free stellar populations, (2002), A&A, 382, 28.

[127] Schauer, A. T. P. et al., Constraining First Star Formation with 21 cm Cosmology, (2019a), ApJL, 877, L5.

[128] Schaye, J. et al., The EAGLE project: simulating the evolution and assembly of galaxies and their environments, (2015), MNRAS, 446, 521.

[129] Schenker, M. A. et al., Contamination of broadband photometry by nebular emission in high-redshift galaxies: investigations with Keck's mosfire near-infrared spectrograph, (2013), ApJ, 777, 67.

[130] Schneider, R., et al., First stars, very massive black holes and metals, (2002), ApJ, 571, 30.

[131] Schneider, R., et al., Low-mass relics of early star formation, (2003), Nature, 422, 869.

[132] Schneider, R., et al., Constraints on the IMF of the first stars, (2005), MNRAS, 369, 825-834.

[133] Seager, S., Sasselov, D. D., & Scott, D., A new calculation of the recombination epoch, (1999), ApJ, L523.

[134] Shapiro, P. R. & Giroux, M. L., Cosmological HII Regions and the Photoionization of the Intergalactic Medium, (1987), ApJ, 321, 107.

[135] Shen, R.-F., A Catalog of Quasar Properties from Sloan Digital Sky Survey Data Release 7, (2011), ApJS, 194, 45.

[136] Shen, R.-F. & Kelly, B. C., The demographics of broad-line quasars in the mass-luminosity plane. I. Testing FWHM-based virial black hole masses, (2012), ApJ, 746, 169.

[137] Sheth, R. K., & Tormen, G., An excursion set model of hierarchical clustering: ellipsoidal collapse and the moving barrier, (2002), MNRAS, 329, 61.

[138] Short, C.J., & Coles, P., Gravitational instability via the Schrodinger equation, (2006), Journal of Cosm. and Astrop. Phys., 12, 012

[139] Shull, J. M., & van Steenberg M. E., X-ray secondary heating and ionization in quasar emission-line clouds, (1985), ApJ, 298, 268.

[140] Slatyer, T. R & Wu, C., Early-Universe Constraints on Dark Matter-Baryon Scattering and their Implications for a Global 21cm Signal, (2018), Phys. Rev. D, 98, 023013.

[141] Song, M. et al., The Evolution of the Galaxy Stellar Mass Function at $z = 4 - 8$: A Steepening Low-mass-end Slope with Increasing Redshift, (2016), ApJ, 825, 5.

[142] Spergel, D. N., et al., First-Year Wilkinson Microwave Anisotropy Probe (WMAP) Observations: Determination of Cosmological Parameters, (2003), ApJS, 148, 175.

[143] Springel, V. et al., Simulations of the formation, evolution and clustering of galaxies and quasars, (2005), Nature, 435, 629.

[144] Stark, D. P. et al., Keck spectroscopy of $3 < z < 7$ faint Lyman break galaxies: the importance of nebular emission in understanding the specific star formation rate and stellar mass density, (2013), ApJ, 763, 129.

[145] Stetcher, T. P., & Williams, D. A., Photodestruction of Hydrogen Molecules in H I Regions, (1967), ApJ, 149, 29.

[146] Strömgren, B., The Physical State of Interstellar Hydrogen, (1939), ApJ, 89, 526.

[147] Sugimura, K. et al., Stunted accretion growth of black holes by combined effect of the flow angular momentum and radiation feedback, (2018), MNRAS, 478, 3961.

[148] Susa, H., & Kitayama T., Collapse of low-mass clouds in the presence of a UV radiation field, (2000), MNRAS, 317, 175.

[149] Susa, H., & Umemura M., Secondary Star Formation in a Population III Object, (2006), ApJ, 645, 93

[150] Takeo, E. et al., Rapid growth of black holes accompanied with hot or warm outflows exposed to anisotropic super-Eddington radiation, (2018), MNRAS, 476, 673.

[151] Tegmark, M., et al., How Small Were the First Cosmological Objects?, (1997), ApJ, 474, 1.

[152] Tornatore, L., Ferrara A., & Schneider R., Population III stars: hidden or disappeared?, (2007), MNRAS, 382, 945.

[153] Trinca, A. et al., The low-end of the black hole mass function at cosmic dawn, 2021 (submitted to MNRAS).

[154] Ueda, Y. et al., Toward the standard population synthesis model of the X-ray background: evolution of X-ray luminosity and absorption functions of active galactic nuclei including Compton-thick populations, (2014), ApJ, 786, 104.

[155] Valiante, R. et al., The origin of the dust in high-redshift quasars: the case of SDSS J1148+5251, (2011), MNRAS, 416, 1916.

[156] Valiante, R. et al., High-redshift quasars host galaxies: is there a stellar mass crisis? (2014), MNRAS, 444, 2442.

[157] Valiante, R. et al., From the first stars to the first black holes, (2016b), MNRAS, 457, 3356.

[158] Valiante, R. et al., Chasing the observational signatures of seed black holes at z $>$ 7: candidate observability, (2018a), MNRAS, 474, 3825.

[159] Valiante, R. et al., Chasing the observational signatures of seed black holes at z $>$ 7: candidate statistics, (2018b), MNRAS, 476, 407.

[160] Valiante, R. et al., Unveiling early black hole growth with multi-frequency gravitational wave observations, (2020), MNRAS, 500, 4095.

[161] van den Hoek, L. B. & Groenewegen M. A. T., New theoretical yields of intermediate mass stars, (1997), A&AS, 123, 305.

[162] van de Hulst, H. C., et al., Rotation and density distribution of the Andromeda nebula derived from observations of the 21-cm line, (1957), B.A.N., 14, 1.

[163] Wang, R. et al., The black hole fundamental plane from a uniform sample of radio and X-ray emitting broad line AGNs, (2006), ApJ, 645, 890.

[164] Wild, J. P., The Radio-Frequency Line Spectrum of Atomic Hydrogen and its Applications in Astronomy, (1952), ApJ, 115, 206.

[165] Wilman, R. J. et al., A semi-empirical simulation of the extragalactic radio continuum sky for next generation radio telescopes, (2008), MNRAS, 388, 1335.

[166] Woosley, S. E., & Weaver T. A., The Evolution and Explosion of Massive Stars. II. Explosive Hydrodynamics and Nucleosynthesis, (1995), ApJS, 101, 181.

[167] Wouthuysen, S. A., On the excitation mechanism of the 21-cm (radio-frequency) interstellar hydrogen emission line, (1952), AJ, 57, 31.

[168] Wyithe, J. S. B. & Loeb, A. Undetected Sources Allow Transmission of the Lyman-alpha Line From Galaxies Prior to Reionization, (2004b), ApJ, 625, 1.

[169] Xu, H. et al., X-ray background at high redshifts from Pop III remnants: results from Pop III star formation rates in the renaissance simulations, (2016a), ApJ, 832, 140.

[170] Yajima, H. et al., Dusty Gas Accretion onto Massive Black Holes and Infrared Diagnosis of the Eddington Ratio (2017), ApJ, 846, 3.

[171] Zeldovich, Ya B., Gravitational instability: an approximate theory for large density perturbations., (1970), A&A, 5, 84.

[172] Zhukovska, S. et al., Evolution of interstellar dust and stardust in the solar neighbourhood, (2008), A&A, 479, 453.

[173] Zygelman, B., Hyperfine Level-changing Collisions of Hydrogen Atoms and Tomography of the Dark Age Universe, (2005), ApJ, 622, 1356–1362.

Acknowledgements

Alla fin fine è "solo" una laurea, ma questa laurea rappresenta comunque un primo piccolo traguardo, un traguardo per cui mi sento di dover ringraziare molte persone.
Mi sento di iniziare da tutti gli amici che mi hanno sostenuto, sopportato e accompagnato durante questi anni: siete davvero tanti e per questo mi ritengo davvero fortunato.

Grazie al CVD che, nonostante siano passati ormai molti anni e ci si veda di rado, rimanete uno dei miei più bei ricordi degli anni a cavallo tra le medie e le superiori.
Grazie ai lezzi con le nerdate a LoL e la casa di Ivano che siamo riusciti a non radere al suolo. Grazie alle finte caste e agli uomini puri per gli anni delle superiori.
Tra le varie esperienze vissute, una che non credo dimenticherò tanto facilmente è il camposcuola della mitica Piancavallo: grazie ciuccelli per esserne stati parte e per quell'alchimia unica che si è creata.
Parlando di alchimie incredibili non posso non pensare a voi staffini... Non riuscirei ad immaginare come sarebbe stato quest'ultimo anno senza le patatine, il pokerino, il mojito sulla terrazza di Anna e il sushi in Tesla.
Grazie Eminence per gli anni in Sq., grazie Gio Trev per un sacco di cose incluso il fatto che se non fosse stato per te non mi sarei giocato quest'anno come capo.
Degli ultimi 5 anni, più dei vari esami e delle lezioni mi porterò dietro i Vittone's boys. Da quella lontana prima serata al Madrid, con voi ho vissuto molte delle serate più leggendarie di sempre, senza dimenticare le uscite ad Asiago che con voi e con i bigoli della Edelweiss hanno avuto tutto un altro sapore. A proposito di serate e cibo non posso non nominare le serate di via Bottazzo che potevano essere interrotte soltanto dalle lamentele dei vicini e i pranzi del Venerdì con i Jamm Jaa. A big thank also to the international guys that joined us in Padova bringing their enthusiasm and their food (a big thank also to the international dinners and to Niko's house).
Grazie Matte e Chiara per l'ospitalità romana, grazie Marco per averti ritrovato praticamente a casissimo per riprendere quell'amicizia nata alle elementari, grazie Gio Iera perché tra Uni, pallavolo, gruppo (per un periodo) e cose varie ci sei praticamente ogni giorno, grazie Anna e cumpa' perché ormai da parecchi anni siete dei punti fermi nella mia vita.
In questa lunga fila di ringraziamenti non possono mancare coloro con cui ho condiviso praticamente di tutto. Grazie ai Paccovalli. Per tutto.

Non mi posso dimenticare della family, perché come si sa, "a famigghia è 'mportante".
In testa ovviamente devo ringraziare mamma e papà. Per avermi spronato a fare sempre di più e sempre meglio, per avermi sostenuto nelle difficoltà, per avermi fatto notare i miei errori così che potessi correggerli e quindi migliorarmi, per avermi voluto bene sempre e comunque... insomma per essere mamma e papà.
Grazie u ma' parrì, a ma' parri', u ma' figghio', zii e cugini... anche se distanti ci siete sempre stati quando era importante. Grazie nonni per la vostra dolcezza, mai come in quest'occasione sento la vostra mancanza.

Nel mio percorso scolastico ho avuto la fortuna di incontrare diversi professori che hanno saputo stimolare la mia curiosità e spronarmi a dare il meglio. Suor Marilena, prof.ssa Masutti, prof.ssa Cazzola e prof. Menniti: grazie per aver evitato che io passassi le mie giornate scolastiche interamente a giocare a Clash of Clans.
Ma soprattutto, se sono riuscito a scrivere questa tesi, lo devo in gran parte ai professori Antonino Milone, Michela Mapelli e Raffaella Schneider. Ognuno di voi è per me un punto di riferimento perché mi avete fatto conoscere ed appassionare al mondo della ricerca e per i preziosi consigli che mi avete dato.
Alla prof.ssa Schneider (e a tutto il gruppo di ricerca: Rosa, Luca, Alessandro, Federica, Claudia e Alessandra) un ringraziamento in più per avermi proposto un progetto estremamente interessante e per avermi seguito durante tutto il lavoro, non potevo sperare di capitare in un gruppo di ricerca migliore.

Infine Ilaria... non ci sono parole per esprimere il sostegno e la fiducia che mi hai trasmesso (durante questa tesi ma non solo). Grazie di aver condiviso con me tutte le sfide degli ultimi anni.